

**INSIGHTS INTO OZONE AND PM_{2.5} POLLUTION: A CASE STUDY
IN SPRING CHINA AND TREND ANALYSIS ACROSS THE
CONTINENTAL UNITED STATES**

A Dissertation
Presented to
The Academic Faculty

by

Kezhen Chong

In Partial Fulfillment
of the Requirements for the Degree
Doctor of Philosophy in the
School of Earth and Atmospheric Sciences

Georgia Institute of Technology
December 2023

COPYRIGHT © 2023 BY KEZHEN CHONG

**INSIGHTS INTO OZONE AND PM_{2.5} POLLUTION: A CASE STUDY
IN SPRING CHINA AND TREND ANALYSIS ACROSS THE
CONTINENTAL UNITED STATES**

Approved by:

Dr. Yuhang Wang, Advisor
School of Earth and Atmospheric Sciences
Georgia Institute of Technology

Dr. Nga Lee (Sally) Ng
School of Chemical and Biomolecular
Engineering
Georgia Institute of Technology

Dr. Lewis G. Huey
School of Earth and Atmospheric Sciences
Georgia Institute of Technology

Dr. Jennifer Kaiser
School of Civil and Environmental
Engineering
Georgia Institute of Technology

Dr. Rodney J. Weber
School of Earth and Atmospheric Sciences
Georgia Institute of Technology

Date Approved: December 11, 2023

ACKNOWLEDGEMENTS

I would like to express my sincere gratitude to my advisor, Dr. Yuhang Wang, without whose support and patient guidance I would not have been able to complete my research. I have always been inspired by his professional knowledge and insights throughout my Ph.D. I would also like to thank my Ph.D. thesis committee members, Dr. Lewis G. Huey, Dr. Jennifer Kaiser, Dr. Nga Lee (Sally) Ng, and Dr. Rodney J. Weber for reviewing this thesis and their comments.

I would like to thank the group members. I have had a great time working with Dr. Hang Qu, Dr. Jianfeng Li, Dr. Aoxing Zhang, Dr. Qiyang Yan, Fanghe Zhao, and Shengjun Xi. Special appreciation goes to my steadfast friend, Yuhan Yang, who has always been by my side throughout this endeavor. Furthermore, I express sincere thanks to Ke Xu for his enduring patience and support over the years.

Lastly, I want to express my deepest and most sincere thanks to my parents for their unwavering encouragement and support, particularly during the most demanding stages of my research. Their unwavering belief in me has served as the guiding force propelling me forward.

TABLE OF CONTENTS

ACKNOWLEDGEMENTS	iii
LIST OF TABLES	vi
LIST OF FIGURES	vii
LIST OF SYMBOLS AND ABBREVIATIONS	xii
SUMMARY	xv
CHAPTER 1. Introduction	1
1.1 Introduction and Background	1
1.2 Thesis Outline	4
CHAPTER 2. Observation-based Diagnostic of Photoactive Heterogeneous HONO Sources and their Divergent Implications for Ozone Production	6
2.1 Introduction	6
2.2 Methods and Materials	9
2.2.1 Observations	9
2.2.2 Data Preparation	10
2.2.3 Photochemical Models, Source Parameterizations, and Simulated cases.	12
2.3 Results and Discussions	15
2.3.1 Observation Overview and Effects of Biomass Burning and Aerosol Acidity	16
2.3.2 Validities of Different Photoactive Heterogeneous HONO Sources	21
2.3.3 Sensitivity of O ₃ Production to Heterogeneous HONO Sources	26
2.4 Conclusion	31
CHAPTER 3. Remote Sensing Measurements at a Rural Site in China: Implications for Satellite NO₂ and HCHO Measurement Uncertainty and Emissions from Fires	35
3.1 Introduction	35
3.2 Method	38
3.2.1 Ground-based MAX-DOAS Measurement	38
3.2.2 Satellite Products and AMF Calculations	40
3.3 Results and Discussions	46
3.3.1 Overview of the Observations and Intercomparisons	46
3.3.2 Resolving the Difference Between NASA and KNMI NO ₂ TVCDs	55
3.3.3 Biomass Burning Impacts on HONO, NO ₂ , and HCHO	60
3.4 Conclusions	70
CHAPTER 4. Seasonal and Historical Trends of Secondary Organic Carbon across the Continental United States	73
4.1 Introduction	73

4.2	Material and Methods	76
4.2.1	Observational Dataset	76
4.2.2	ACCA Clustering Method	77
4.2.3	EMSOC	78
4.2.4	SMLR Method for Factor Analysis	80
4.3	Results and Discussions	82
4.3.1	Regional Clustering and Validation	82
4.3.2	Factor Analysis of Summertime SOC	85
4.3.3	Increasing SOC Despite Decreasing Anthropogenic Emissions	89
4.4	Conclusions	93
CHAPTER 5.	Conclusions and future work	96
5.1	Observation-based Diagnostic of Photoactive Heterogeneous HONO Sources and their Divergent Implications for Ozone Production	96
5.2	Remote Sensing Measurements at a Rural Site in China: Implications for Satellite NO₂ and HCHO Measurement Uncertainty and Emissions from Fires	97
5.3	Seasonal and Historical Trends of Secondary Organic Carbon across the Continental United States	99
REFERENCES		102

LIST OF TABLES

Table 1	Instruments used during the OPECE campaign.	10
Table 2	Simulation cases.	15
Table 3	Comparisons of HONO source parameterizations to previous studies.	25
Table 4	Comparisons of HONO/NO ₂ and HONO/pNO ₃ of different studies.	29
Table 5	Satellite products and their abbreviations used in this work.	40
Table 6	Quality filters applied to satellite products.	42
Table 7	Intercomparison results for NO ₂ TVCDs: correlation coefficient (r), p-value, slope for the through-the-origin least squares regression, root mean square error (RMSE), mean bias error (MBE), and number of data pairs (N) in each set of comparison between satellite and MAX-DOAS data.	48
Table 8	Same as Table 7 but for HCHO TVCDs.	48
Table 9	Stepwise regression results for MLR of SOC on log-transformed sulfate (log.SO ₄) and nitrate(log.NO ₃), HCHO TVCD (TVCD_HCHO), Fire (Emissions_C) and Radiation (ssrd). Columns from left to right are region names, index for the selected model, number of predictors selected, selected predictors, correlation coefficient, adjusted correlation coefficient, and Mallow's Cp.	81

LIST OF FIGURES

Figure 1	Radius ratio of ambient to dry aerosols as a function of RH.	11
Figure 2	Comparisons of daily AMS and PM _{2.5} filter measurements of aerosol inorganic ions: (a) pNO ₃ , (b) SO ₄ ²⁻ , (c) NH ₄ ⁺ , and (d) Cl ⁻ . Red solid lines denote through-the-origin least-squares regressions and red dashed lines are 1:1 lines.	12
Figure 3	Time series for O ₃ , NO _x , HONO, pNO ₃ , and S _A from 23 March to 22 April 2018.	17
Figure 4	Mean diurnal profiles for observed O ₃ , NO ₂ , HONO, pNO ₃ , S _A , and NO.	18
Figure 5	Correlations of CH ₃ CN with NO ₂ , pNO ₃ , S _A and organic matters in aerosol.	18
Figure 6	(a) Scatter plot of HONO (blue), HONO/NO ₂ (red), and HONO/pNO ₃ (yellow) as a function of CH ₃ CN. (b) Same as (a) but as a function of aerosol pH. (c) Box plots of HONO concentrations for clean and BB airmasses where the mean value is denoted by the red dot. And the median is denoted by black line. (d) and (e) are like (c) but for HONO/NO ₂ and HONO/pNO ₃ , respectively.	21
Figure 7	Frequency histogram for observation data points of different levels of CH ₃ CN.	22
Figure 8	(a) Scatter plot of pHONO as functions of pNO ₃ (blue), pNO ₃ ×jHNO ₃ (red), and P(HNO ₃) (green). (b) Same as (a) but as functions of NO ₂ (blue) and NO ₂ ×S _A ×SWR (red). The corresponding correlation coefficients are shown at the bottom right corner of the plots. (c) Observed diurnal HONO (black dots) with standard deviation (black vertical lines) and simulated HONO under the six cases (B, S0-S3) as described in Table 2. Simulation cases. (d) Mean diurnal profiles of pNO ₃ (orange) and NO ₂ (blue) during the measurement period. All panels show the non-BB data.	23
Figure 9	Simulated evolutions of O ₃ , NO _x , HONO, pNO ₃ , OH, and PO ₃ in a Lagrangian box model for seven days under cases F0 – F3. (b) O ₃ enhancement ratios, defined as the relative O ₃ increase from the initial O ₃ concentration for cases F0 – F3. (c), (d), and (e) are simulated evolutions of HONO/NO ₂ , HONO/pNO ₃ and NO _x /pNO ₃	28

ratios. The dashed lines denote measured HONO/NO₂, HONO/pNO₃ and NO_x/pNO₃ values from Ye et al.¹¹⁷.

- Figure 10 (a) Cumulative PO₃ as a function of initial NO_x for cases F0 - F3. The dashed lines denote NO_x levels at which cumulative PO₃ reaches its peak values. (b) Loss of NO_x (Δ NO_x) as a function of initial NO_x. 31
- Figure 11 Ozone production efficiency (OPE) as a function of initial NO_x concentrations for cases F0 - F3. 31
- Figure 12 Annual mean maximum daily average 8-hr (MDA8) O₃ concentrations (left) and annual mean noontime NO₂ concentrations (right) for eastern China from 2014 to 2022. 34
- Figure 13 The observation site (yellow marker) and large cities (blue markers) (from Google Earth). The upper right panel shows the site location and satellite observation pixel grids for OMI L2, TROPOMI L2, and TROPOMI L3 products. 39
- Figure 14 Box plots of OMI-NASA, OMI-KNMI, and TROPOMI v1.0.1 cloud pressures on cloudy days identified by TROPOMI. 45
- Figure 15 Standard satellite products compared with AMF_{REAM} retrieved TVCDs (molecules/cm³), the orange and green dots denote cloud corrected TROPOMI using OMI-NASA (TROPOMI_REAM_CC_N) and OMI-KNMI (TROPOMI_REAM_CC_K) cloud pressures accordingly. The red lines represent a 1:1 reference. The dashed lines denote the fitted lines on the corresponding scattered data. The root mean square error (RMSE) between TROPOMI_REAM_noCC and TROPOMI_REAM_CC_K is 1.8×10^{15} molecules/cm³, (relative change 29.7%) while that between TROPOMI_REAM_CC_K and TROPOMI_REAM_CC_N is 1.7×10^{14} molecules/cm³ (relative change 2.5%). The fitted slopes for TROPOMI_REAM_noCC, TROPOMI_REAM_CC_N, and TROPOMI_REAM_CC_K, against original TROPOMI products are 1.11, 1.28, and 1.29, respectively. 45
- Figure 16 The daily evolution of FIRMS fire counts within 5 km from the observation site. 46
- Figure 17 Daily variations and uncertainties (vertical error bars) of TVCDs from Mar 08, 2018, to Apr 26, 2018. (a) Time series of daily NO₂ TVCD data from MAX-DOAS (black), OMI-NASA (orange), OMI-KNMI (blue), and TROPOMI (green). (b) Time series of daily HCHO TVCD data from MAX-DOAS (black), OMI-NASA 47

(orange), OMI-BIRA (blue), and TROPOMI (green). The red shadings indicate days affected by nearby burning activities.

- Figure 18 Intercomparison between NO₂ TVCDs from MAX-DOAS and those from satellites. (a) Before AMF adjustments, i.e., OMI-NASA (orange), OMI-KNMI (blue), and TROPOMI (green). (b) After AMF corrections using AMF_{REAM}, i.e., NASA_REAM (orange), KNMI_REAM (blue), and TROPOMI data with/without cloud correction (TROPOMI_REAM_CC/TROPOMI_REAM_noCC, olive/green). The dashed lines are least-squares regressions through the origin between satellite and MAX-DOAS data. A solid red line represents the 1:1 reference. 50
- Figure 19 Slopes with error bars (top panel) and correlation coefficients (R, bottom panel) for NO₂ TVCDs observed between satellites and MAX-DOAS, from left to right, are TROPOMI, TROPOMI_REAM without cloud correction, TROPOMI_REAM with cloud correction, KNMI, KNMI_REAM, NASA, NASA_REAM. The boxes with slash lines denote AMF_{REAM} corrected satellite data. The boxes with red borders represent data with a p-value < 0.05, indicating statistical significance. 52
- Figure 20 Slopes with error bars (top panel) and correlation coefficients (R, bottom panel) for HCHO TVCDs observed between satellites and MAX-DOAS, from left to right, are TROPOMI, OMI-BIRA, BIRA_REAM, NASA, and NASA_REAM. The boxes with slash lines denote AMF_{REAM} corrected satellite data. The boxes with red borders represent data with a p-value < 0.05, indicating statistical significance. 53
- Figure 21 Original AMFs vs REAM-scaled AMFs for two OMI HCHO products. The red dashed line represents a 1:1 reference. 53
- Figure 22 Intercomparison of HCHO TVCDs from MAX-DOAS with those from satellites. (a) OMI-NASA, OMI-BIRA, and TROPOMI data before AMF adjustment. (b) OMI-NASA and OMI-BIRA data after AMF adjustment. The boxes with error bars show the average and standard deviations for the corresponding variables in each bin of MAX-DOAS data. The vertical bars with standard deviations show the Sd ratio, the standard deviation ratios of satellite to MAX-DOAS data in each bin, in which more than 2 data points are available. The dashed lines are fitted on the corresponding scatter plots (in (a)) through the origin, with a solid red line representing the 1:1 reference. 54
- Figure 23 Scatter plots of original AMF (blue) and REAM profile scaled AMF_{REAM} (orange) from OMI-NASA versus OMI-KNMI. The 56

dashed lines are least-squares regressions through the origin, and a solid red line represents the 1:1 reference.

Figure 24	The median vertical profiles with standard deviations (horizontal error bars) of scattering weights (w) of OMI-NASA (orange) and OMI-KNMI (blue) products from Mar 08 to Apr 26, 2018.	57
Figure 25	The box plots for cloud pressure (hPa, upper row) and cloud radiance fraction (unitless, lower row) of OMI-KNMI and OMI-NASA.	59
Figure 26	Mean cloud pressure (upper row) and mean cloud radiance fraction (lower row) from OMI-KNMI (left column) and OMI-NASA (right column) NO ₂ products. The purple box denotes the grid that contains the observation site (denoted by the purple triangle in the upper right panel).	60
Figure 27	MAX-DOAS observations for SO ₂ , HONO, HCHO, NO ₂ , and AEC during the 7 BB days identified by FIRMS fire data.	62
Figure 28	FIRMS observed fire hotspots (red squares) around the observation site (denoted as a yellow marker on the map) on Mar 25 th (top panel) and Apr 11 th (bottom panel).	64
Figure 29	MAX-DOAS observed daytime evolutions of SO ₂ , HONO, HCHO, NO ₂ , and AEC mixing ratios for (a) non-burning days under clean conditions, (b) on Apr 11, 2018, during the burning events under clean conditions, (c) non-burning days under polluted conditions, and (d) on Mar 25, 2018, during the burning events under polluted conditions.	66
Figure 30	Surface mixed layer height (solid red lines) calculated by MAX-DOAS vertical profiles of SO ₂ from Mar 8 th to Apr 26 th , 2018.	68
Figure 31	(a) Enhancement ratios of BB to non-BB days of NO ₂ , HONO, HCHO, AEC, and SO ₂ in the upper and lower columns for Apr 11. (b) Same as (a) but for Mar 25. (c) BB enhancement ratios relative to SO ₂ enhancement in the upper and lower columns for NO ₂ , HONO, HCHO, and AEC for Apr 11. (d) Same as (c) but for Mar 25. See text for details.	70
Figure 32	ACCA grouped clusters.	78
Figure 33	Normal quantile-quantile (Normal QQ) plots before and after log-transformation for sulfate (SO_4^{2-}) and nitrate (NO_3^-).	81

Figure 34	Overview of EMSOC derived secondary ratios (SOC/OC). (a) Validation against other methods; (b) Annual mean EMSOC-derived SOC/OC for each cluster.	85
Figure 35	One on one comparison of SOC/OC derived from our study versus previous values.	85
Figure 36	(a) Seasonal variations of SOC for each of the six regions; (b) is similar to (a) but for POC. (c) Normalized seasonal mean and standard deviations of SOC, POC, and OC for all CONUS sites; (d) inter-regional deviations for SOC and POC in each season.	86
Figure 37	(a) Resulted p-values from MLR built on significant factors, where shaded cells means that the corresponding factor is insignificant. (b) Normalized regional mean concentrations of all factors.	87
Figure 38	Trend of SOC and POC [percent/decade]. Solid filled cells indicate that the trend is significant, while transparent cells indicate that no significant trend is detected.	89
Figure 39	Trends of all species. Solid filled cells indicate that the trend is significant, while transparent cells indicate that no significant trend is detected.	90
Figure 40	Historical trends for HCHO TVCDs (left) and Surface Solar Radiation Downwards (SSRD) (right).	91
Figure 41	Historical trends for and fire carbon emissions from GFED.	92
Figure 42	Historical trends for Canadian fire emissions.	92
Figure 43	Relative trend of annual SOC/OC. Solid cells indicate that the trend is significant, while transparent cells indicate that the trend is insignificant.	93
Figure 44	Illustration of the accounted SOC in two methods	101

LIST OF SYMBOLS AND ABBREVIATIONS

ACCA	Average Correlation Clustering Algorithm
AMF	Tropospheric Air Mass Factor
AMF _{REAM}	REAM Scaled AMF
AMS	Aerosol Mass Spectrometer
AOD	Aerosol Optical Depth
AVKs	Averaging Kernels
BB	Biomass Burnings
BIRA	Royal Belgian Institute for Space Aeronomy
CH ₃ CN	Acetonitrile
CMB	Chemical Mass Balance
CONUS	Continental United States
DOAS	Differential Optical Absorption Spectroscopy
EC	Elemental Carbon
EF	Enhancement Factor for Calculating $jpNO_3$
EMSOC	Empirical SOC
FIRMS	Fire Information for Resource Management System
GEOS	Goddard Earth Observing System
GFED	Global Fire Emissions Database
GLER	Geometry-dependent surface Lambertian Equivalent Reflectivity
HCHO	Formaldehyde
HNO ₃	Nitric Acid
HONO	Nitrous Acid

HR-ToF-AMS	High-Resolution Time-of-Flight Aerosol Mass Spectrometry
IMPROVE	Interagency Monitoring of Protected Visual Environments
ISOP	Isoprene
IUP	Institute Of Environmental Physics, University of Bremen
jHNO ₃	Photolysis Rate of HNO ₃
jNO ₂	Photolysis Rate of NO ₂
jpNO ₃	Photolysis Rate of pNO ₃
KNMI	Royal Netherlands Meteorological Institute
LOPAP	Long Path Absorption Photometer
LT	Local Time
MAX-DOAS	Multi-Axis Differential Optical Absorption Spectroscopy
MBE	Mean Bias Error
MLR	Multiple Linear Regression
MODIS	Moderate Resolution Imaging Spectroradiometer
MPIC	Max Planck Institute for Chemistry
NCP	North China Plain
NO	Nitric Oxide
NO ₂	Nitrogen Dioxide
NO _x	Nitrogen Oxides (NO+NO ₂)
O ₃	Ozone
OC	Organic Carbon
OH	Hydroxyl Radical
OMI	Ozone Monitoring Instrument
OPECE	Ozone Photochemistry and Export from China Experiment
pHONO	Missing HONO Source Strength

PM _{2.5}	Particulate Matter Finer than 2.5 μm Aerodynamic Diameter
PMF	Positive Matrix Factorization
pNO ₃	Particulate Nitrate
PTR-ToF-MS	Proton Transfer Reaction Time-of-Flight Mass Spectrometry
REAM	Regional chEmical trAnsport Model
RMSE	Root Mean Square Error
SCDs	Slant Column Densities
SOC	Secondary OC
SWR	Short Wave Radiation
TROPOMI	Tropospheric Monitoring Instrument
TVCDs	Tropospheric Vertical Column Densities
UV	Ultraviolet
VOCs	Volatile Organic Compounds
W	Scattering Weight Vector
WRF	Weather Research and Forecasting model

SUMMARY

In the troposphere, ozone (O_3) and fine particulate matter ($PM_{2.5}$) stand out as two major pollutants, with their production intricately tied to various photochemical processes involving nitrogen oxides ($NO_x = NO + NO_2$) and volatile organic compounds (VOCs). A better understanding of these chemical processes, along with precise quantifications of the relative abundance of the precursors and their regional characteristics, plays a crucial role in addressing O_3 and $PM_{2.5}$ pollution. This dissertation utilizes ground- and satellite-based observations and model simulations to provide comprehensive insights into the complex photochemistry underlying O_3 and $PM_{2.5}$ formation.

Extensive ground-based observations of trace gases and particles were obtained at a rural coastal site in eastern China during the Ozone Photochemistry and Export from China Experiment (OPECE) campaign in spring 2018. We first utilized this dataset to validate three photoactive heterogeneous HONO sources: photoactive conversion of NO_2 on aerosols, photolysis of particulate nitrate (pNO_3), and the photolysis of adsorbed nitric acid (HNO_3). Subsequently, we diagnosed their implications for O_3 production with model simulations. We utilized this extensive dataset to investigate the recycling of reactive nitrogen through daytime heterogeneous HONO productions. The comparable agreement between observed and simulated HONO concentrations with any one of the three heterogeneous HONO production mechanisms involving reactive nitrogen suggests the intrinsic relationships between NO_2 , pNO_3 , and HNO_3 . However, the implications for reactive nitrogen recycling, O_3 production, and O_3 control strategy vary greatly. The conversion of HONO from pNO_3 can drastically enhance O_3 production on a regional basis,

while the conversion of HONO from NO₂ can reduce O₃ sensitivity to NO_x changes in polluted eastern China. Furthermore, our results showed that increased HONO levels in BB is likely due to increased precursor levels, rather than direct emissions.

Furthermore, satellite observations of NO₂ and HCHO, which are often used in the investigation of regional photochemistry patterns, are validated by the ground-based multi-axis differential optical absorption spectroscopy (MAX-DOAS) measurements at this coastal rural site in China. A total of six satellite products from the Ozone Monitoring Instrument (OMI) and the TROPOspheric Monitoring Instrument (TROPOMI) were analyzed. We found generally better agreement between MAX-DOAS and satellite product for NO₂ data than for HCHO data. Nonetheless, TROPOMI HCHO products showed significantly better agreement with MAX-DOAS measurements compared to OMI data. After unifying the a priori profiles used in the air mass factor (AMF) calculation, the most significant factor contributing to the discrepancies between the two OMI NO₂ products is found to be the scattering weight, which is affected largely by the different choices of ancillary parameters, such as cloud. In addition, an investigation on the BB days highlighted the variability of BB impact on HONO.

Lastly, we divided the continental US (CONUS) into six regions according to the correlations of organic carbon (OC) concentrations among different sites and investigated the seasonal and historical trends of secondary organic carbon (SOC) using OC and elemental carbon (EC) data by the Interagency Monitoring of PROtected Visual Environments (IMPROVE) network across CONUS from 2005 to 2020. The regional mean secondary fractions vary from 22% to 40% and are consistent with co-located values reported by previous studies. Unlike primary OC (POC), SOC exhibits a consistent

seasonal variation with a peak in summer across all regions. For summertime SOC, HCHO is found to be a significant contributor to all regions except for CA, where fire plays a significant role. Furthermore, we found a more significant correlation of SOC with sulfate than nitrate, particularly in regions where sulfate concentrations are low. In addition, despite decreasing trends of anthropogenic precursors of SOC and POC concentrations in the past two decades, significant decreasing SOC trends are found only in the eastern US in winter, as well as Southeast (SE) in summer. Accordingly, SOC fraction trends are found to be significantly increasing except for SE. As anthropogenic emissions decrease, SOC will most likely account for increasingly larger fractions of OC and PM_{2.5}.

CHAPTER 1. INTRODUCTION

1.1 Introduction and Background

Tropospheric ozone (O_3) and fine particulate matter ($PM_{2.5}$) are two of the most important pollutants in the troposphere. Not only do they have detrimental effects on human and vegetation health, but they also pose threats to ecosystem productivity¹. In fact, $PM_{2.5}$ was listed the fifth mortality risk factor in 2015², underscoring the urgency of addressing air pollution problems³. Despite notable improvements in air quality initiatives, the persistence of O_3 and $PM_{2.5}$ pollution remains a global concern, especially in developing regions⁴. Notably, China has experienced severe O_3 and $PM_{2.5}$ pollution over the past decade^{5, 6}, while in the United States, although strict mitigation steps have been taken to decrease anthropogenic emissions, the exceedance of the standard still happens, necessitating continued efforts in air quality control^{7, 8}.

O_3 formation includes two main precursors: volatile organic compounds (VOCs) and nitrogen oxides ($NO_x = NO_2 + NO$). Specifically, the reaction of VOCs with hydroxyl radicals (OH) generates peroxy radicals (HO_2 and RO_2). The produced HO_2 and RO_2 can further convert nitric oxide (NO) to nitrogen dioxide (NO_2), contributing to the net production of O_3 ⁹. In addition, the formation of secondary organic carbon (SOC), which constitutes a significant yet highly uncertain portion of $PM_{2.5}$ ¹⁰, also includes the oxidations of VOCs. Specifically, the oxidation process yields products with reduced volatility and increased solubility, enabling them to either partition to preexisting particles or nucleate to form new particles. Moreover, though this process is usually biogenic driven due to their

large emissions globally, studies have indicated that NO_x can modulate this process by affecting the reactions in many ways^{11, 12}.

Various production pathways of SOC remains unclear¹³, moreover, due to the nature of its definition, it is difficult to directly measure SOC, contributing to the difficulties of controlling PM_{2.5} pollution. Tackling the issue of PM_{2.5} pollution requires a better quantification of SOC over large temporal and spatial coverages.

While there is a good understanding of the overall formation mechanism of O₃ compared to SOC, the additional radical sources, which can significantly influence the relative abundance of NO_x and VOCs, thereby affecting the relationship between O₃ and its precursors, remain not entirely clear. For example, previous studies have reported a large missing source of nitrous acid (HONO), which serves as an important OH source via fast photolysis, posing obstacles in accurate prediction of O₃ in the models. Therefore, tackling the detrimental effects of poor air quality requires a better understanding of the processes involved in O₃ and SOC formation¹⁴⁻¹⁶.

In the pursuit of comprehending this intricate system, substantial effort has been devoted over the past several decades through both observational and modeling techniques. In situ observation data is particularly useful by providing high-resolution data associated with real atmospheric conditions¹⁷. Correspondingly, long-term measurement networks, such as the Interagency Monitoring of PROtected (IMPROVE) network, have provided crucial observational insights in tracking the regional patterns and historical trends of key air pollutants^{18, 19}. Furthermore, satellite observations, focusing on tropospheric vertical column densities (TVCDs) of key trace gases, such as formaldehyde (HCHO) and NO₂,

have facilitated the investigation of regional air pollution conditions by providing quantifications of their precursors²⁰. Complementing these efforts, model simulations have also proven to be invaluable tools in simulating key photochemical processes involved in O₃ and SOC formations^{21, 22}.

Building upon the foundations laid by prior research, this thesis employs modeling analysis, along with ground- and satellite- based measurements to comprehensively understand the processes involved in O₃ and PM_{2.5} pollution. Firstly, this work provides a comprehensive examination of three most common photoactive heterogeneous production mechanisms of HONO, including photoenhanced NO₂ conversion on aerosol surfaces, photolysis of particulate nitrate (pNO₃) and adsorbed nitric acid (HNO₃). By dissecting the sources of HONO, this research gains their implications for O₃ production, contributing to the understanding of the intricate processes involved in O₃ production. Secondly, this work validates satellite measurements of HCHO and NO₂, which provides insights on discrepancies associated with assessing pollutants using satellite data. This validation offers insights into the complexities of satellite-based pollution assessment, essential for refining future remote sensing techniques. Lastly, this thesis analyzes historical and seasonal trends of SOC along with ancillary datasets. By characterizing the regional trends of SOC, this work aims to provide essential inputs for the development of targeted regional mitigation strategies.

By delving into these three critical aspects, this thesis aims to contribute to our understanding of the intricate dynamics of O₃ and PM_{2.5} pollution, fostering the development of more effective and targeted mitigation strategies.

1.2 Thesis Outline

Chapter 1 introduces the O₃ and PM_{2.5} pollution issues and the related photochemical processes in the troposphere.

Chapter 2 investigates the photoactive heterogeneous HONO sources and their divergent implications for O₃ production. Eastern China is characterized by severe O₃ pollution with high aerosol loadings, providing an optimal setting to understand the heterogeneous HONO production pathways and their implications for O₃ production. This chapter utilizes a suite of surface measurement data at a rural coastal site in eastern China during spring 2018. With more and more observational studies highlighting the existence of either of the three sources, this work first validates all three sources and testifies the ability of in situ observations to distinguish among the three heterogeneous pathways. Furthermore, to better understand how these HONO sources will contribute to O₃ pollution, implications for O₃ production are assessed through diagnostics of the recycling of reactive nitrogen via different HONO heterogeneous production mechanisms. Through the investigation of these HONO production pathways, this chapter gives a better understanding of the photochemical processes involved in O₃ and PM_{2.5} pollution.

Chapter 3 validates satellite measurements of two main precursors associated with O₃ and PM_{2.5} formations, NO_x and VOCs. This chapter intercompares six different satellite products of NO₂ and HCHO, indicators for NO_x and VOCs, and validates them with ground-based remote sensing measurement from the Multi-Axis Differential Optical Absorption Spectroscopy (MAX-DOAS) data to understand the discrepancies and their causes among different satellite products on non-biomass burning (BB) days. Utilizing

measurements on BB-affected days, this chapter further investigates BB effects on trace gases, such as HCHO, NO₂ and HONO. Through the investigation into the discrepancies associated with different satellite products, this chapter provides insights into factors that needed to be considered while utilizing satellite measurement in assessing pollution precursors.

Chapter 4 investigates historical and seasonal trends of SOC across the continental US (CONUS) from 2005 to 2020. Current studies on SOC are usually limited in both temporal and spatial coverages, preventing trend and regional studies of SOC. In this chapter we utilize an empirical methodology that can be applied efficiently in a consistent manner to estimate SOC using the historical OC and EC data from the IMPROVE network for six regions in CONUS. Seasonal variations, significant factors for summertime SOC in each region, as well as historical trends from 2005 to 2020, are investigated through stepwise multi-linear regression and other statistical tests. This study provides a comprehensive examination of SOC that covers, to the best of our knowledge, the largest spatial (CONUS) and longest temporal (15 years) coverages in SOC studies. The results provide insights into the historical trends and regional effects for SOC across the United States.

Chapter 5 concludes the thesis and summarizes the findings and future works.

CHAPTER 2. OBSERVATION-BASED DIAGNOSTIC OF PHOTOACTIVE HETEROGENEOUS HONO SOURCES AND THEIR DIVERGENT IMPLICATIONS FOR OZONE PRODUCTION

2.1 Introduction

Nitrous acid (HONO) plays a significant role in the production of the hydroxyl radical (OH) via fast photolysis²³⁻²⁶. Understanding HONO formation mechanisms advances our knowledge of photochemical processes to better predict and regulate regional air pollution, such as the formation of O₃ and secondary organic aerosols²⁷⁻³⁰.

HONO is produced through the gas-phase reaction of nitric oxide (NO) and OH (R1)³¹. Direct emissions from combustion activities, such as vehicle exhaust and biomass burning (BB) can also contribute to HONO levels³²⁻³⁷. In recent years, observations in a variety of locations have found other daytime HONO sources to be important^{38, 39}.



Various HONO production pathways have been proposed based on field measurements and laboratory experiments, with heterogeneous reactions highlighted as crucial contributors⁴⁰⁻⁴³. For example, studies have demonstrated the importance of heterogeneous nitrogen dioxide (NO₂) conversion on ground surfaces as an important nocturnal HONO source⁴⁴, where production of HONO (prod(HONO)) is parameterized as in Eq. (1):

$$\text{prod(HONO)} = f \times [\text{NO}_2] \times V_d/H \quad (1)$$

where f is the yield of HONO from deposited NO_2 reaching the surface; H is the height of the first model layer, and V_d is the dry deposition velocity of NO_2 . However, this source and gas-phase production still cannot explain observed daytime HONO losses^{21, 45-47}. Aerosol reactions were recognized as a contributor to HONO productions as early as the 1990s⁴⁸. Research by Ammann et al. detected HONO production from NO_2 on suspended soot particles, though not sufficient to explain the observed daytime HONO levels, this study highlighted the important role of aerosols in HONO production⁴⁹. Since then, numerous observations have reported HONO heterogeneous production pathways, including photosensitized conversion of NO_2 ⁵⁰⁻⁵⁸, where the reactive uptake coefficient (γ) can be enhanced by short wave radiation (SWR) as parameterized in Eq. (2), and photolysis of particulate nitrate (pNO_3) (Eq. (3))⁵⁹⁻⁶², or adsorbed nitric acid (HNO_3)⁶³⁻⁶⁵ (Eq. (4)). In Eq. (3) and Eq. (4), Y_{HONO} is the yield coefficient of HONO from HNO_3 , while EF is the enhancement factor to calculate the photolysis rate of pNO_3 ($j\text{pNO}_3$) from HNO_3 photolysis rate ($j\text{HNO}_3$). More details regarding these HONO sources will be discussed later.

$$\text{prod}(\text{HONO}) = k_a[\text{NO}_2], k_a = S_A \left[\frac{R_p}{D_g} + \frac{4}{\gamma\omega} \right]^{-1}, \gamma = \text{SWR} \times \gamma' \quad (2)$$

$$\text{prod}(\text{HONO}) = EF \times j\text{HNO}_3 \times [\text{pNO}_3] \quad (3)$$

$$\text{prod}(\text{HONO}) = Y_{\text{HONO}} \times P(\text{HNO}_3 \text{ from } \text{NO}_2 + \text{OH}) \quad (4)$$

Although the precise mechanism of aerosol-induced HONO production is still a subject of debate⁶⁶⁻⁶⁸, heterogeneous mechanisms have been included into atmospheric chemistry simulations and have shown promising agreement with observed levels of

HONO. Various HONO budget analyses have been conducted, yet the prevailing mechanism responsible for daytime HONO production beyond R1 remains uncertain⁶⁹⁻⁷². This is due in part to large uncertainties in key reaction parameters of heterogeneous daytime HONO production, such as the reactive uptake coefficient of NO₂ (γ), the enhancement factor of jpNO₃ (EF), and HONO yield coefficient (Y_{HONO}) from photolysis of adsorbed HNO₃, as well as variations in precursor concentrations observed in different campaigns.

Furthermore, environmental factors, such as BB⁷³⁻⁷⁵ and aerosol acidity^{76, 77}, can impact HONO production. This provides additional challenges to characterize HONO sources. For example, Nie et al.⁷³ found that the conversion rate of NO₂ to HONO in BB plumes is twice that in non-BB plumes, suggesting that BB aerosol composition can enhance NO₂ conversion efficiencies of BB aerosols. Aerosol acidity can also affect the volatility of aerosol components and gas-particle partitioning and HONO heterogeneous production tends to increase with decreasing pH⁷⁸⁻⁸⁰.

In this chapter, we test these proposed HONO heterogeneous mechanisms, including photosensitized NO₂ conversion on aerosols, photolysis of pNO₃, and photolysis of surface adsorbed HNO₃ on aerosols, using a comprehensive dataset of gaseous and particulate compositions measured at a rural coastal site during the 2018 spring Ozone Photochemistry and Export from China Experiment (OPECE)¹⁴. Observations at a remote location are ideal for diagnosing photochemical processes due in part to generally less-complex emission characteristics compared to urban regions. In this work we investigate the impact of BB and aerosol acidity on observed HONO concentrations. Focusing on the observations not affected by BB, we also analyze the intrinsic photochemical relationships

between NO_2 , pNO_3 , and HNO_3 in the remote boundary layer and how the relationships can obscure the diagnostics of HONO heterogeneous production mechanisms. Lagrangian box model simulations are used to demonstrate the utility of diagnosing O_3 enhancements by the recycling of reactive nitrogen species through HONO production on aerosols. We also investigate the implications of the different HONO heterogeneous production mechanisms for O_3 control strategy.

2.2 Methods and Materials

2.2.1 Observations

The OPECE campaign was carried out at the Yellow River Delta Ecology Research Station of the Coastal Wetland in Dongying, Shandong, China. The rural coastal site (37.76°N , 118.98°E) is located in the Yellow River Delta region near the Shandong Yellow River Delta National Nature Reserve¹⁴. The closest urban area, Dongying, is located approximately 50 km southwest of the site. From 23 March to 22 April of 2018, surface concentrations of HONO were measured by a Long Path Absorption Photometer (LOPAP)⁸¹⁻⁸⁵. Additionally, measurements of other species, including NO_x ($\text{NO}+\text{NO}_2$), O_3 , acetonitrile (CH_3CN), carbon monoxide (CO), volatile organic compounds (VOCs), aerosol size distribution, NO_2 photolysis rate ($j\text{NO}_2$), as well as meteorological parameters, including pressure, temperature, and relative humidity (RH) during this period were obtained. Detailed information regarding the chemical instruments used is provided in Table 1 and previous studies¹⁴.

Table 1. Instruments used during the OPECE campaign.

Parameters	Instruments	Temporal resolution
HONO	LOPAP	1 min
NO, NO ₂	Thermo 42i	1 min
O ₃	Thermo 49i	1 min
CO	Thermo 48i	1 min
VOCs	GCFID or PTR-ToF-MS	60min or 1min
Aerosol number size distribution	Scanning Mobility Particle Sizer (SMPS)	5 min
CH ₃ CN	PTR-ToF-MS	1 min
jNO ₂	Actinic flux	1 min
Aerosol chemical composition	Sample filter analysis	24 hour
	Aerosol Mass Spectrometer (AMS)	1 min

2.2.2 Data Preparation

Ambient aerosol surface area (S_A) was calculated from the observed dry surface areas S_A^{dry} while accounting for the hygroscopic effect through Eq. (5) as described in Lewis et al.⁸⁶, where $a = 0.78$ and $b=1.90$ are two empirical parameters chosen accordingly with the assumption of aerosol composition to be ammonium sulfate. Figure 1 illustrates the relationship between the radius ratio of ambient (r) to dry (r_{dry}) aerosols and relative humidity (RH). The calculated S_A at the surface is scaled by the vertical profile of aerosol extinction coefficient (AEC) measured by Multi-Axis Differential Optical Absorption Spectroscopy (MAX-DOAS) to get S_A for layers above the surface. The aerosol size measurement range from SMPS covers the submicron range (10 nm to 700 nm), therefore the S_A in our study here represents a lower limit.

$$\frac{r}{r_{\text{dry}}} = a \left(b + \frac{1}{1 - \text{RH}} \right)^{\frac{1}{3}}, S_A = S_A^{\text{dry}} \times \left(\frac{r}{r_{\text{dry}}} \right)^2 \quad (5)$$

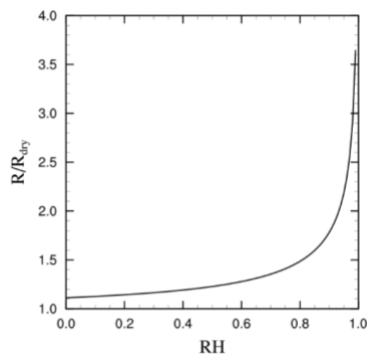


Figure 1. Radius ratio of ambient to dry aerosols as a function of RH.

Aerosol chemical composition was measured by both AMS and PM_{2.5} filter samples (Table 1). Comparisons of daily inorganic ion concentrations reported by the two instruments demonstrate reasonable agreement with p-values <0.05 and measurement ratios ranging from 0.83 to 1.1 (Figure 2). The AMS instrument sample particles size < 1 μm. Therefore, AMS data are generally lower than the filter measurements. In our study, we combined the two datasets to obtain pNO₃ and other inorganic aerosol concentrations. We first derive the hourly profile for each day from AMS data and then scale the hourly profile by the daily filter-based data. The thermodynamic model ISOROPPIA-II (<https://www.epfl.ch/labs/lapi/software/isorropia/>)^{87, 88} was used to compute aerosol pH and partition of soluble species between particulate and gaseous phases. The forward mode with the inputs of total species concentrations (i.e., gas + particle) and meteorological parameters (relative humidity, temperature) gives more accurate results than the reverse mode.⁸⁸⁻⁹¹ Due to a lack of observed ammonia (NH₃) and HNO₃ data, we iterated ISORROPIA-II adopting the predicted NH₃ and HNO₃ to obtain total ammonia (NH₃ and ammonium (NH₄⁺)) and nitrate (HNO₃⁺, NO₃⁻) concentrations as inputs for the next iteration until NH₃ and HNO₃ predictions converge.⁹²

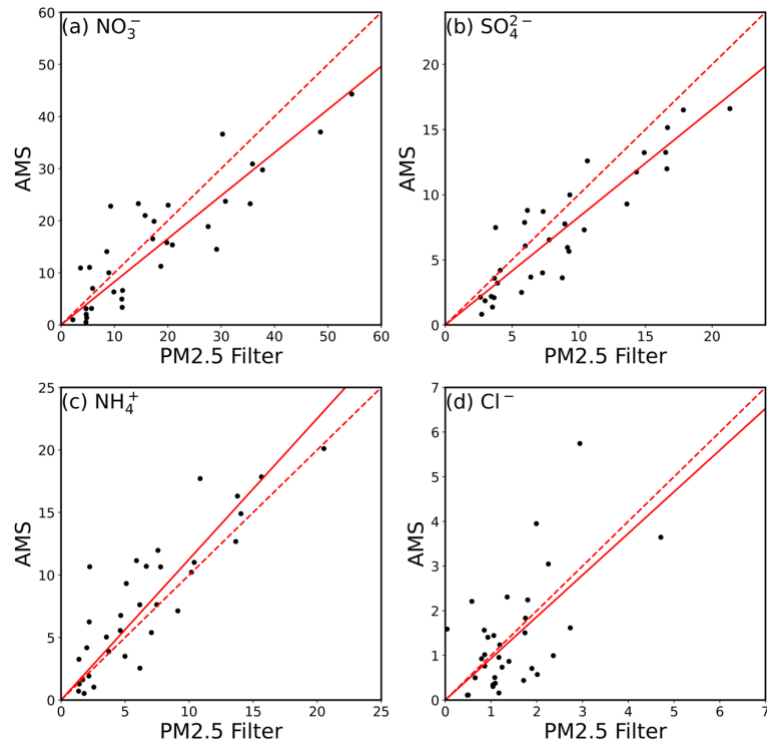


Figure 2. Comparisons of daily AMS and PM_{2.5} filter measurements of aerosol inorganic ions: (a) pNO₃, (b) SO₄²⁻, (c) NH₄⁺, and (d) Cl⁻. Red solid lines denote through-the-origin least-squares regressions and red dashed lines are 1:1 lines.

2.2.3 Photochemical Models, Source Parameterizations, and Simulated cases.

In this chapter, we utilize the Regional chEmical trAnspOrt Model (REAM) in both one- and zero-dimensional configurations^{16, 18, 21, 93} to evaluate the recycling of reactive nitrogen species through heterogeneous HONO production and its impacts on O₃ formation. The model incorporates 30 vertical layers in the troposphere, and the chemistry mechanism is based on the GEOS-Chem model⁹⁴. To ensure realistic meteorological conditions, observed data are used to constrain meteorological parameters such as temperature, RH, wind velocities and directions. Photolysis rates are calculated based on cloud fraction and optical depths simulated by the Weather Research and Forecasting (WRF) model and subsequently scaled using jNO₂ observations. We constrain the model

at a 1-minute time step using surface observations of O₃, NO₂, NO, carbon monoxide (CO), and VOCs.

To investigate the relationship between HONO production and potential production pathways, we calculated the missing HONO source strength (pHONO) by

$$\text{pHONO} = d[\text{HONO}] + L_{\text{chem}} + L_{\text{transport}} - P_{\text{OH+NO}} \quad (6)$$

where, $d[\text{HONO}]$ represents the net change of HONO calculated from observation data for each time step of 1 minute, L_{chem} denotes the chemical loss of HONO through photolysis and gas-phase reactions, $L_{\text{transport}}$ denotes the loss of HONO through vertical transport, and $P_{\text{OH+NO}}$ denotes the production of HONO through the gas-phase reaction of NO and OH. HONO produced from primary emissions is expected to be negligible since the observation site is in a rural coastal region. Previous studies have suggested HONO/NO_x emission ratios ranging from 0.03% to 2.1% depending on fuel types⁹⁵. A brief calculation using emission rate data from the Multi-resolution Emission Inventory for China (MEIC 2017) shows that HONO produced from primary emission is less than 0.01 ppbv/hr, which accounts for less than 1% of the mean daytime missing HONO source in our study. Therefore, HONO production from primary emissions is not considered in our following analysis.

Hourly pHONO data are calculated in the baseline 1-D model simulation by constraining surface HONO and other chemical concentrations to the observations (with the same chemical setup as case B in (Table 2) using Eq (6). To explain observation-based “missing” pHONO, five additional 1-D model simulations were conducted (Table 2). In

case S0, HONO production from NO₂ conversion on ground surface upon dry deposition of NO₂ was parameterized with f equal to 0.24 (Eq. (1)) to reproduce nighttime HONO observations following Liu et al.²¹. As in the previous study, an uptake coefficient of 10^{-6} of NO₂ uptake to aerosol surfaces under dark conditions was assigned⁹⁶.

To reproduce daytime HONO observations, three photoactive HONO production mechanisms were implemented in model simulations on top of S0. The parameters were chosen by considering the values and uncertainties from previous studies and minimizing the simulation errors of daytime HONO simulations. In S1, we considered a first-order enhancement on aerosol uptake of NO₂ from SWR²¹, in which $\gamma = 5 \times 10^{-7} \times \text{SWR}$, to simulate daytime enhancements of pHONO (Eq. (2)). In S2, photolysis of pNO₃⁵⁹ was implemented in two subsets. In S2-1, jpNO₃ was scaled from jHNO₃ by EF = 80 (Eq. (3))⁷⁰. However, a recent study by Andersen et al.⁶¹ indicated that the EF depends on bulk pNO₃ concentrations and can be parameterized as a Langmuir function of pNO₃. In S2-2, EF was computed as a function of the concentration of pNO₃ (Eq. (7))⁹⁷, where $K_L = 0.19 \text{ nmol}^{-1} \text{ m}^3$ is the Langmuir equilibrium constant of nitrate ion, and a is the coefficient to be fitted. In S3, we parameterized HONO produced from surface adsorbed HNO₃ and subsequent photolysis with a yield coefficient (Y_{HONO} , Eq. (4))⁹⁸.

$$\text{EF} = \frac{K_L \times a}{1 + K_L \times [\text{pNO}_3]} \quad (7)$$

A major chemical impact of heterogeneous HONO production in S1-S3 is the recycling of reactive nitrogen. To understand the effect of this recycling on O₃ production rate (PO_3), we conducted a set of Lagrangian free-running box-model simulations (F0 - F3)

to investigate the evolution of plume aging. F0 represents the control case using the same chemical reactions as S0 (case Control). F1 incorporates photosensitized uptake of NO₂ on aerosol surfaces as in S1. F2-1 considers the photolysis of pNO₃ with a constant EF as in S2-1 (EF=80), while F2-2 incorporates a changing EF as in S2-2 (changing EF). Lastly, case F3 includes the production of HONO from HNO₃ as in S3. The models are initialized with average concentrations of observed O₃, NO, NO₂, HONO, CO, and VOCs and started at midnight.

Table 2. Simulation cases.

Cases	Configuration
B	NO + OH + M → HONO + M
S0	B + NO ₂ conversions on ground (f = 0.24) and on aerosols ($\gamma = 10^{-6}$) (Eq. (1))
S1	S0 + photosensitized NO ₂ conversions on aerosol $\gamma = \max(5 \times 10^{-7} \times \text{SWR}, 10^{-6})$ (Eq. (2))
S2-1	S0 + photolysis of pNO ₃ , $\text{jpNO}_3 = 80 \times \text{jHNO}_3$ (Eq. (3))
S2-2	S0 + photolysis of pNO ₃ , $\text{jpNO}_3 = \text{EF}(\text{pNO}_3, a = 3 \times 10^4) \times \text{jHNO}_3$ (Eq. (7))
S3	S0 + HONO from photolysis of HNO ₃ adsorbed on aerosols, $Y_{\text{HONO}} = 0.45$ (Eq. (4))
F0	Free-running S0
F1	F0 + photosensitized NO ₂ conversions on aerosol $\gamma = \max(5 \times 10^{-7} \times \text{SWR}, 10^{-6})$
F2-1	F0 + photolysis of pNO ₃ , $\text{jpNO}_3 = \text{EF} \times \text{jHNO}_3$, EF = 80
F2-2	F0 + photolysis of pNO ₃ , $\text{jpNO}_3 = \text{EF}(\text{pNO}_3, 3 \times 10^4) \times \text{jHNO}_3$
F3	F0 + HONO from HNO ₃ , $Y_{\text{HONO}} = 0.45$

2.3 Results and Discussions

2.3.1 *Observation Overview and Effects of Biomass Burning and Aerosol Acidity*

Figure 3 shows the time series of observed O₃, NO_x, HONO, pNO₃, and S_A during the OPECE campaign. The average HONO concentration was 0.39 ± 0.27 parts per billion by volume (ppbv) with a maximum of 1.54 ppbv recorded at the site. These HONO levels have been reported in measurements from other rural coastal sites in China⁹⁹⁻¹⁰¹, and some urban/suburban areas in Europe such as London¹⁰² and Paris³⁹, much higher than those observed in clean coastal regions¹⁰³. The average concentrations of pNO₃ and S_A were 8 ± 16.8 μg/m³ and 527 ± 382 μm²/cm³, respectively. The diurnal profiles of HONO and other species were also examined (Figure 4). The diurnal profile of HONO illustrates a nighttime accumulation followed by a sharp decrease in the early morning due to rapid photolysis. A slower decrease was observed at noon, indicating the presence of a photoactive daytime HONO source. The average NO_x concentration was 13.6 ± 10.4 ppbv, however, much higher O₃ levels, exceeding 100 ppbv at times, were observed, with an average peak concentration of 70 ppbv. This elevated O₃ level underscores the need to gain a better understanding of springtime photochemistry in China. In this chapter, we focus on investigating the impact of photoactive HONO sources on O₃ enhancements, as explained in more detail in Section 3.3.3.

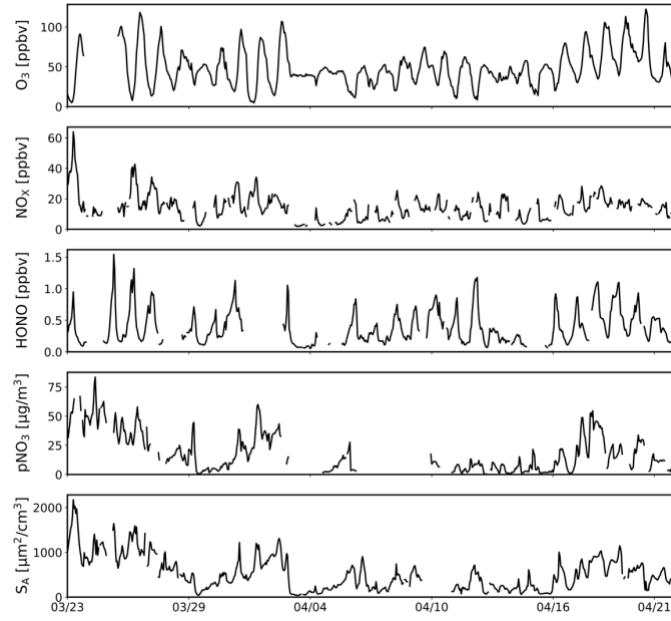


Figure 3. Time series for O₃, NO_x, HONO, pNO₃, and S_A from 23 March to 22 April 2018.

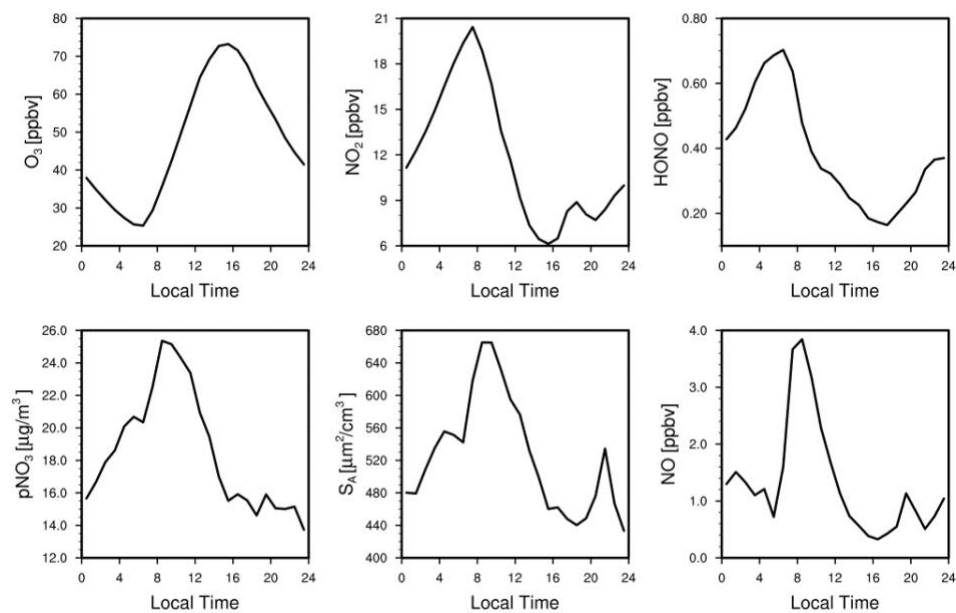


Figure 4. Mean diurnal profiles for observed O₃, NO₂, HONO, pNO₃, S_A, and NO.

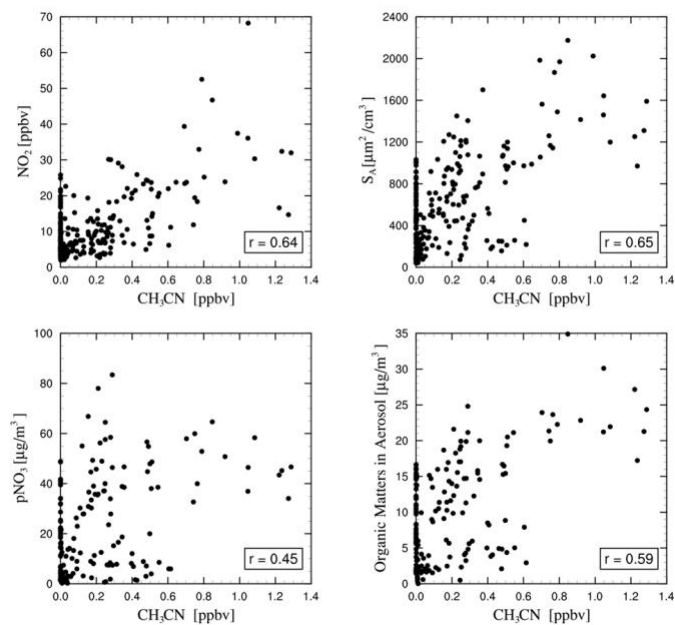


Figure 5. Correlations of CH₃CN with NO₂, pNO₃, S_A and organic matters in aerosol.

BB can significantly contribute to regional air pollution, including HONO, through both direct emissions and secondary production. The long lifetime and source-specific characteristics of CH₃CN make it a widely used tracer for BB¹⁰⁴⁻¹⁰⁷. During the measurement campaign, NO_x, S_A, and organic aerosols showed concurrent enhancements with CH₃CN (Figure 5), indicating the representativeness of CH₃CN as an indicator of BB impact at this site. For observations with elevated levels of CH₃CN, we investigated BB impacts on mixing ratios and production pathways of HONO. Consistent with previous studies^{34, 35, 106, 108, 109}, a positive correlation was found between HONO and CH₃CN concentrations (Figure 6(a)). Previous studies reported BB's acceleration effect on secondary productions of HONO. In our study, we examined the impact on HONO/NO₂ and HONO/pNO₃ ratios, which are used as indicators for NO₂ and pNO₃ conversions to HONO, respectively. Both ratios decrease with higher CH₃CN concentrations (> 0.4 ppbv). To further characterize BB-impacted air masses, we employed a threshold of 0.1 ppbv CH₃CN to define BB-impacted and clean airmasses^{110, 111}. We compared the daytime averaged HONO, HONO/NO₂, and HONO/pNO₃ between these two groups. The average HONO concentrations increased from 0.25 to 0.33 ppbv (Figure 6(c)) due to BB. However, the ratios did not show significant differences, and in some cases, a decrease in the averaged values was observed (Figure 6(d), (e)). We also analyzed data from a fire event near the site on 31 March 2018¹⁴ and compared the ratios in BB and clean airmasses. While HONO was significantly enhanced during the fire event, the median ratios still showed little difference from those of clean airmasses, except for a slightly higher average HONO/NO₂ ratio than that of the clean airmasses. Therefore, the observed enhancement

of HONO associated with BB might be attributed to the increased levels of HONO precursors, such as NO_x or pNO₃, rather than direct emissions of HONO or enhanced conversion efficiencies from its precursors.

In addition to BB, we investigated the impact of aerosol acidity on HONO production (Figure 6 (b)). The average daytime pH varied in a range of 3 to 6, with most values centered around 4. However, no significant relationship was observed between pH and HONO, HONO/NO₂, and HONO/pNO₃. Aerosol acidity may influence HONO production by affecting the partitioning between nitrite (NO₂⁻) and HONO^{76, 77, 112}. Previous studies showed that HONO production from photolysis of pNO₃ increases sharply with decreasing pH in more acidic conditions when the pH is below the acid dissociation constant for HONO (pK_a ~ 3)⁷⁶. The pH range in our study was higher than HONO pK_a values from previous experimental studies^{78, 113, 114}, which may explain the weak dependency of HONO production on pH in our study.

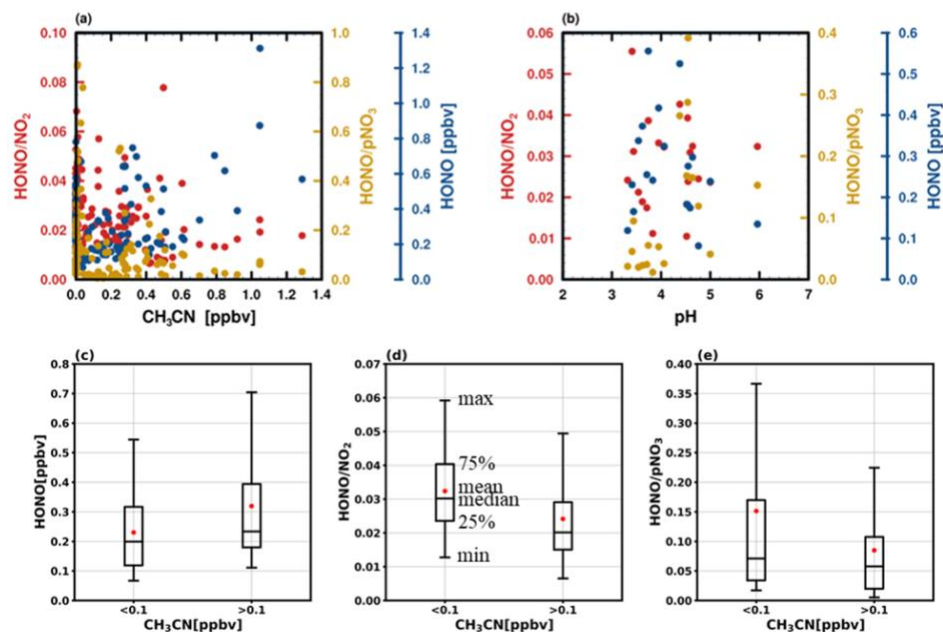


Figure 6. (a) Scatter plot of HONO (blue), HONO/NO₂ (red), and HONO/pNO₃ (yellow) as a function of CH₃CN. (b) Same as (a) but as a function of aerosol pH. (c) Box plots of HONO concentrations for clean and BB airmasses where the mean value is denoted by the red dot. And the median is denoted by black line. (d) and (e) are like (c) but for HONO/NO₂ and HONO/pNO₃, respectively.

2.3.2 Validities of Different Photoactive Heterogeneous HONO Sources

Here we address the question to see if a comprehensive in situ observation dataset can be applied to test the validity of the proposed heterogeneous mechanisms, including photosensitized NO₂ conversion on aerosol, photolysis of pNO₃ and HONO yield from adsorbed HNO₃. A caveat in this analysis is that NO₂, HNO₃, and pNO₃ are all part of the reactive nitrogen family and they have dependent relationships, which are reflected in the correlation analysis. To avoid the impact of BB, we focus on the observations not affected by BB, which comprises 55% of the total available data (Figure 7).

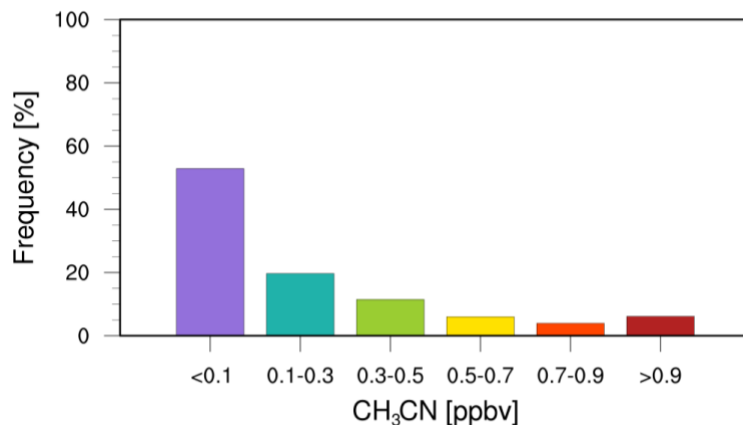


Figure 7. Frequency histogram for observation data points of different levels of CH₃CN.

Figure 8(a) shows a significant positive correlation between pHONO and pNO₃, with a correlation coefficient $r = 0.83$. This correlation strengthens to $r = 0.87$ when considering the case of pNO₃×jHNO₃. Additionally, strong correlation between pHONO and the production rate of HNO₃ from NO₂ (P(HNO₃)) are found with $r = 0.9$. We also find a significant correlation between pHONO and the production terms of photosensitized NO₂ conversion on aerosols, with r increasing from 0.82 between pHONO and NO₂ to 0.90 for that with NO₂×S_A×SWR (Figure 8(b)). These strong correlations reflect the intrinsic relationships among the precursors of heterogeneous HONO production^{115, 116}.

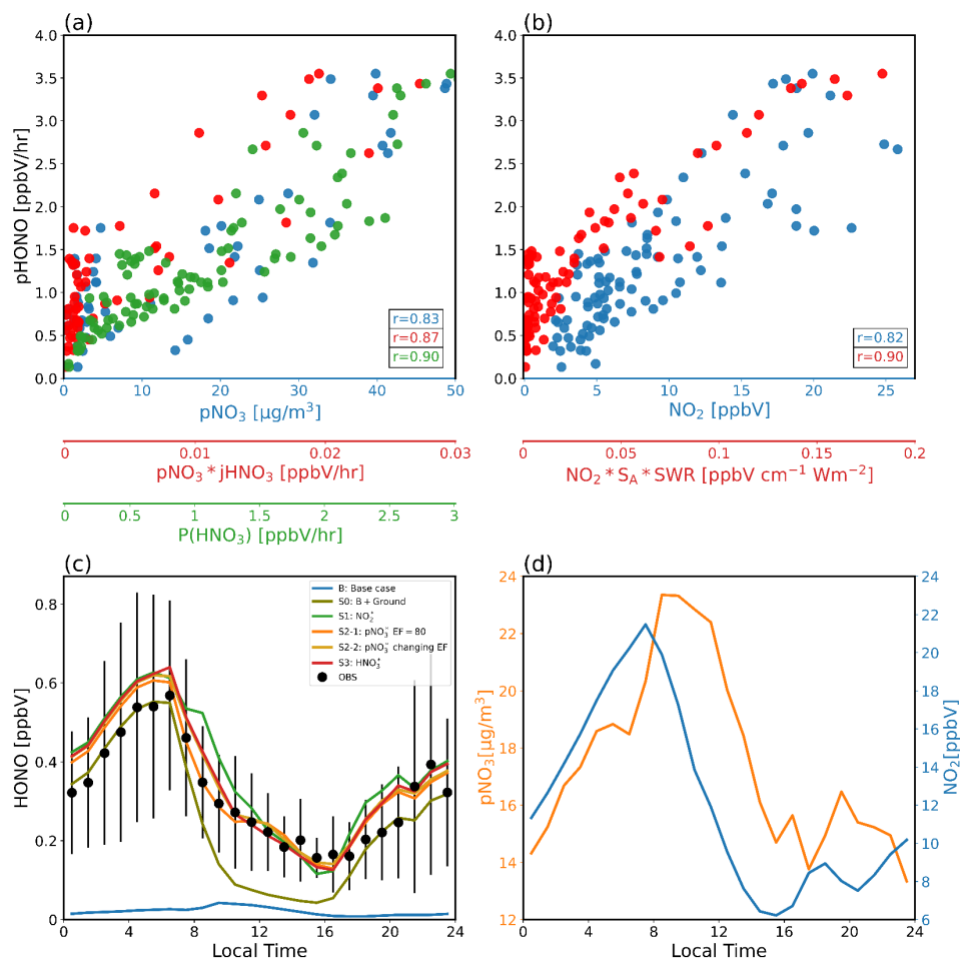


Figure 8. (a) Scatter plot of pHONO as functions of pNO₃ (blue), pNO₃×jHNO₃ (red), and P(HNO₃) (green). (b) Same as (a) but as functions of NO₂ (blue) and NO₂×S_A×SWR (red). The corresponding correlation coefficients are shown at the bottom right corner of the plots. (c) Observed diurnal HONO (black dots) with standard deviation (black vertical lines) and simulated HONO under the six cases (B, S0-S3) as described in Table 2. Simulation cases. (d) Mean diurnal profiles of pNO₃ (orange) and NO₂ (blue) during the measurement period. All panels show the non-BB data.

To further assess the photoactive HONO production mechanisms, we conducted a set of constrained simulations (S0-S3, Table 2) incorporating additional HONO sources as described in Section 2.2.3. Consistent with previous studies, the observed HONO levels consistently exceed those predicted by R1 (Figure 8(c): B) throughout the day. Nocturnal

HONO levels are explained by heterogeneous NO_2 conversion on the ground surface with $f = 0.24$, while daytime HONO concentrations remain underestimated (Figure 8(c): S0).

After incorporating photoactive HONO production mechanisms (S1-S3), the model with any one of the mechanisms can reproduce the observed HONO levels within one standard deviation of the observations (Figure 8(c): S1-S3). Importantly, the derived key parameters for HONO production, obtained by minimizing the simulation errors, are comparable to those reported in previous experimental and modeling studies (Table 3). This agreement underscores the difficulty of assessing the underlying HONO heterogeneous production mechanism due to the intrinsic relationships among reactive nitrogen species. For example, higher HONO concentrations can promote pNO_3 production⁴⁵, and the photolysis of pNO_3 can recycle reactive nitrogen from a reservoir species back into more reactive gaseous species, thereby sustaining atmospheric NO_2 levels¹¹⁷⁻¹¹⁹. Moreover, as atmospheric HNO_3 is produced through the reaction of OH and NO_2 , the production rate of HONO via this process is directly proportional to NO_2 . Given these intertwined relationships, it becomes challenging to establish a definitive causal relationship between HONO production and the proposed mechanisms solely through photochemical analysis of in situ observations.

Table 3. Comparisons of HONO source parameterizations to previous studies.

Location	Time	γ		jpNO ₃ [s ⁻¹]	Y _{HONO}	Ref.
Experimental		3×10^{-4}				57
Experimental					0.53	98
Beijing, China	Aug 2007	$10^{-4} \times k_{\text{SWR}}^1$				21
Houston, TX, US	Apr- May 2009	$6 \times 10^{-5} \times k_{\text{jNO}_2}^2$				120
Dallas, TX, US	Jun 2011	8.5×10^{-4}				121
Hong Kong, China	Aug 2011	$5 \times 10^{-5} \times k_{\text{SWR}}$				122
NY, US	Multiple years			$(1.3 \pm 1.2) \times 10^{-4}$		59
Wangdu, Hebei, China	Jun - Jul 2014	$10^{-3} \times k_{\text{jNO}_2}$	and	1.3×10^{-4} 1.3×10^{-4}		70
Experimental	Apr - Dec 2016			8.2×10^{-5} 8.2×10^{-5}		123
Nanjing, Jiangsu, China	May - Jun 2016	$2 \times 10^{-5} \times k_{\text{jNO}_2}$	and	$208 \times \text{jHNO}_3$		71
Optimal γ	Multiple cases	$5 \times 10^{-4} \times k_{\text{SWR}}$				27
Changzhou, Jiangsu, China	Apr 2017	$2 \times 10^{-5} \times k_{\text{jNO}_2}$	and	$119 \times \text{jHNO}_3$		72
Beijing, China	Apr - May 2018	$1.1 \times 10^{-4} \times k_{\text{SWR}}$	and	$119 \times \text{jHNO}_3$		115
Beijing, China	May - Jul 2018	$10^{-4} \times k_{\text{jNO}_2}$	and	$119 \times \text{jHNO}_3$		124
Beijing, China	Nov 2018 - Jan 2019	$6 \times 10^{-5} \times k_{\text{jNO}_2}$	and	$119 \times \text{jHNO}_3$		124
Dongying, Shandong, China	Mar - Apr 2018	$5 \times 10^{-4} \times k_{\text{SWR}}$	or	EF \times jHNO ₃ , EF=80 or [20, 3600] with a median of 106	or 0.45	This study

¹ $k_{\text{SWR}} = \text{SWR}/1000$.

² $k_{\text{jNO}_2} = \text{jNO}_2 / [\text{jNO}_2 \text{ at noon}]$

However, these mechanisms have very different implications for the recycling of reactive nitrogen. The conversion from NO_2 to HONO has the lowest impact since both species are short-lived. The ratio of pNO_3 to total nitrate from ISORROPIA results shows a contribution of pNO_3 always higher than 90%, suggesting that in springtime, the gas-particulate partitioning of nitrate strongly favors the formation of pNO_3 from gaseous HNO_3 . Therefore, the conversion of HNO_3 to HONO reduces the lifetime of HNO_3 and the formation of pNO_3 , effectively enhancing the recycling of reactive nitrogen. The photolysis of pNO_3 significantly reduces the lifetime of the most long-lived reactive nitrogen reservoir and makes the entire inorganic reactive nitrogen family photochemically active, speeding up the recycling of reactive nitrogen the most.

2.3.3 Sensitivity of O_3 Production to Heterogeneous HONO Sources

The drastically different implications of the heterogeneous HONO production mechanisms on the recycling of reactive nitrogen also strongly affect the production and concentration of O_3 . We use Lagrangian box model simulations to analyze the chemical evolutions of isolated airmasses and investigate the consequences of the heterogeneous HONO production mechanisms (Table 2: F0 – F3). Figure 9(a) shows the divergent evolutions of O_3 , NO_x , OH, and PO_3 among the HONO production mechanisms. Compared to F0 without HONO production from aerosols, photoactive conversion of NO_2 (F1) or adsorbed HNO_3 to HONO (F3) has a transient impact on reactive nitrogen, OH, and O_3 , while the impact from HONO production from pNO_3 is much larger and longer lasting. The difference lies in how the heterogeneous HONO production mechanism affects the recycling between NO_x and pNO_3 . The conversion of NO_2 to HONO on aerosols

partitions reactive nitrogen into HONO, which effectively reduces the conversion from NO_x to pNO₃. In the case of F3, photolysis of adsorbed HNO₃ back to HONO reduces the production of HNO₃ and hence the concentration of pNO₃ by nearly half. Photolysis of HONO adds a larger radical source and can speed up O₃ production¹⁷. However, one O₃ is lost for each conversion of NO₂ to HONO. The conversion from HNO₃ to HONO does not incur this O₃ loss and therefore produces more O₃ than the conversion from NO₂ to HONO (Figure 9(b)). The effects are most obvious in the first day but diminish over time as reactions of NO_x produce pNO₃, which is a permanent sink of reactive nitrogen in these two cases.

In cases F2-1 and F2-2, however, the conversion of pNO₃ to HONO allows a full recycling of inorganic reactive nitrogen species^{119, 125-127}. Daytime HONO and NO_x concentrations are sustained at significant levels, leading to high OH concentrations and O₃ production and a tripling of O₃ concentrations of > 100 ppbv after a week (Figure 9(a)). The increase of O₃ is twice as much in F2-1 and F2-2 as that of F0, F1 or F3 (Figure 9(b)). The difference between F2-1 and F2-2 is smaller compared to their differences from F1 and F3. A recent study¹²⁸ implementing HONO conversion from NO₂ and pNO₃ into a chemistry-climate model found a reduction effect on O₃ driven by HONO conversion from NO₂ and a strong enhancement of NO_x caused by HONO conversion from pNO₃. A necessary condition to simulate an O₃ reduction is that NO from HONO photolysis can only produce a fractional (<1) O₃ despite the additional OH from HONO photolysis. This could occur when OH reacts with O₃ due to a lack of reactive VOCs. Figure 9 shows that it is not the case in a polluted boundary layer.

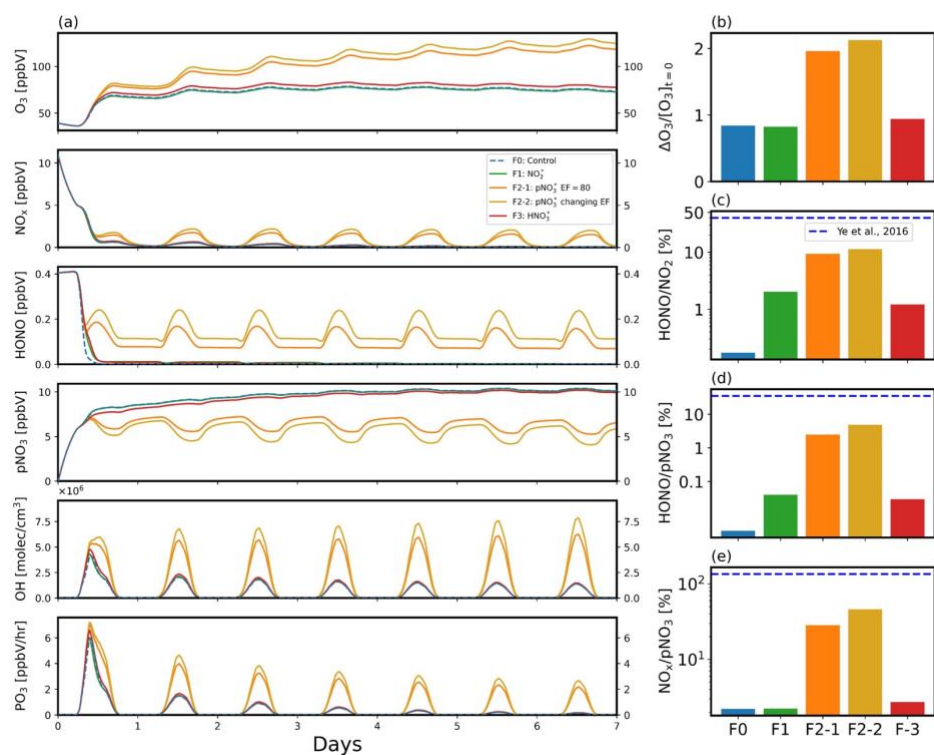


Figure 9. Simulated evolutions of O₃, NO_x, HONO, pNO₃, OH, and PO₃ in a Lagrangian box model for seven days under cases F0 – F3. (b) O₃ enhancement ratios, defined as the relative O₃ increase from the initial O₃ concentration for cases F0 – F3. (c), (d), and (e) are simulated evolutions of HONO/NO₂, HONO/pNO₃ and NO_x/pNO₃ ratios. The dashed lines denote measured HONO/NO₂, HONO/pNO₃ and NO_x/pNO₃ values from Ye et al.¹¹⁷.

Ye et al.¹¹⁷ reported rapid cycling of pNO₃ to HONO from aircraft measurements over the North Atlantic Ocean in the marine boundary layer, based on observed high HONO production with low-level NO_x present. We reexamined their observation data using the simulation results from OPECE. Following the observation-model comparison procedure by Ye et al., we used model outputs at 2:30 pm on the 2nd diurnal cycle, which represents a 1.5-day airmass transport from the coastal site in the marine boundary layer, to be compared to their observations. The observed HONO/NO₂, HONO/pNO₃, and

NO_x/pNO₃ ratios reported by Ye et al. are much higher than our simulation results (Figure 9 (c) - (e)), although our observations during OPECE are more comparable to the observed values reported by other ground-based studies (Table 4). Therefore, the marine observations by Ye et al. appear to suggest a chemical environment of extremely high recycling of reactive nitrogen not seen over polluted land areas^{103, 129}.

Figure 9 (b) shows that O₃ production rate can be much higher from the pNO₃ conversion mechanism (F2-1 and F2-2) than the two other mechanisms (F1 and F3) in comparison to the case of no heterogeneous HONO production (F0). However, the effects depend on the amount of reactive nitrogen. To illustrate this dependence, we conducted box model simulations for 3 hours under noontime conditions with initial NO_x mixing ratios in the range of 1-25 ppbv. Similar results are obtained when longer integration hours are used, but the differences of F2-1 and F2-2 from the other cases increase with time.

Table 4. Comparisons of HONO/NO₂ and HONO/pNO₃ of different studies.

Location	Time	HONO/NO ₂	HONO/pNO ₃	Reference
Beijing, China	Aug 2007	9.5%		21
Houston, TX, US	Apr - May 2009	2.5%		120
Dallas, TX, US	Jun 2011	1%		121
Hong Kong, China	Aug 2011	2.6%		122
Wangdu, Hebei, China	Jun - Jul 2014	5%	14%	70
Cape Verde GAW station	2014 - 2015	13%	0.9%	126
Nanjing, Jiangsu, China	May - Jun 2016	5%	12%	71
Changzhou, Jiangsu, China	Apr 2017	6.8%	41%	72
Beijing, China	Apr - May 2018	11%		115
Beijing, China	May - Jul 2018	7%		124
Beijing, China	Nov 2018 - Jan 2019	5%		124
Dongying, Shandong, China	Mar - Apr 2018	4.3%	4.1%	This study

A few features emerge from the modeling analysis. Figure 10(a) shows the cumulative PO_3 first increases with NO_x and then starts to decrease with increasing NO_x . The NO_x concentration at which the cumulative PO_3 maximizes is the transition from NO_x -limited to VOC-limited O_3 production^{17, 18}. The critical initial NO_x concentration for this transition increases when heterogeneous HONO production is introduced (Figure 10). The largest increase occurs with the NO_2 conversion mechanism (F1) because the OH production from HONO photolysis speeds up the conversion of NO_x to its reservoir HNO_3 . In F2 and F3 cases, HNO_3 can be effectively recycled back to NO_x but not in F1. Consequently, the reduction of NO_x is fastest in F1 due to HONO production. In a polluted urban-like environment where O_3 production rate is lower at higher NO_x concentrations, the faster NO_x reduction tends to increase PO_3 . As the urban plume ages, however, it is expected that pNO_3 recycling (F2-1 and F2-2) will increase PO_3 much more than NO_2 recycling (F1). Figure 11 shows the ozone production efficiency (OPE), defined as the cumulative PO_3 in a three-hour period (ΔO_3) per NO_x consumed (ΔNO_x) as a function of initial NO_x concentration. The NO_2 conversion case (F1) is slightly higher than the case without heterogeneous HONO production (F0) under high- NO_x conditions. The pNO_3 conversion case (F2-1 and F2-2) increases OPE by a factor of 2-4 compared to F0. The HNO_3 conversion case (F3) is more similar to (and higher than) the NO_2 conversion case (F1) under low NO_x conditions and approaches the pNO_3 conversion cases (F2-1 and F2-2) under high NO_x conditions.

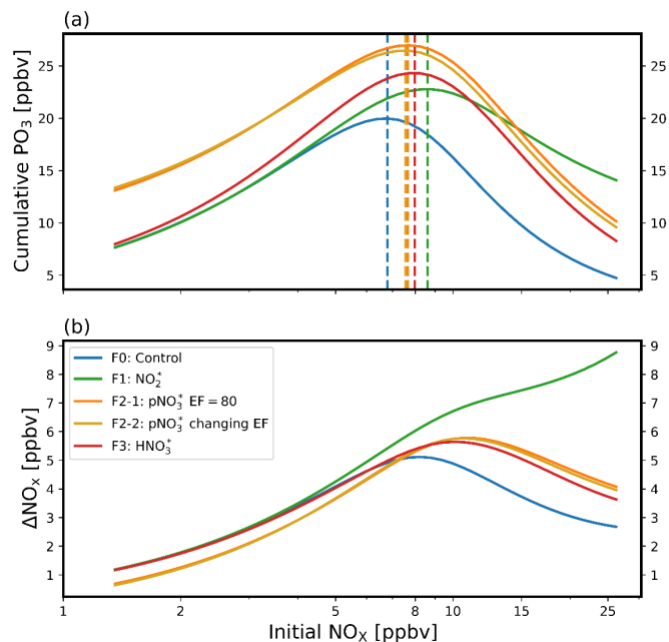


Figure 10. (a) Cumulative PO₃ as a function of initial NO_x for cases F0 - F3. The dashed lines denote NO_x levels at which cumulative PO₃ reaches its peak values. (b) Loss of NO_x (ΔNO_x) as a function of initial NO_x.

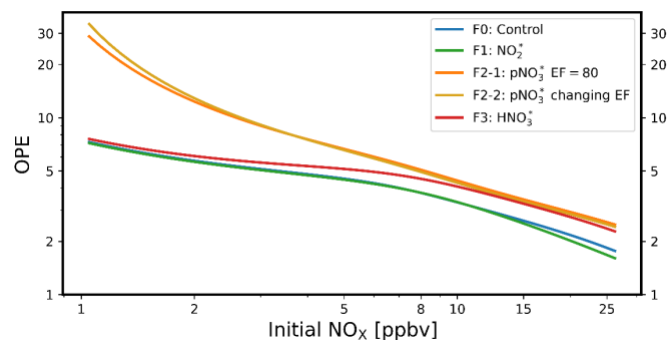


Figure 11. Ozone production efficiency (OPE) as a function of initial NO_x concentrations for cases F0 - F3.

2.4 Conclusion

Modeling analysis of the OPECE gaseous and particulate measurements at a rural coastal site shows clear evidence for daytime heterogeneous production of HONO on

aerosols in agreement with previous studies. High HONO concentrations from recent fires can be attributed to the increased level of HONO precursors, such as NO_x or pNO₃, rather than primary emissions of HONO. By incorporating either photosensitized NO₂ conversion on aerosols, photolysis of pNO₃, or photolysis of surface adsorbed HNO₃ on aerosols, the model can reproduce the observed HONO concentrations when other reactive nitrogen and chemical species are constrained by the observations. This modeling equivalency reflects the intrinsic relationships between NO₂, pNO₃, and HNO₃ in the chemical system, indicating that inland in situ observations may not provide sufficient constraints to investigate the underlying mechanism of heterogeneous HONO production. It appears necessary to conduct Lagrangian experiments away from sources such as in the marine boundary layer since the three mechanisms have drastically different predictions of HONO/NO₂, HONO/pNO₃, and NO_x/pNO₃ ratios (Figure 9(c)-(e)) after 1-2 days of chemical aging. Being able to follow the evolutions of these ratios can provide more information on the underlying mechanism.

The maritime observations by Ye et al.¹¹⁷ are not as ideal as a Lagrangian experiment but can be carried out more easily. Their observations suggest a chemical environment of much faster reactive nitrogen recycling than the one found in OPECE or other inland datasets, which may indicate additional processes contribute to efficient reactive nitrogen recycling through HONO production over the ocean. However, it also implies much higher O₃ production in offshore regions than in current model predictions. A survey of OPECE observations did not provide evidence for high O₃ air mass transport from offshore regions, which may be related to prevailing westerly conditions during OPECE.

Quantifying the mechanism of heterogeneous HONO production on aerosols has profound implications for understanding O₃ pollution and is important to formulating effective O₃ mitigation strategies. The conversion of HONO from pNO₃ can drastically increase the lifetime of NO_x and the cumulative O₃ production during the aging process far away from emission sources (Figure 9 and Figure 10) compared to the other two mechanisms. It has the potential to substantially elevate O₃ concentrations in regions located downwind from emission sources and to amplify O₃ levels even in distant marine environments, potentially exerting a global influence.

On the other hand, the conversion of HONO from NO₂ on aerosols can move the transition regime, when O₃ production becomes insensitive to NO_x, into higher NO_x conditions and significantly flatten the PO₃ increase as NO_x decreases under high NO_x conditions (Figure 10(a)) compared to the other mechanisms or the case without heterogeneous HONO production. The faster removal of NO_x (Figure 10(b)) also implies a lower effect of background O₃ production in downwind regions on urban O₃ compared to the other cases since the OPEs of case F1 are among the lowest under low NO_x conditions (Figure 11). The net effect is to reduce O₃ sensitivity to NO_x changes. It may help explain the observations that O₃ concentrations in China have not changed much over the past decade despite a ~50% reduction in NO_x (Figure 12)^{6, 130-132}.

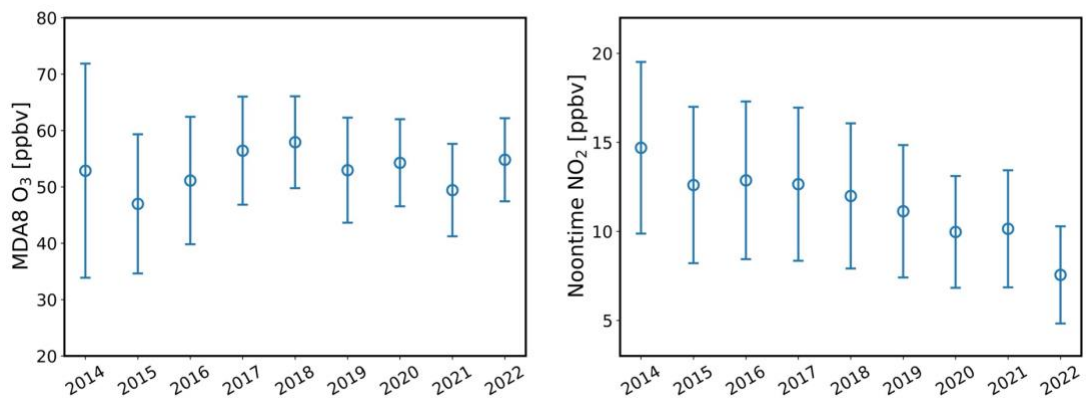


Figure 12. Annual mean maximum daily average 8-hr (MDA8) O₃ concentrations (left) and annual mean noontime NO₂ concentrations (right) for eastern China from 2014 to 2022.

CHAPTER 3. REMOTE SENSING MEASUREMENTS AT A RURAL SITE IN CHINA: IMPLICATIONS FOR SATELLITE NO₂ AND HCHO MEASUREMENT UNCERTAINTY AND EMISSIONS FROM FIRES

3.1 Introduction

Nitrogen dioxide (NO₂) and formaldehyde (HCHO) play critical roles in the tropospheric photochemical processes^{1, 133-135}. NO₂ is an essential precursor for ozone (O₃) production in the troposphere and has both natural and anthropogenic sources^{22, 136-138}. HCHO is produced during the oxidation of volatile organic compounds (VOCs), contributing to the productions of O₃ and aerosols. In the remote atmosphere, HCHO is mainly produced from methane oxidation. Over the continents, it is mainly produced by the oxidation of non-methane VOCs emitted from biogenic and anthropogenic sources. Consequently, these emissions can be detected through the enhancements of short-lived HCHO^{17, 18, 139, 140}.

Observations of these trace gases provide valuable information to understand photochemical processes. Compared with surface measurements, which are limited in spatiotemporal coverages, satellite observations of tropospheric vertical column densities (TVCDs) can provide continuous datasets with a broad spatial range. The Ozone Monitoring Instrument (OMI) and the TROPOspheric Monitoring Instrument (TROPOMI) have provided continuous measurements of NO₂ and HCHO to advance our understanding

of the related atmospheric chemical processes^{15, 141-146}. OMI aboard NASA's Aura satellite has been in orbit since 2004. It has a local overpass time of around 13:45 local time (LT) and a $13 \times 24 \text{ km}^2$ nadir resolution¹⁴⁷. TROPOMI onboard the European Copernicus Sentinel-5 Precursor (S5P) satellite was launched in 2017 and has extended the historical time series of midday observations from OMI with a local overpass time around 13:30 and an improved spatial resolution of $7 \times 3.5 \text{ km}^2$ ($5.5 \times 3.5 \text{ km}^2$ after August 2019)¹⁴⁸. Both OMI and TROPOMI measure the backscattered radiance and solar irradiance in the visible and ultraviolet bands. The spectral windows of 328.5 - 359/356.5nm and 402/405 - 465nm are typically used to retrieve HCHO and NO₂ TVCDs, respectively^{149, 150}.

The increasing capability of satellite monitoring from space has enabled studies to better characterize pollution patterns, such as analyzing the responses of trace gases to either anthropogenic or biogenic sources^{142, 151, 152} and investigating regional emission trends^{15, 153, 154}. The uncertainties of satellite products consist of both systematic and random components. In rural regions, where TVCDs are usually low, satellite observations are subject to significant uncertainties i.e., 45% - 105% as reported in previous studies^{155, 156}. Validations of satellite observations are of particular interest to understanding sources of errors and improving retrieval accuracies¹⁵⁷⁻¹⁶⁰.

The multi-axis differential optical absorption spectroscopy (MAX-DOAS) instrument has been developed^{161, 162} to simultaneously measure column densities of trace gases, including NO₂ and HCHO. Observing at multiple elevation angles, it can provide enhanced signals for low elevations with a horizontal spatial representativeness of the same order or even finer than the spatial resolution of satellite observations¹⁶³, thus has been

utilized in assessments of satellite products. Such studies can be validations of a single satellite product¹⁶⁴⁻¹⁶⁹ or intercomparisons of several satellite products^{166, 170, 171}.

In addition to satellite validations, the simultaneous multicomponent observations from MAX-DOAS provide valuable vertical observational constraints of pollutants. These synchronous measurements have been utilized to analyze the fast-changing evolutions of complex photochemical processes, especially in relation to the impacts of biomass burnings (BB) on trace gases and aerosols. For instance, researchers have employed MAX-DOAS measured HCHO as a tracer for absorption aerosols to investigate brown carbon emissions from BB plumes at different stages¹⁷². Other MAX-DOAS studies have focused on examining photochemical processes, such as ozone formation sensitivities¹⁷³ and the production mechanisms of nitrous acid (HONO), which has gained significant attention in recent years due to its potentially large impact on hydroxyl radicals (OH)^{174, 175}.

In this chapter, we analyze MAX-DOAS observation at a rural coastal site in the Shandong province, China. On days when local fire emissions are minimal, we use these observations to evaluate different satellite products for NO₂ and HCHO TVCDs from OMI and TROPOMI. On days with active burning, we investigate the enhancements HONO, NO₂, and HCHO due to nearby agriculture burnings using MAX-DOAS observed vertical profiles of trace gases and aerosol extinction. We first provide descriptions of the satellite and MAX-DOAS observations in section 3.2. We give an overview of intercomparison in section 3.3.1, analyze the reasons for satellite differences in section 3.3.2, investigate the HONO and HCHO enhancements from BB events in section 3.3.3, and provide a summary in section 3.4.

3.2 Method

3.2.1 Ground-based MAX-DOAS Measurement

We obtained ground-based MAX-DOAS measurements from the Ozone Photochemistry and Export from China Experiment (OPECE) at a rural site located on the east coast of the Shandong province, between Mar 08 and Apr 26, 2018. The site (37.76°N , 118.98°E) is 200-300 km downwind from the heavily polluted center of North China Plain (NCP), located at the estuary of the Yellow River near a national bird sanctuary (Figure 13). It is surrounded by crops and some off-line oil fields, and the city of Dongying, 50 km to the southwest of the site, is the only known area nearby with concentrated pollution emissions¹⁴. The expansive flat terrain encompassing the site provides an optimal setting for remote sensing measurements.

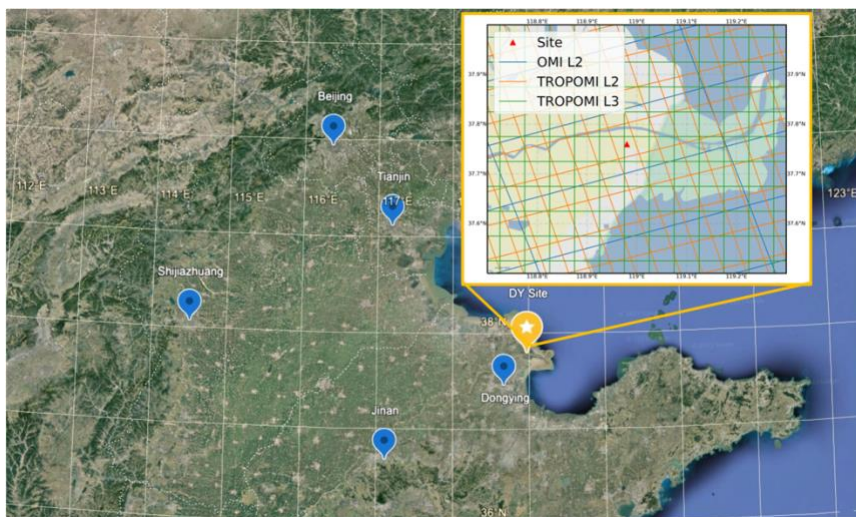


Figure 13. The observation site (yellow marker) and large cities (blue markers) (from Google Earth). The upper right panel shows the site location and satellite observation pixel grids for OMI L2, TROPOMI L2, and TROPOMI L3 products.

Vertical profiles of NO₂, HCHO, HONO, sulfur dioxide (SO₂), and aerosol extinction coefficients (AEC) are obtained to evaluate satellite products on non-burning days and analyze agriculture burning impacts on burning days using a commercial MAX-DOAS instrument^{176, 177}. The instrument has a spectral range between 300 - 460 nm with a spectral resolution of ~ 0.6 nm full width at half maximum (FWHM)^{174, 178}. Spectral observations were conducted at various elevation viewing angles controlled by a built-in mechanical processor. Detailed information about the instrumental operations can be found in previous works^{179, 180}. Differential slant column densities computed from the observed spectra by the QDOAS software¹⁸¹ were combined with the differential air mass factors to derive the vertical column densities. Trace gas profiles were retrieved based on the optimal estimation method¹⁸² using a forward radiative transfer model^{162, 179, 180}. In this study, data measured with a solar zenith angle > 75°, or DOAS fitting results with root mean square of residuals larger than 10⁻³ were filtered out.

Compared to surface and satellite observations, the MAX-DOAS instrument offers the advantage of measuring the vertical distribution of the boundary and upper layers. The average errors for near-surface (0-100m) concentrations of NO₂, HCHO, HONO, and SO₂ were 0.1, 0.04, 0.14, and 0.16 parts per billion by volume (ppbv), respectively, and 0.11 for AEC, consistent with previous studies^{174, 183}. The MAX-DOAS data extends from the surface to 3 km (2.6 km for HONO and SO₂) at a 15-minute time step and a vertical resolution of around 100 m below 2km and 200m above. Additionally, corresponding

averaging kernels (AVKs) for each species are provided, which indicate good sensitivities of MAX-DOAS measurements within the boundary layer.

3.2.2 Satellite Products and AMF Calculations

In this chapter, we utilized six satellite products in total, and for simplicity purposes, we listed their abbreviations in Table 5. We obtained three Level-2 (L2) NO₂ TVCD products, including two OMI products: OMNO2 v4.0 from NASA ¹⁸⁴ and QA4ECV NO₂ v1.0 from KNMI ¹⁸⁵, as well as the TROPOMI v1.0.1 operational product ¹⁸⁶. We note that significant advancements in TROPOMI NO₂ products have been made since the v1.0.1 version. However, the newer TROPOMI product is unavailable for our study period (Mar - Apr 2018), which was during the commissioning phase of TROPOMI. We implemented cloud corrections to correct the bias in the TROPOMI v1 products.

Table 5. Satellite products and their abbreviations used in this work.

Species	Data Product	Abbreviations
NO ₂	OMNO2 v4.0	OMI-NASA, NASA_REAM
NO ₂	QA4ECV NO ₂ v1.0	OMI-KNMI, KNMI_REAM
NO ₂	TROPOMI v1.0.1	TROPOMI, TROPOMI_REAM
HCHO	OMHCHO v3	OMI-NASA, NASA_REAM
HCHO	QA4ECV HCHO v1.2	OMI-BIRA, BIRA_REAM
HCHO	TROPOMI L3	TROPOMI

The retrieval process for NO₂ TVCDs involves three steps: (1) fitting the slant column densities (SCDs) from the measured spectrum data using the differential optical absorption spectroscopy (DOAS) spectral fitting method ¹⁸⁷, (2) separating tropospheric SCDs (TSCDs) from the stratospheric SCDs, and (3) computing the tropospheric air mass

factors (AMFs) based on scattering weights and a priori NO₂ profiles. The TVCDs are then obtained by dividing TSCDs by the AMFs¹⁸⁷⁻¹⁸⁹. The NASA and KNMI OMI NO₂ products differ in the processes of spectral fitting, tropospheric-stratospheric separation, and AMF calculation^{185, 189-191}. The retrieval uncertainties for NO₂ TVCDs are approximately 30% under clear sky conditions and can be even higher in cloudy conditions^{185, 192-194}.

For HCHO TVCDs, we utilized the QA4ECV HCHO v1.2 product by the European consortium (BIRA, IUP, MPIC, KNMI, WUR)^{195, 196} and OMHCHO v3 product from NASA¹⁹⁷. As the TROPOMI L2 HCHO product¹⁹⁸ is not available for our study period, we obtained 0.05°×0.05° L3 daily data processed by the BIRA team¹⁶⁶. The retrieval process for HCHO TVCDs consists of three steps, (1) fitting the SCDs from the ultraviolet (UV) part of the spectra, (2) converting the SCDs to TVCDs using air mass factors retrieved from a look-up table, and (3) performing a background correction to correct for global offset and other factors. Therefore, the retrieved HCHO TVCD can be expressed as follows:

$$N_v = \frac{N_s - N_{s0}}{M} + N_{v0} \quad (8)$$

where M is the air mass factor, N_s is the SCD, N_{s0} and N_{v0} are the reference sector correction terms. More details can be found in the algorithm papers¹⁹⁸. The uncertainties of satellite HCHO products are related to pollution conditions and can be greater than 45%

as shown in a previous study¹⁵⁶, partly due to the nature of stronger Rayleigh scattering in the UV band, which limits the sensitivity to HCHO, especially in the lower atmosphere¹⁹⁹.

The extensive utilizations of OMI and TROPOMI products worldwide^{15, 132, 194, 200-204} highlight the importance to ensure reliable data quality and mitigate factors that could contribute to the deviations among different products in the intercomparisons. To ensure the quality of data used in our study, we followed the instructions in the corresponding README files^{149, 150, 186, 205} to filter out any invalid or failed retrievals for all the satellite products. Specific quality filters used in this study are listed in Table 6.

Table 6. Quality filters applied to satellite products.

Product	Filters	References
OMNO2 v4.0	The least-significant bit of vcdQualityFlags is 0 & SolarZenithAngle < 85 & cloud fraction < 30% & XTrackQualityFlags = 0 or 255	Table 4 from ¹⁵⁰
QA4ECV NO ₂ v1.0	processing_error_flag=0 & solar_zenith_angle < 80 & snow_ice_flag < 10 & amf_trop/amf_geo > 0.2 & cloud radiance fraction no2 <=0.5	²⁰⁵
TROPOMI v1.0.1	quality assurance value >0.75	Table 6 of the ATBD file ¹⁸⁶
OMHCHO v3	MainDataQualityFlag = 0	
QA4ECV HCHO v1.2	processing quality flags = 0	
TROPOMI L3	we use all non-missing data	

Furthermore, it is important to consider the variations introduced by the use of different a priori profiles in the retrievals of OMI and TROPOMI products (e.g.,²⁰⁶⁻²⁰⁸. NASA retrievals employ monthly mean NO₂ profiles from the Global Modeling Initiative (GMI) model at 1°×1.25°, as well as the monthly mean HCHO profiles from the GEOS-

Chem model at a resolution of $2^\circ \times 2.5^\circ$ ^{209, 210}. On the other hand, TROPOMI and KNMI retrievals utilize daily NO₂ or HCHO profiles from the Tracer Model version 5 (TM5-MP) at $1^\circ \times 1^\circ$ resolution^{186, 205, 211}.

In this chapter, we employed consistent a priori profiles simulated by the Regional Chemical transport Model (REAM) in satellite and MAX-DOAS retrievals to facilitate the intercomparisons. REAM has been widely applied in previous studies^{15, 22, 194}. It is a regional chemistry transport model with boundary conditions obtained from a $2^\circ \times 2.5^\circ$ simulation from the GEOS-Chem model. REAM has a horizontal resolution of 36 km and 30 vertical layers in the troposphere, driven by meteorology fields from the Weather Research and Forecasting (WRF) model. The chemistry mechanism is based on the GEOS-Chem model, with anthropogenic emissions adopted from the Multiresolution Emission Inventory for China and biogenic isoprene emissions from the Model of Emissions of Gases and Aerosols from Nature²¹². For our study, we run REAM simulation for March and April 2018 to obtain a priori profiles of NO₂ and HCHO.

To ensure consistency in our intercomparisons of different products^{192, 213}, we calculated AMFs using REAM a priori profiles (AMF_{REAM}) as $AMF_{REAM} = \frac{\sum_i V_{i,REAM} W_i}{\sum_i V_{i,REAM}}$, where $V_{i,REAM}$ is the VCD for vertical layer i , and W_i is the scattering weight for that layer. While NASA products provide the scattering weight data, the other products offer AVKs. The scattering weight vector (\mathbf{W}) can be computed as $\mathbf{W} = \mathbf{AVK} * AMF$, where the AVKs are multiplied by the tropospheric AMF¹⁸⁸.

Studies have suggested a low bias in TROPOMI NO₂ product up to v1.3 due to cloud pressure retrieval biases^{191, 214}. However, the newer versions (since v1.4) with the updated cloud algorithms^{215, 216} do not cover our study period (Mar - Apr 2018). Therefore, for the TROPOMI NO₂ product, we performed cloud pressure corrections by replacing the original cloud pressure data with those provided by either of the two OMI products. The AMF of a partially clouded pixel is calculated as a linear combination of a cloudy AMF (AMF_{cl}) and a clear AMF (AMF_{clr}), as shown in Eq. (9), where f_r is the cloud radiance fraction^{158, 217}. On TROPOMI cloudy days, i.e., when TROPOMI cloud radiance fraction > 0, the mean cloud pressures for OMI-NASA, OMI-KNMI, and TROPOMI v1.0.1 are 800, 674, and 953 hPa, respectively (Figure 14). On days when the specific OMI cloud data is not available, we used a scaling factor, which is the ratio between cloud pressures of OMI to TROPOMI, 0.8 for OMI-NASA and 0.7 for OMI-KNMI, to scale the TROPOMI cloud pressures. The relative change of NO₂ TVCDs, due to different selections of OMI cloud pressures, was 2.5%, a considerably smaller change compared to the 29.7% shift observed before and after applying cloud correction (Figure 15). Despite the OMI-KNMI's lower mean cloud pressure compared to OMI-NASA, the impact of OMI cloud pressure choices on the results appears relatively insignificant in comparison to the substantial change due to cloud correction. For the following analysis, we will use TROPOMI products that have been corrected by corresponding OMI-NASA cloud pressure data as in Eq. (9).

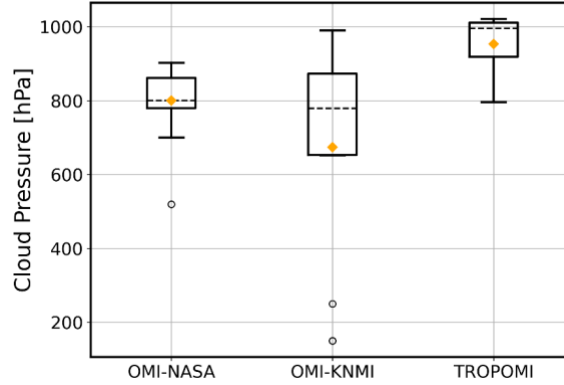


Figure 14. Box plots of OMI-NASA, OMI-KNMI, and TROPOMI v1.0.1 cloud pressures on cloudy days identified by TROPOMI.

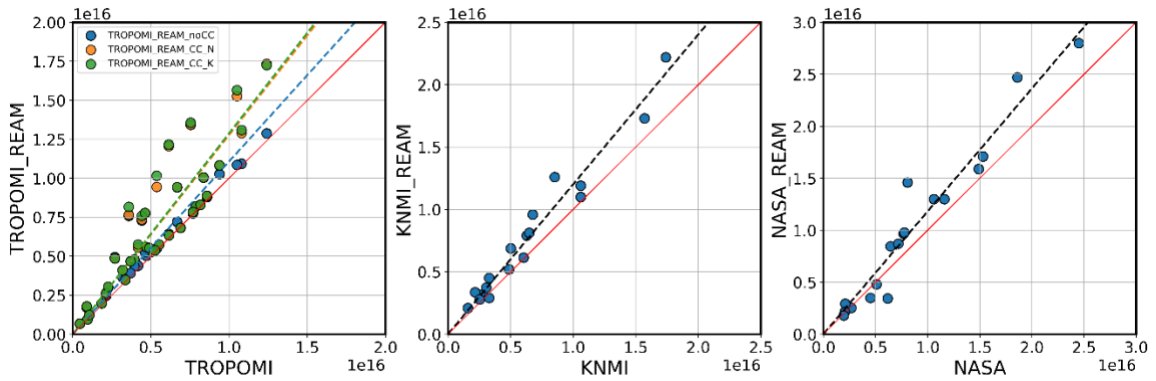


Figure 15. Standard satellite products compared with AMF_{REAM} retrieved TVCDs (molecules/cm³), the orange and green dots denote cloud corrected TROPOMI using OMI-NASA (TROPOMI_REAM_CC_N) and OMI-KNMI (TROPOMI_REAM_CC_K) cloud pressures accordingly. The red lines represent a 1:1 reference. The dashed lines denote the fitted lines on the corresponding scattered data. The root mean square error (RMSE) between TROPOMI_REAM_noCC and TROPOMI_REAM_CC_K is 1.8×10^{15} molecules/cm³, (relative change 29.7%) while that between TROPOMI_REAM_CC_K and TROPOMI_REAM_CC_N is 1.7×10^{14} molecules/cm³ (relative change 2.5%). The fitted slopes for TROPOMI_REAM_noCC, TROPOMI_REAM_CC_N, and TROPOMI_REAM_CC_K, against original TROPOMI products are 1.11, 1.28, and 1.29, respectively.

$$AMF = f_r AMF_{cld} + (1 - f_r) AMF_{clr} \quad (9)$$

During the measurement period, local agriculture burning occurred¹⁴. To identify these burning events around the observation site, we utilized the data from the Fire Information for Resource Management System (FIRMS) standard product²¹⁸. The FIRMS fire/hotspot data are derived from satellite sensors, including the Moderate Resolution Imaging Spectroradiometer (MODIS) onboard the Aqua and Terra satellites and the Visible Infrared Imaging Radiometer Suite (VIIRS) aboard S-NPP. By examining fire hot spots within 5 km of the observation site (Figure 16), we identified days affected by the burning events nearby. Since the emissions from these nearby fire events can potentially affect MAX-DOAS observations, we excluded the observations on 7 burning days from the intercomparisons between MAX-DOAS and satellite products. In section 3.3.3, we further examine the effects of burning on trace gas and aerosol concentrations specifically on the two largest burning days, Mar 25 and Apr 11, using MAX-DOAS observations.

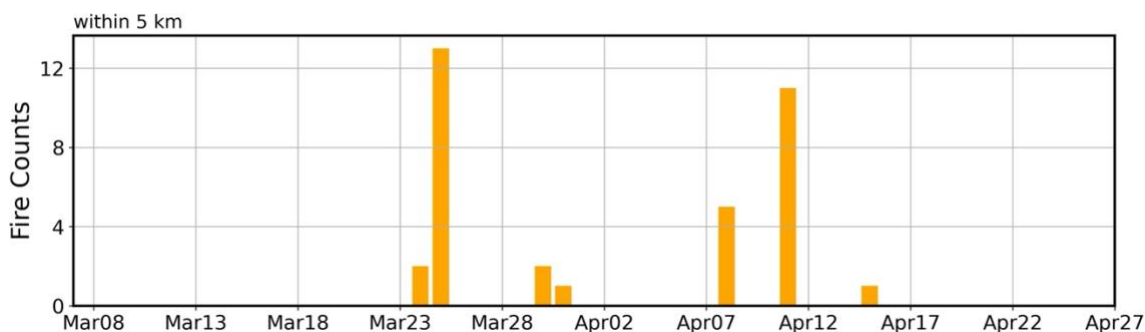


Figure 16. The daily evolution of FIRMS fire counts within 5 km from the observation site.

3.3 Results and Discussions

3.3.1 Overview of the Observations and Intercomparisons

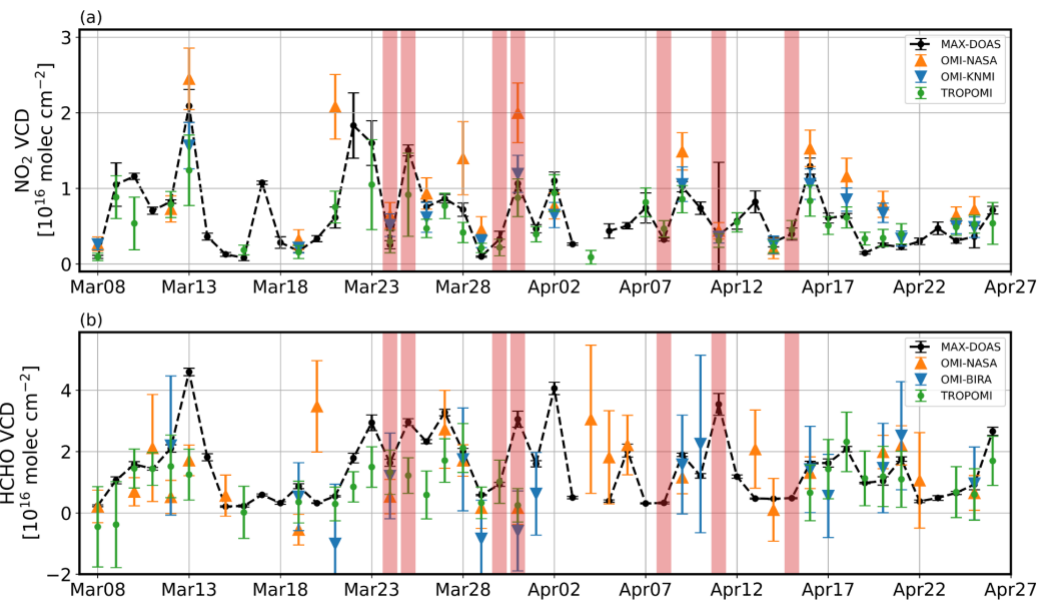


Figure 17. Daily variations and uncertainties (vertical error bars) of TVCDs from Mar 08, 2018, to Apr 26, 2018. (a) Time series of daily NO₂ TVCD data from MAX-DOAS (black), OMI-NASA (orange), OMI-KNMI (blue), and TROPOMI (green). (b) Time series of daily HCHO TVCD data from MAX-DOAS (black), OMI-NASA (orange), OMI-BIRA (blue), and TROPOMI (green). The red shadings indicate days affected by nearby burning activities.

Figure 17 illustrates the daily variations and uncertainties of NO₂ and HCHO TVCDs from MAX-DOAS and satellite products during the study period. Satellite data in the pixel over the site are compared to MAX-DOAS data at 13:00 - 14:00. The measured NO₂ TVCDs from MAX-DOAS ranged from 2×10^{15} to 1.8×10^{16} molecules/cm². In comparison to MAX-DOAS data, satellite observations captured the daily variations of NO₂ TVCDs well, except for a high bias in the OMI-NASA product. In contrast, larger discrepancies between MAX-DOAS and satellite data were found for HCHO, accompanied by larger uncertainties as well. Comparison statistics including correlation coefficients (r), p -values for linear correlation tests, slope for the through-the-origin least

squares regression, root mean square error (RMSE), mean bias error (MBE), and number of data pairs compared (N) are listed for each pair of comparison in Table 7 and Table 8.

Table 7. Intercomparison results for NO₂ TVCDs: correlation coefficient (r), p-value, slope for the through-the-origin least squares regression, root mean square error (RMSE), mean bias error (MBE), and number of data pairs (N) in each set of comparison between satellite and MAX-DOAS data.

Satellite Product	r	p	slope	RMSE [$\times 10^{16}$]	MBE [$\times 10^{16}$]	N
OMI-NASA	0.92	$\ll 0.05$	1.21	0.290	0.250	13
OMI-KNMI	0.92	$\ll 0.05$	0.838	0.223	0.002	13
TROPOMI	0.90	$\ll 0.05$	0.741	0.174	-0.105	28
NASA_REAM	0.91	$\ll 0.05$	1.41	0.354	0.408	13
KNMI_REAM	0.85	$\ll 0.05$	0.96	0.331	0.137	13
TROPOMI_REAM_noCC	0.88	$\ll 0.05$	0.77	0.194	-0.076	28
TROPOMI_REAM_CC	0.88	$\ll 0.05$	0.95	0.228	0.042	28

Table 8. Same as Table 7 but for HCHO TVCDs.

Satellite Product	r	p	slope	RMSE [$\times 10^{16}$]	MBE [$\times 10^{16}$]	N
OMI-NASA	0.290	0.216	0.718	1.104	0.023	20
OMI-BIRA	0.326	0.329	0.956	0.619	-0.014	11
TROPOMI L3	0.580	0.005	0.567	0.552	-0.609	22
NASA_REAM	0.489	0.029	0.995	1.197	0.420	20
BIRA_REAM	0.262	0.436	0.931	0.655	-0.045	11

The intercomparisons between MAX-DOAS and three satellite NO₂ TVCD products are presented in Figure 18. Each data point represents a pair of satellite-MAX-DOAS measurements, and through-the-origin least-squares regression lines are shown for all comparisons. While the satellite data captured the daily variations well, noticeable biases can be seen. Specifically, OMI-KNMI and TROPOMI exhibited low biases

compared to MAX-DOAS, whereas OMI-NASA showed a high bias (Figure 18(a)). These biases could be contributed by the differences in the a priori profiles used in the respective satellite products. We applied AMF_{REAM} computed from the same REAM a priori profiles to scale the original data products. For the two OMI products, the inclusion of AMF_{REAM} increased NO_2 TVCDs (Figure 15) due to a larger gradient of NO_2 concentrations from the lower boundary layer to the free troposphere simulated by the REAM model than the global model results used in the original satellite products, which was also reported in previous studies²⁰. However, in the case of TROPOMI retrievals, the largest corrections are related to cloud pressure corrections to this specific version of TROPOMI data used in our study, as mentioned in the previous section, which resulted in a 21% increase in TROPOMI NO_2 TVCDs (Figure 15) and brought TROPOMI data into close agreement with MAX-DOAS measurements. After these corrections, OMI-KNMI and TROPOMI TVCDs exhibited reasonably good agreement with MAX-DOAS, while OMI-NASA data showed a 30% higher bias (Figure 18(b)). We note that using the same a priori profiles did not completely eliminate the discrepancies between OMI-NASA and OMI-KNMI TVCDs. A further investigation into the differences between these two OMI NO_2 TVCD products will be discussed in section 3.2. Despite the biases, the correlation coefficients between satellite products and MAX-DOAS measurements for NO_2 TVCDs are all above 0.8 with significant p-values (<0.05), confirming the statistically significant agreements between satellite data and MAX-DOAS (Figure 19).

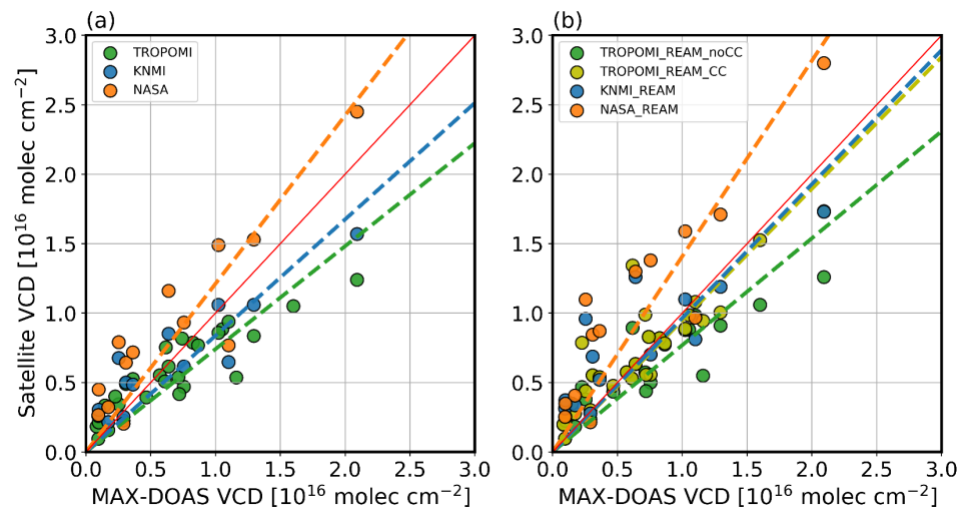


Figure 18. Intercomparison between NO₂ TVCDs from MAX-DOAS and those from satellites. (a) Before AMF adjustments, i.e., OMI-NASA (orange), OMI-KNMI (blue), and TROPOMI (green). (b) After AMF corrections using AMF_{REAM}, i.e., NASA_REAM (orange), KNMI_REAM (blue), and TROPOMI data with/without cloud correction (TROPOMI_REAM_CC/TROPOMI_REAM_noCC, olive/green). The dashed lines are least-squares regressions through the origin between satellite and MAX-DOAS data. A solid red line represents the 1:1 reference.

The discrepancies between MAX-DOAS and satellite HCHO products are much larger compared to the reasonable agreement observed among NO₂ products. MAX-DOAS HCHO ranged from 2.3×10^{15} to 4.6×10^{16} molecules/cm². Correlations between standard satellite products and MAX-DOAS data are statistically insignificant ($p > 0.05$) (Figure 20), except for TROPOMI data, which exhibited a higher correlation coefficient (~ 0.6) and a significant correlation with MAX-DOAS data (p -value = 0.005). To address the impact of different a priori profiles, we corrected the satellite data with AMF_{REAM} calculated from REAM simulated a priori profiles. The correction significantly improved the correlation of OMI-NASA data with MAX-DOAS ($p < 0.05$) (Figure 20). However, the AMF_{REAM} effect on OMI-BIRA data is negligible in the correlation comparison due to much better

agreement of the OMI-BIRA AMF data with AMF_{REAM} than OMI-NASA AMF data (Figure 21). In the case of TROPOMI, since only L3 data is available, AMF adjustments could not be applied. To further quantify the comparisons, we analyzed the standard deviations of NASA_REAM, BIRA_REAM, and TROPOMI data. Binning the satellite data based on MAX-DOAS measurements, with each bin representing 10^{16} molecules/cm², we calculated the standard deviations of satellite and MAX-DOAS data when > 2 data points are available. There are generally 6-9 data points in each bin, except for the comparison between OMI-NASA and MAX-DOAS, where the $[2 - 3] \times 10^{16}$ molecules/cm² bin only has 3 data points, resulting in a large standard deviation for that bin. Results showed that the standard deviations of OMI data are consistently larger than those of MAX-DOAS, whereas the standard deviations of TROPOMI are comparable to MAX-DOAS (Figure 22 (b)), indicating better quality of TROPOMI HCHO data. Comparing the standard deviations of satellite data with those of MAX-DOAS data, for low-, mid-, and high-HCHO bins, the Sd ratios, are > 3 for OMI data and ~ 1 for TROPOMI data, indicating much improved correlation of TROPOMI data with MAX-DOAS data than that of OMI data. The examination of RMSE for the whole data set (Table 8) with roughly same sample sizes reveals that the RMSE for the OMI-NASA product is approximately twice that of the TROPOMI product.

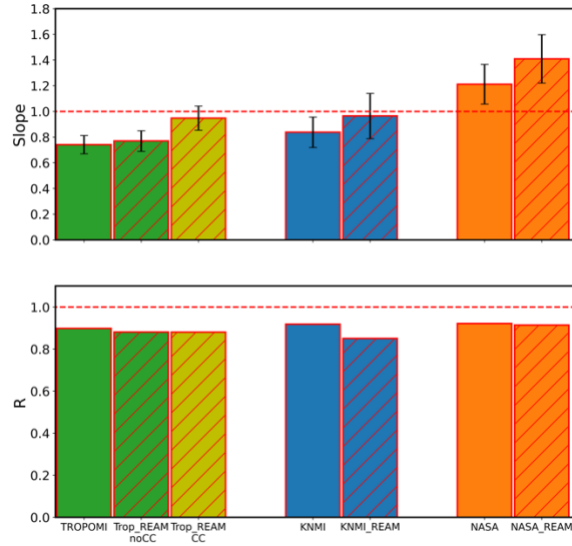


Figure 19. Slopes with error bars (top panel) and correlation coefficients (R, bottom panel) for NO₂ TVCDs observed between satellites and MAX-DOAS, from left to right, are TROPOMI, TROPOMI_REAM without cloud correction, TROPOMI_REAM with cloud correction, KNMI, KNMI_REAM, NASA, NASA_REAM. The boxes with slash lines denote AMF_{REAM} corrected satellite data. The boxes with red borders represent data with a p-value < 0.05, indicating statistical significance.

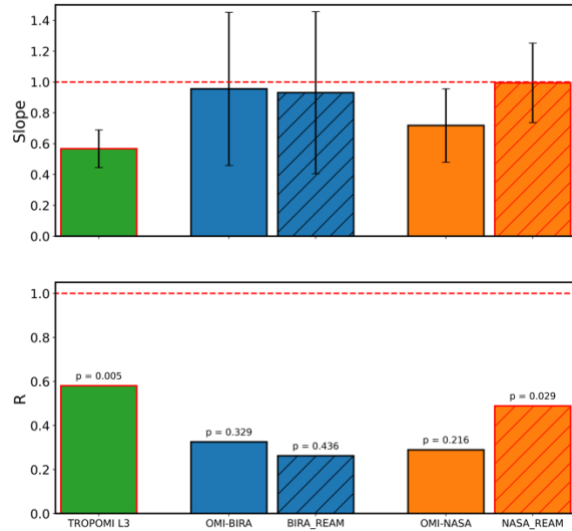


Figure 20. Slopes with error bars (top panel) and correlation coefficients (R, bottom panel) for HCHO TVCDs observed between satellites and MAX-DOAS, from left to right, are TROPOMI, OMI-BIRA, BIRA_REAM, NASA, and NASA_REAM. The boxes with slash lines denote AMF_{REAM} corrected satellite data. The boxes with red borders represent data with a p-value < 0.05, indicating statistical significance.

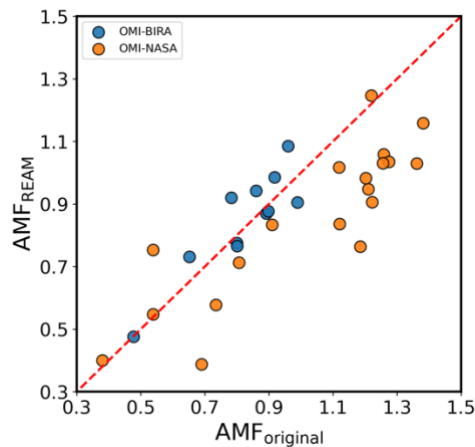


Figure 21. Original AMFs vs REAM-scaled AMFs for two OMI HCHO products. The red dashed line represents a 1:1 reference.

Previous studies have also shown that intercomparisons of HCHO products generally exhibit larger scatters and weaker correlations compared to NO₂, especially in

the case of OMI HCHO products (e.g., this study²⁰). This can be attributed to stronger Rayleigh scattering at shorter wavelengths (~340nm for HCHO) than at longer wavelengths (~440nm for NO₂), resulting in lower sensitivity of measurements to HCHO in the lower atmosphere than to NO₂¹⁹⁹. Although only pre-release TROPOMI HCHO data were available during the OPECE period, the analysis showed promising improvements in the signal-to-noise ratios of TROPOMI HCHO product compared to OMI¹⁶⁶. Furthermore, it should be noted that some scatter in the comparisons of satellite data with MAX-DOAS data can be caused by uncertainties related to spatial representativeness or mismatch and random uncertainties of satellite products, which are challenging to quantify from pairwise comparisons²¹⁹. Estimating the random uncertainties may require a triple co-location method²²⁰, but this approach requires a larger dataset than available in this study (e.g., sample size N>100)²²¹⁻²²³. Nonetheless, the comparison of satellite HCHO TVCDs to NO₂ data based on MAX-DOAS observations is informative in demonstrating the larger uncertainties associated with satellite HCHO retrievals compared to NO₂.

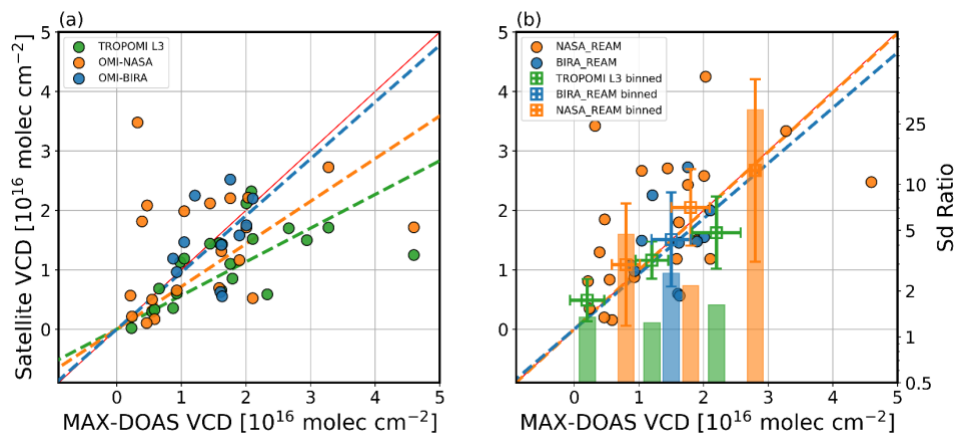


Figure 22. Intercomparison of HCHO TVCDs from MAX-DOAS with those from satellites. (a) OMI-NASA, OMI-BIRA, and TROPOMI data before AMF

adjustment. (b) OMI-NASA and OMI-BIRA data after AMF adjustment. The boxes with error bars show the average and standard deviations for the corresponding variables in each bin of MAX-DOAS data. The vertical bars with standard deviations show the Sd ratio, the standard deviation ratios of satellite to MAX-DOAS data in each bin, in which more than 2 data points are available. The dashed lines are fitted on the corresponding scatter plots (in (a)) through the origin, with a solid red line representing the 1:1 reference.

During this study period, we investigated the weekly variations in MAX-DOAS and satellite TVCDs of NO₂ and HCHO to gain insights into potential source contributions of pollutants. Previous studies have suggested lower NO₂ TVCDs on weekends than on weekdays in urban regions ^{194, 207, 224-226}. However, the average weekly variation of NO₂ and HCHO datasets did not exhibit statistically significant variations based on the Kruskal-Wallis test. The lack of significant weekly variations can be attributed to the influence of changes in transport to the observation site, which can weaken the expected weekly cycle associated with urban emissions ^{225, 227-229}. Furthermore, MAX-DOAS observations of SO₂ (Figure 30) indicated that the rural observation site was strongly affected by the transport of polluted and clean air masses.

3.3.2 Resolving the Difference Between NASA and KNMI NO₂ TVCDs

We further investigated the systematically higher biases observed in OMI-NASA NO₂ TVCDs than in OMI-KNMI data. Examination of SCDs showed negligible discrepancies between these two products, consistent with previous studies ^{206, 230}. Therefore, our focus shifted to the difference in AMFs, which is known to be a major source of uncertainty in the OMI NO₂ retrievals ¹⁹³. A comparison of AMFs for the two OMI products before and after applying the REAM a priori profiles showed that using the same

a priori profiles results in slightly better AMF agreement between NASA and KNMI data, but the substantial low bias in the NASA AMFs persisted (Figure 23). This result suggested that the difference in AMFs between the two OMI products is not primarily influenced by the difference in NO₂ a priori profiles but rather by the scattering weights, which are independent of the vertical distribution for optically thin absorbers like NO₂^{231, 232}.

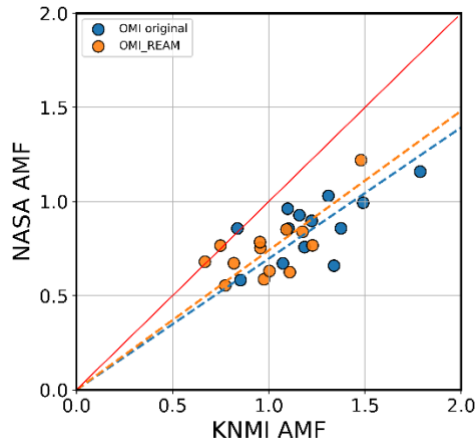


Figure 23. Scatter plots of original AMF (blue) and REAM profile scaled AMF_{REAM} (orange) from OMI-NASA versus OMI-KNMI. The dashed lines are least-squares regressions through the origin, and a solid red line represents the 1:1 reference.

Further inspection of scattering weights revealed a low bias of scattering weights of OMI-NASA compared to those of OMI-KNMI in the lower troposphere, specifically around 800 hPa (Figure 24). The scattering weights are determined through a look-up table based on factors including optical geometry, surface reflectivity, cloud pressure, and cloud fraction^{188, 190}.

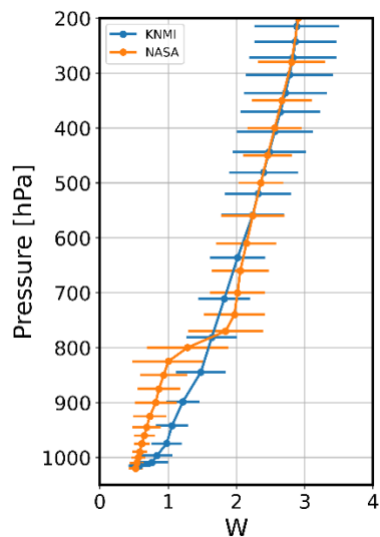


Figure 24. The median vertical profiles with standard deviations (horizontal error bars) of scattering weights (w) of OMI-NASA (orange) and OMI-KNMI (blue) products from Mar 08 to Apr 26, 2018.

Cloud properties were compared between KNMI and NASA retrievals during the study period (Figure 25), revealing retrieved average cloud pressures of 645 ± 260 hPa for KNMI and 820 ± 115 hPa for NASA. In addition, the mean cloud radiance fraction from NASA is approximately 0.3, which is around twice as large as that of KNMI at around 0.15. This discrepancy in cloud properties between the two OMI products extends beyond the observation site, as shown by a comparison of mean distributions for the NCP region around the OPECE site (Figure 26). Surface reflectivity also affects AMF calculation by being one parameter used in the look-up table for scattering weights and indirectly through its impact on cloud retrievals^{233, 234}. The v4.0 of the NASA product incorporated the geometry-dependent surface Lambertian equivalent reflectivity (GLER) product to account for the bidirectional reflectance distribution function (BRDF) effect. The daily GLER product is derived from MODIS observations and applied to both NO₂ and cloud retrievals

in the NASA product, replacing the climatological OMI-based datasets used in previous versions ^{210, 235-237}. Studies have indicated that the inclusion of this new GLER product could lead to lower AMF by 29% to 50% due to a combination of the BRDF effect and biases between MODIS and OMI-based datasets ^{210, 238}. It remains unclear whether updating GLER in NASA retrievals is responsible for the observed differences in the scattering weight profiles in this study. Further inspections comparing the retrieval algorithms of two OMI products are needed. Additionally, since the observation site is coastal (Figure 13), lower-level clouds in the ocean boundary layer may also contribute to the uncertainties in AMF calculations ¹⁵⁸. Furthermore, both OMI-KNMI and OMI-NASA products accounted for scattering effects of aerosols in AMF calculations ^{185, 210}. The aerosol optical depth (AOD) measured by MAX-DOAS during our study period is 1 ± 0.48 . Absorbing aerosols might introduce further uncertainties ²³⁹.

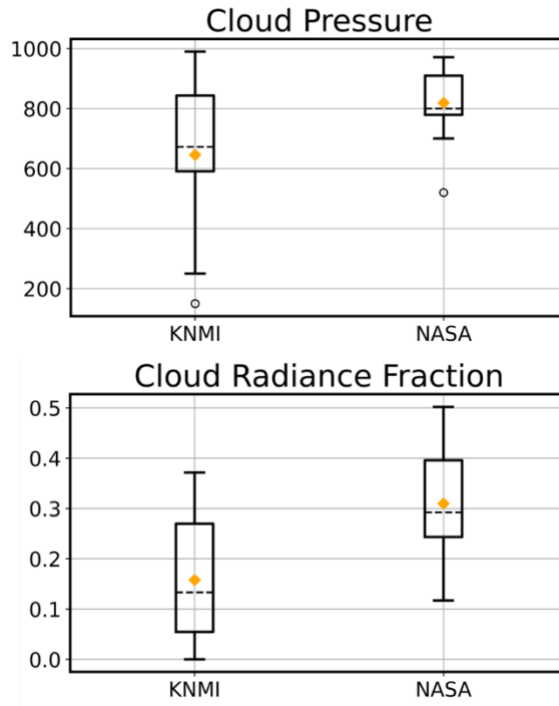


Figure 25. The box plots for cloud pressure (hPa, upper row) and cloud radiance fraction (unitless, lower row) of OMI-KNMI and OMI-NASA.

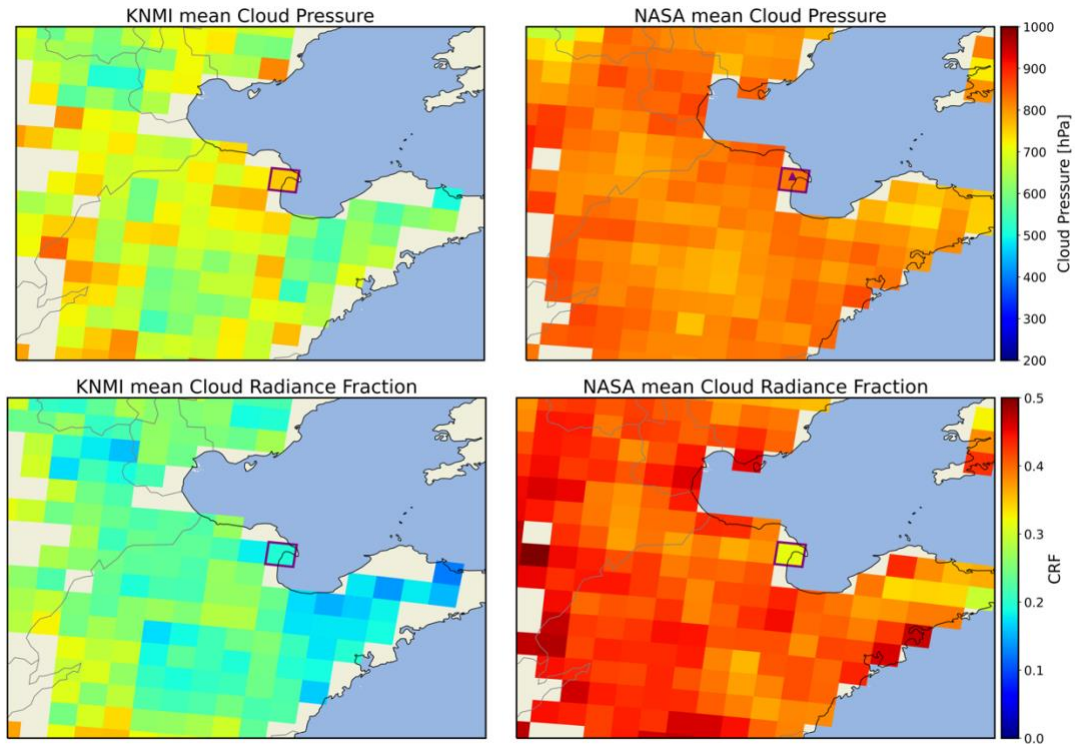


Figure 26. Mean cloud pressure (upper row) and mean cloud radiance fraction (lower row) from OMI-KNMI (left column) and OMI-NASA (right column) NO₂ products. The purple box denotes the grid that contains the observation site (denoted by the purple triangle in the upper right panel).

3.3.3 Biomass Burning Impacts on HONO, NO₂, and HCHO

During the measurement period, we identified 7 BB days using FIRMS fire hot spot data (Figure 16). During these 7 days, the OMI products had around 2 valid measurements and TROPOMI had 3 valid measurements. Since agriculture burning is often localized, its impact can be much larger on the ground-based MAX-DOAS measurements than on OMI data. TROPOMI data has a finer horizontal resolution than OMI data³⁵, but is not publicly available during our study period, when TROPOMI was still in the commissioning phase.

Additionally, the MAX-DOAS instrument provides vertical profile information. Therefore, only the MAX-DOAS measurements are utilized in the analysis of BB impacts.

On the BB days, westerly winds at ~ 3 m/s dominated the site, except for Mar 25, Apr 8, and Apr 11. The MAX-DOAS observations of SO₂, HONO, HCHO, NO₂, and AEC for all the BB days (Figure 27) indicated significant variations in air quality conditions. The daytime mixing ratios of SO₂ ranged from 0.4 ppbv to 9.2 ppbv. The enhancements of NO₂ and HCHO tend to co-occur more frequently than either one to co-occur with high HONO concentrations. On the other hand, AEC concentrations can be enhanced even when NO₂ and HCHO concentrations are not elevated, reflecting likely aerosol production during the smoldering stage of burning and subsequent transport processes.

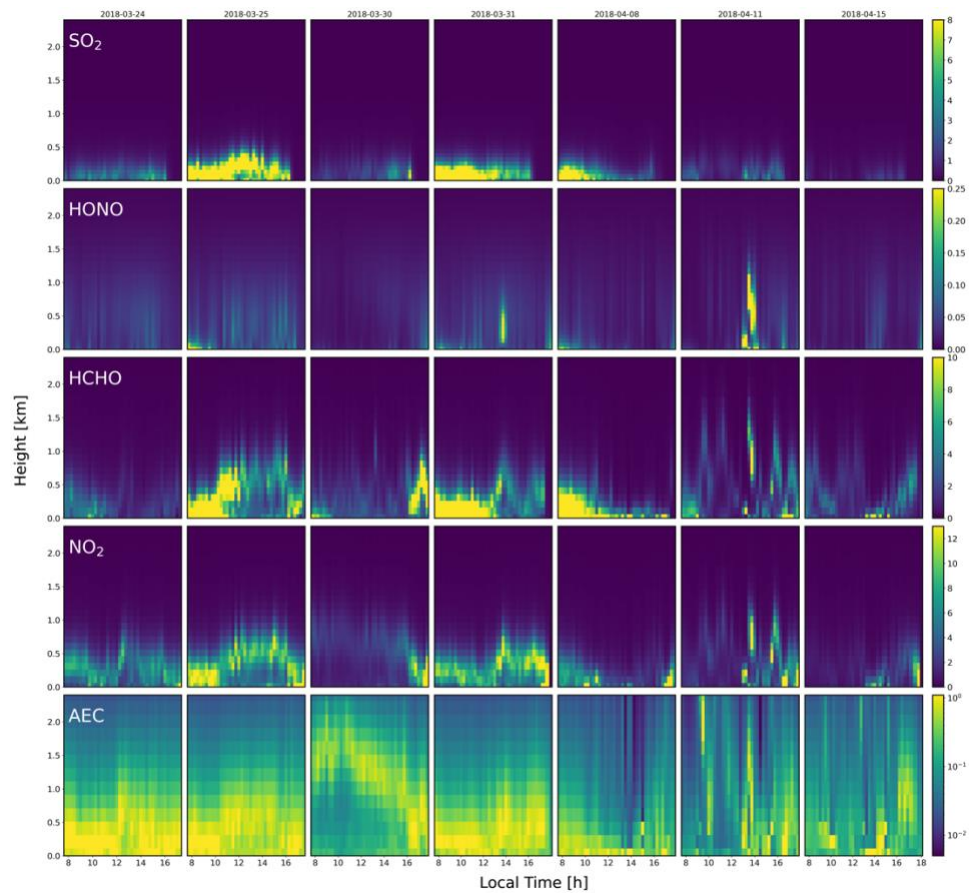


Figure 27. MAX-DOAS observations for SO₂, HONO, HCHO, NO₂, and AEC during the 7 BB days identified by FIRMS fire data.

The observations of SO₂ indicated that BB events occurred on both polluted and clean days. In order to accurately quantify BB enhancements, it is important to account for the background concentrations. To achieve this, we utilized the observed SO₂ concentrations to distinguish between clean and polluted days. Specifically, days with noontime near-surface SO₂ lower than 1 ppbv were identified as clean days while others were classified as polluted. During the measurement period, we identified 12 clean days and 38 polluted days based on this criterion.

For BB effect analysis, we divided the observations into two groups based on the pollution conditions and selected two BB days with the highest fire counts under clean (Apr 11) and polluted (Mar 25) conditions, respectively. Other than the highest fire counts, these two days were also characterized by elevated HCHO and NO₂ in the upper boundary layer compared to other BB days, indicating more pronounced BB impacts (Figure 27). On Mar 25, significant burning activities occurred 5 km to the west of the site. Wind at 3 m/s came from the northwest. On Apr 11, wind was weak at 0.7 m/s, and the burnings occurred right next to the site (Figure 28).



Figure 28. FIRMS observed fire hotspots (red squares) around the observation site (denoted as a yellow marker on the map) on Mar 25th (top panel) and Apr 11th (bottom panel).

Figure 29 illustrates the daytime profiles of trace gas species and AEC for both BB events and their corresponding average background conditions. On average, polluted days exhibited much higher boundary-layer concentrations than clean days for all species, except for HONO.

On Apr 11, observed SO₂ concentrations surpassed the average levels of non-BB days, indicating that BB could also contribute to the observed high concentrations. Notably, observations of HCHO revealed three distinct burning plumes reaching above 0.5 km between 1 pm and 6 pm LT, accompanied by corresponding enhancements in NO₂, peaking above 0.5 km around 2 pm LT. The observations of HONO displayed significant

enhancements up to 1.2 km from 1 pm to 3 pm LT, marking the largest HONO pollution event throughout the campaign. Additionally, observations of AEC on Apr 11 also showed elevated levels up to 1.5 km between 1 pm to 3 pm LT, with high AEC concentrations limited to the lower boundary layer in the late afternoon. These observations are consistent with photolytically enhanced production of HONO on aerosols, as discussed in previous studies^{21, 117}.

On Mar 25, higher SO₂ concentrations were also observed in the lower boundary layer compared to the average non-BB polluted days. HCHO observations showed elevated concentrations at 0.5-1 km throughout the day, while NO₂ observations exhibited elevated levels, with larger enhancements in the late morning than in the afternoon. It is noteworthy that the average vertical gradient of NO₂ is larger than that of HCHO on polluted non-BB days, reflecting the secondary production of HCHO²⁴⁰. However, the enhancements of HONO and AEC on Mar 25 were not as significant as those of HCHO and NO₂ compared to the average non-BB days.

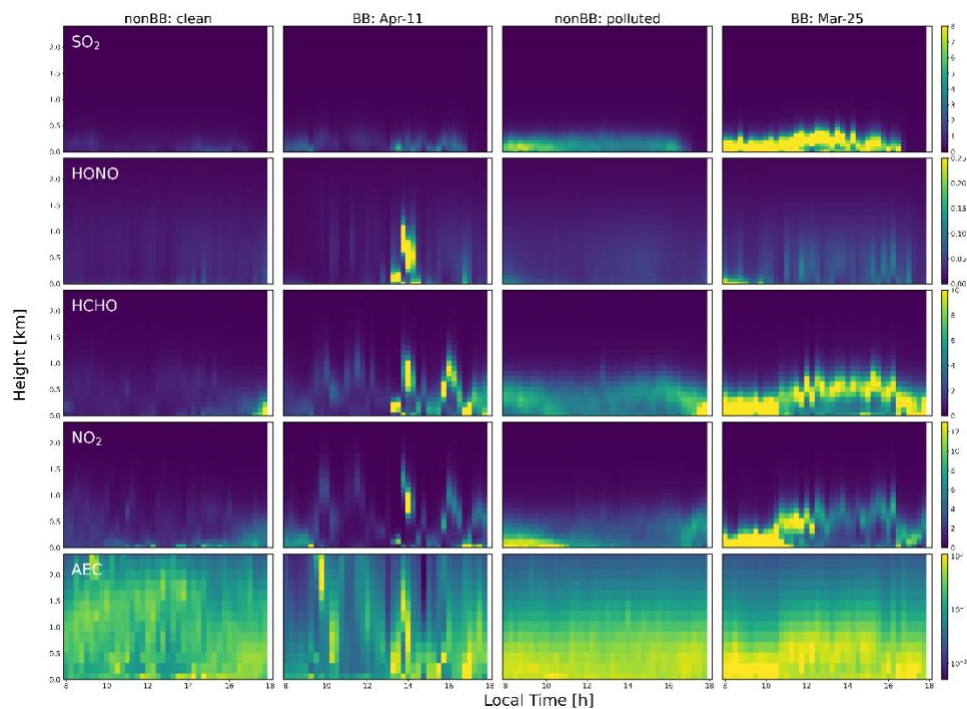


Figure 29. MAX-DOAS observed daytime evolutions of SO₂, HONO, HCHO, NO₂, and AEC mixing ratios for (a) non-burning days under clean conditions, (b) on Apr 11, 2018, during the burning events under clean conditions, (c) non-burning days under polluted conditions, and (d) on Mar 25, 2018, during the burning events under polluted conditions.

During the flaming stage, HONO can be co-emitted with NO_x³⁶, whereas during the smoldering stage, the secondary production of HONO becomes more important⁷⁴. Heterogeneous HONO production mechanisms have been extensively studied in recent years due to their potentially significant impact on O₃ production, such as photo-enhanced NO₂ conversion on aerosols²¹ and the photolysis of particulate nitrate¹¹⁷. Among HONO, NO₂, and HCHO, HONO has the shortest photochemical lifetime. Therefore, the moderate but more persistent enhancements of HONO than those of NO₂ and HCHO throughout the boundary layer on Mar 25 (Figure 29) likely reflects heterogeneous HONO production that sustained the elevated level of HONO.

To quantify the enhancements due to BB at both the surface and upper layers, we determined the height of the surface mixed layer by the location of the largest SO₂ vertical gradient on polluted days. For clean days, the average hourly height of the surface mixed layer height was used. The derived surface layer heights during the OPECE experiment ranged from 300m to 500m (Figure 30). To assess the BB enhancements, we integrated MAX-DOAS observations within the lower columns of the surface mixed layer and the upper columns from the top of the surface layer to 3.5 km. Subsequently, we calculated the column enhancement ratios, denoted as X , of lower and upper columns on the selected burning days to the corresponding averages on non-BB days, i.e., Apr 11 data relative to non-BB clean days' average and Mar 25 to the non-BB polluted days' average. Figure 31 (a)-(b) shows the ratios of NO₂, HONO, HCHO, AEC, and SO₂ column enhancements. The column enhancement ratios for SO₂, X_{SO_2} , are large in both the upper and lower columns on Apr 11 and in the lower column on Mar 25. The polluted NCP region is characterized by high anthropogenic SO₂ emissions^{241, 242}. Additionally, agricultural burnings also contribute to SO₂ emissions. The emission factor ratio of SO₂ to NO₂ for agricultural fires is estimated to be 0.4²⁴³. However, as shown in Figure 29, the observed SO₂ concentrations do not correlate with NO₂, which is produced during BB, on burning days. Figure 31 further demonstrates that the X_{SO_2} is much larger than X_{NO_2} in the surface mixed layer on two BB days, indicating that relative enhancement ratios of SO₂ to NO₂ are much larger than the emission factor for agricultural burnings reported by Liu et al. (2016). Consequently, the observational evidence suggests that BB emissions of SO₂ are negligible compared to other anthropogenic SO₂ sources at the observation site.

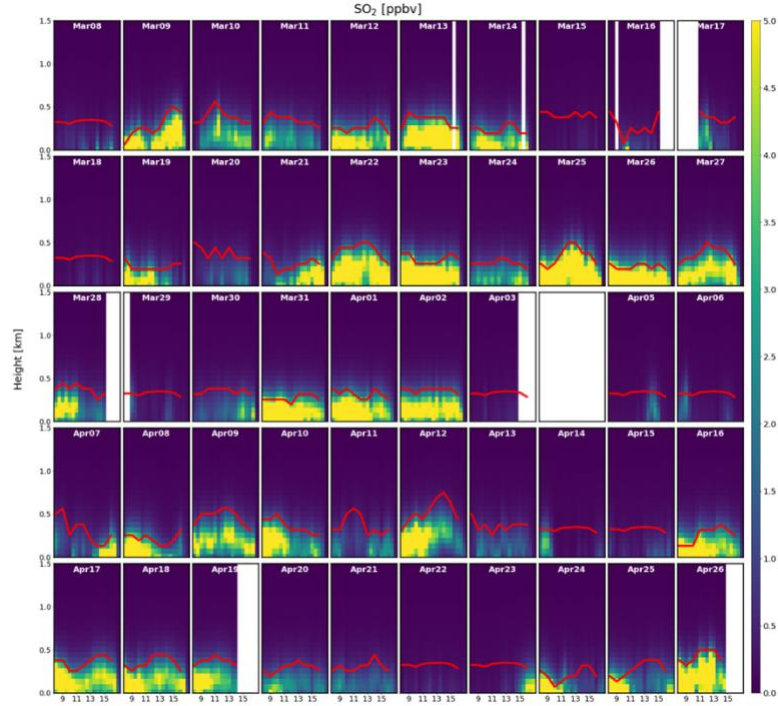


Figure 30. Surface mixed layer height (solid red lines) calculated by MAX-DOAS vertical profiles of SO₂ from Mar 8th to Apr 26th, 2018.

Since SO₂ is not affected by BB emissions, we calculated BB enhancements relative to that of SO₂ given the nearly linear relationships of the non-BB enhancements of other species with that of SO₂. This can be expressed as the relative BB enhancement ratio:

$$\frac{X^i/X_{bg}^i}{X^{SO_2}/X_{bg}^{SO_2}},$$

where X^i denotes the density of species i , and X_{bg}^i denotes the average density

of species i on the corresponding non-BB days. Figure 31 (c)-(d) show the relative BB enhancement ratios for Apr 11 and Mar 25. In the surface layer, the relative BB enhancement ratios of all species are either slightly greater than 1 or less than 1. However, in the upper layer, the enhancements of HONO, NO₂, and HCHO are larger compared to the surface layer, indicating stronger vertical transport due to the higher potential temperature of fresh BB air masses during the flaming stage, caused by fire heating.

Another supporting piece of evidence for fires in the flaming stage is that the relative enhancement ratios of AEC in the upper layer are small, in contrast to the large enhancement of PMs accompanying the smoldering combustion^{244, 245}. On these two days with the highest fire counts during the OPECE experiment, the fire enhancement of HCHO in the upper layer is consistently large, while HONO and NO₂ enhancement ratios are comparably large only on one of the days. The four panels of Figure 31 together reveal that HCHO and NO₂ enhancements in the upper layer tend to occur together but the enhancement magnitudes have large variations. In comparison, the patterns of HONO enhancements differ from those of HCHO and NO₂.

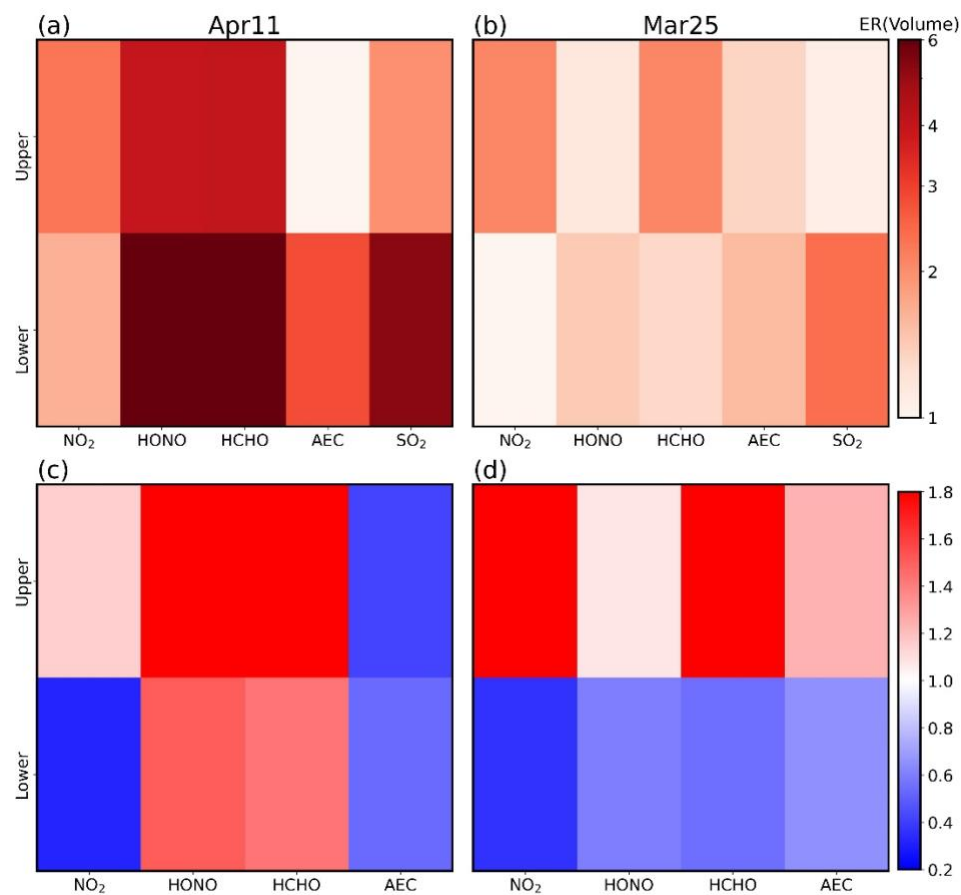


Figure 31. (a) Enhancement ratios of BB to non-BB days of NO₂, HONO, HCHO, AEC, and SO₂ in the upper and lower columns for Apr 11. (b) Same as (a) but for Mar 25. (c) BB enhancement ratios relative to SO₂ enhancement in the upper and lower columns for NO₂, HONO, HCHO, and AEC for Apr 11. (d) Same as (c) but for Mar 25. See text for details.

3.4 Conclusions

Satellite NO₂ and HCHO products provide valuable insights into pollution distributions and global photochemistry. However, to ensure their accurate applications, the validation of satellite products is essential. Ground-based observations conducted at rural sites with minimal local emissions are particularly useful for this purpose. In this study, we utilized MAX-DOAS observations collected at a rural coastal site in Dongying,

China, during the OPECE experiment. The MAX-DOAS observations of NO₂ and HCHO on days without local burnings are intercompared with NASA and KNMI OMI and TROPOMI operational NO₂ TVCD products, NASA and BIRA OMI HCHO products, and TROPOMI L3 HCHO products. Additionally, we analyzed the effects of BB on boundary layer HONO, NO₂, and HCHO using MAX-DOAS observations on days with local burnings.

After employing consistent a priori profiles from the regional REAM model in OMI and MAX-DOAS retrievals and correcting the cloud pressure bias in TROPOMI v1.0 retrievals, we found a generally better agreement of satellite with MAX-DOAS data for NO₂ products than for HCHO products. When comparing with MAX-DOAS data, the correlation coefficients for all satellite NO₂ products exceeded 0.8. While OMI-KNMI and TROPOMI data exhibit no significant biases, OMI-NASA data showed a ~30% positive bias. Further analysis indicated that this bias is due to a lower estimation of scattering weight profiles in the lower troposphere in the OMI-NASA NO₂ product than in the OMI-KNMI data. The reasons for this discrepancy could be attributed in part to the more extensive cloud presence above the boundary layer around the observation site in the OMI-NASA than OMI-KNMI products. On the other hand, the agreement between satellite and MAX-DOAS HCHO data was relatively low, with correlation coefficients below 0.6. The TROPOMI HCHO data exhibited the highest correlation coefficient and significantly lower data scattering relative to MAX-DOAS data compared to OMI data. This intercomparison suggests that the TROPOMI HCHO product shows good promise for improvement compared to OMI.

MAX-DOAS observed vertical profiles of SO₂ show that the observation site was affected by the transport of polluted and clean air masses. We used these data to categorize the observations into clean and polluted days and to estimate the heights of the surface mixed layer. Analysis of MAX-DOAS observations on the two largest burning days (Mar 25 and Apr 11) revealed more pronounced enhancements due to fire emissions in the upper boundary layer than the surface mixed layer, reflecting the higher potential temperature of fresh burning air masses due to fire heating during the flaming stage. The evident upper boundary fire enhancements and comparatively lower enhancements of AEC than NO₂ and HCHO are consistent with the prevalent influence of flaming combustions in MAX-DOAS measurements, which are limited to daytime only. Concentrations of HONO, NO₂, and HCHO can be substantially enhanced by burning, with NO₂ and HCHO enhancements often occurring together but exhibiting considerable variations in magnitude. On the other hand, the fire enhancements of HONO exhibit noticeable differences compared to those of HCHO and NO₂, and they also demonstrate a higher level of variability.

CHAPTER 4. SEASONAL AND HISTORICAL TRENDS OF SECONDARY ORGANIC CARBON ACROSS THE CONTINENTAL UNITED STATES

4.1 Introduction

Carbonaceous aerosols, consist of particulate organic carbon (OC) and elemental carbon (EC), have significant effects on global climate, ecological system, and human health²⁴⁶⁻²⁴⁸. EC is directly emitted from combustion sources, whereas OC includes primary OC (POC) from direct emissions of particles and secondary OC (SOC) produced from the oxidation of volatile organic compounds (VOCs). Both biogenic and anthropogenic VOCs can lead to the formation of SOC^{11, 249-252}, which involves complex sources and processes, making it difficult to characterize SOC. For example, biomass burning (BB), which can lead to emissions of POC, as well as formations of SOC by the emissions of VOC precursors^{253, 254}. A better understanding of the factors controlling SOC is thus essential to develop appropriate regulations that can efficiently control the PM_{2.5} pollution.

Over the past decades, substantial effort has been put into quantifying concentrations and sources of SOC²⁵⁵⁻²⁵⁷. Several methods were developed for deriving SOC concentrations using filter-based measurements. When the SOC fractional contributions from VOC precursors are obtained from smog chamber experiments, SOC concentrations can be estimated from ambient VOC measurements^{258, 259}. The complexity of SOC

precursors and oxidation processes, however, limit the applicability of this method. More generally, SOC estimates are based on tracer correlations. The widely used EC tracer method²⁶⁰ assumes that POC and EC sources are co-located and their concentrations are correlated. Through regression analysis of OC and EC under POC-dominant conditions, the POC/EC ratios are estimated first, and SOC is then computed as the difference between OC and POC. However, the variability of the POC/EC ratio over time and region poses a challenge when using this method²⁶¹. Moreover, multivariate receptor models, such as the chemical mass balance (CMB)²⁶² and positive matrix factorization (PMF)²⁶³, have been developed. The CMB model utilizes a priori source profiles for POC tracers and compute POC concentrations based on least square solutions of OC measurements with the POC source profiles and source contributions. However, variations in POC-tracer profiles for the same type of sources across different regions and seasons, as well as the influence of atmospheric oxidation and mixing processes on ambient POC tracer concentrations, pose limitations to the model's accuracy. The PMF method is more flexible than CMB in that the source profiles are estimated based on the measurements and that both POC and SOC tracers can be used in the analysis. Compared to CMB, the PMF method requires much larger datasets and the results are not necessarily unique²⁶⁴.

Compared to filter-based measurements, the aerosol mass spectrometer (AMS) and aerosol chemical speciation monitor (ACSM) instruments offer significantly higher temporal resolutions and provide detailed composition data with enhanced resolution²⁶⁵⁻²⁶⁷. Typically, the AMS datasets are processed using the PMF method to estimate SOC concentrations. Due to particle loss on sampling inlet surfaces for PM_{2.5} and reduced

transmission efficiency, the original AMS and ACSM instruments were used to measure the composition of submicron particulate matters. Recent development of a new PM_{2.5} aerodynamic lens and a capture vaporizer (CV) improved the collection efficiency of super-micron particles²⁶⁸⁻²⁷⁰. The new CV and PM_{2.5} inlet have been equipped with AMS or ACSM in source apportionment studies in both US and China to be compared with those from the original AMS or ACSM measurements with standard vaporizer (SV) and discrepancies in some organic aerosol (OA) were found²⁷¹⁻²⁷³. For example, studies found generally values in f₄₄ (mass fraction of m/z44 in OA) reported by the new instrument^{271, 274}. Such discrepancies could be attributed to the changed OA mass spectra caused by additional thermal decomposition in the new CV^{275, 276}, a lower transmission efficiency of the new PM_{2.5} lens for particles with sizes less than 300 nm²⁷⁷, or changed relative ionization efficiencies (RIE) leading to changed response factors (RIE x CE)^{278, 279}. Efforts are ongoing to resolve these discrepancies²⁷³.

While AMS/ACSM measurements hold promises for providing high-resolution SOC data and efforts such as the Atmospheric Science and Chemistry mEasurement NeTwork (ASCENT) are underway, processing historical data on large spatial scales are still essential to understand SOC changes²⁸⁰⁻²⁸⁴. Furthermore, establishing connections between historical datasets and future long-term AMS/ACSM measurements is crucial. In this work, we introduce a novel statistical method to estimate empirical SOC (EMSOC) concentrations for six regions across the continental US (CONUS) using historical OC and EC data spanning 15 years (2005-2020) from the Interagency Monitoring of Protected Visual Environments (IMPROVE) network. Our analysis focuses on investigating the

long-term trends and interannual variability in SOC over CONUS, and the corresponding controlling factors for summertime SOC production in different regions through a stepwise multiple linear regression (SMLR).

4.2 Material and Methods

4.2.1 Observational Dataset

Daily observations of aerosol speciation data, including OC, EC, sulfate, and nitrate, during 2005-2020, are obtained from the IMPROVE network. The IMPROVE network has continuous records of PM_{2.5} measurements since 1987, and underwent a temperature protocol change deployed in 2005²⁸⁵. To minimize the impact on long-term consistency due to this protocol change, we start our analysis from 2005. For the SMLR analysis, we utilized several ancillary datasets to represent different factors. To represent the biogenic emissions at each region, we use monthly HCHO tropospheric vertical column density (TVCD) data from the Ozone Monitoring Instrument (OMI). The OMI QA4ECV L3 HCHO products¹⁹⁵ was developed by the European consortium (BIRA, IUP, MPIC, KNMI, WUR) in the framework of the EU-FP7 QA4ECV project. OMI HCHO product provides daily HCHO TVCD data with a local overpass time of 13:30. For each IMPROVE site, we extract HCHO data from the pixel that covers the IMPROVE site for further analysis. Ground-based isoprene (ISOP) measurements from the US Environmental Protection Agency's Air Quality System is also available, but due to their low temporal and spatial coverage throughout our study period, they were discarded from the SMLR analysis. The factors for wildfires are represented by estimated fire carbon emission data

from the fourth version of the Global Fire Emissions Database (GFED)²⁸⁶. Daily 0.25°×0.25° resolution carbon emission data is derived by multiplying the satellite-based burned area and fuel consumption per unit area through a biogeochemical model. Similarly, we selected co-located fire emission data by identifying the GFED grid that covers the IMPROVE site. As for the radiation data, we utilize monthly surface downward solar radiation (ssrd) from the ERA5 reanalysis database²⁸⁷ by the European Centre for Medium-range Weather Forecasts (ECMWF). The reanalysis from ECMWF combines model data with historical satellite and in-situ measurements into a globally complete and consistent data set. To ensure data quality, we utilized Tukey's Fences²⁸⁸ to exclude the outliers for all the time series data. Gridded data (GFED, ERA5, OMI HCHO) are selected to match the corresponding IMPROVE site. Since we derived seasonal secondary fractions, the temporal resolutions are all unified as seasonal data for the SMLR analysis.

4.2.2 ACCA Clustering Method

For a precise assessment of the controlling factors affecting SOC in each region, it is imperative to employ a clustering solution capable of effectively grouping sites governed by similar influential factors in SOC production. Correlation clustering stands out as an effective approach, as it yields results showcasing a more consistent pattern of variation²⁸⁹. Notably, the application of the average correlation clustering algorithm (ACCA)²⁹⁰, widely utilized in the bioinformatic domain, has demonstrated superior capabilities in generating outcomes that are notably more relevant to biological annotations compared to alternative methods. Since no direct measurement of SOC is available, we adopt ACCA method to group 160 IMPROVE sites into six geographical clusters based on the

correlations of OC concentrations among the surface sites. ACCA clustering runs are done with predetermined cluster numbers ranging from 3 to 10. We chose the results according to the criteria that: (1) all sites of a cluster are in one geographical region and (2) have as few clusters as possible. The results for cluster number equals to 6 is chosen and we divide CONUS domain into 6 regions, northwest (NW: 39 sites), California (CA: 22 sites), southwest (SW: 41 sites), Midwest (MW: 12 sites), northeast (NE: 28 sites) and southeast (SE: 18 sites), as shown in Figure 32.

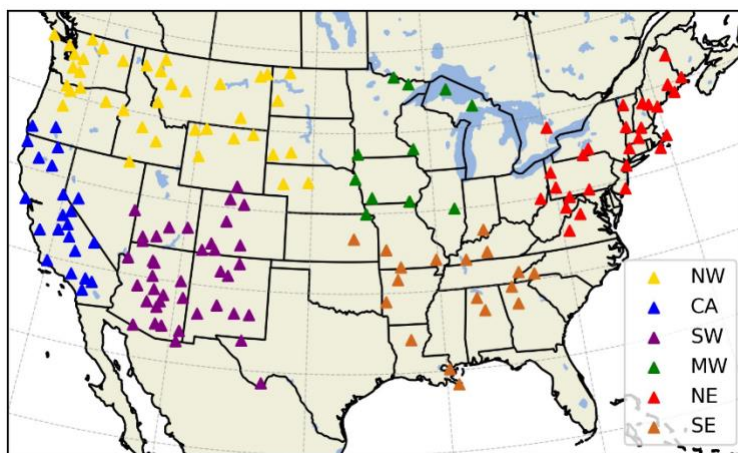


Figure 32. ACCA grouped clusters.

4.2.3 EMSOC

The EMSOC method improves upon the EC tracer method to get an optimized SOC fraction, f_{sec} , using a relatively large dataset. For each season, the OC and EC data within a 5-year window for a given site are used and the window is moved 1 year at a time to cover the period from 2005 to 2020. Our goal is to optimize the seasonal f_{sec} value for a period of 5 years such that,

$$\overline{OC} = \overline{POC} + f_{sec} * \overline{OC} \quad (10)$$

For a given f_{sec} value, we can estimate the daily POC as,

$$POC_{f,day} = (1 - f_{sec}) * OC_{day} \quad (11)$$

where OC_{day} is the observed daily OC concentration for a given site, and $POC_{f,day}$ is the daily POC concentration corresponding to the f_{sec} value. We estimate the daily POC concentration using the same assumption as the EC tracer method,

$$POC_{e,day} = k_f * EC_{day} \quad (12)$$

where EC_{day} is the observed daily EC concentration. We use daily $POC_{f,day}$ data and through-the-origin least square regression to estimate k_f value for each site during the corresponding timeperiod,

$$y = \begin{pmatrix} POC_{f,1} \\ POC_{f,2} \\ POC_{f,3} \\ \dots \\ POC_{f,n} \end{pmatrix}, x = \begin{pmatrix} EC_1 \\ EC_2 \\ EC_3 \\ \dots \\ EC_n \end{pmatrix} \Rightarrow k_f = \frac{x^T y}{x^T x} \quad (13)$$

Using the calculated $POC_{e,day}$ data, Eq. (10) can be written as, derived ratio of POC to EC (k_f), we have the empirical POC and SOC:

$$\overline{OC} = \overline{POC_{e,day}} + f_{sec} * \overline{OC} + \bar{\epsilon} \quad (14)$$

We substitute daily data for OC and $POC_{e,day}$ and obtain,

$$OC_{day} = POC_{E,day} + f_{sec} * \overline{OC} + \epsilon_{day} \quad (15)$$

We optimize the seasonal f_{sec} estimate for a period of 5 years by minimizing the cost function Q,

$$Q = \frac{\sum_{i=1}^N \epsilon_i^2}{N} \quad (16)$$

where N is the number of days in the dataset. Different from Eq. (15), it is also possible to rewrite Eq. (14) as $OC_{day} = POC_{e,day} + f_{sec} * OC_{day} + \epsilon_{day}$ or $OC_{day} = \overline{POC_{e,day}} + f_{sec} * OC_{day} + \epsilon_{day}$. In both cases, it can be shown that the minimum Q value corresponds to $f_{sec} = 1$ which yields an unphysical result. Using the derived f_{sec} , we can proceed to derive the regional mean SOC and POC. This method does not require additional site-specific information, making it applicable to historical OC/EC data from various locations consistently.

4.2.4 SMLR Method for Factor Analysis

We conducted stepwise multiple linear regression (SMLR) analysis on our estimated SOC and ancillary data to quantitatively understand the impacts of biogenic emissions, anthropogenic emissions, fire activity, and radiation on summertime SOC productions. Biogenic emissions were quantified by HCHO TVCDs due to lack of ground-based isoprene observation data. Particulate nitrate and sulfate from the IMPROVE

network were used to assess impacts from anthropogenic emission, while radiation data is from ERA5. Fire carbon emissions were from GFED. Further details on the observational datasets are discussed in previous sections.

Our analysis comprised three key steps: (1) preprocessing and re-gridding data from different sources to match the SOC location; (2) implementing stepwise multiple linear regression (MLR) to identify the significant variables (Table 9); (3) re-fitting the MLR model using the selected significant variables from the stepwise regression and examining the regression output. Prior to constructing the MLR model, we performed necessary log-transformations on sulfate and nitrate data to achieve normal distribution (Figure 33).

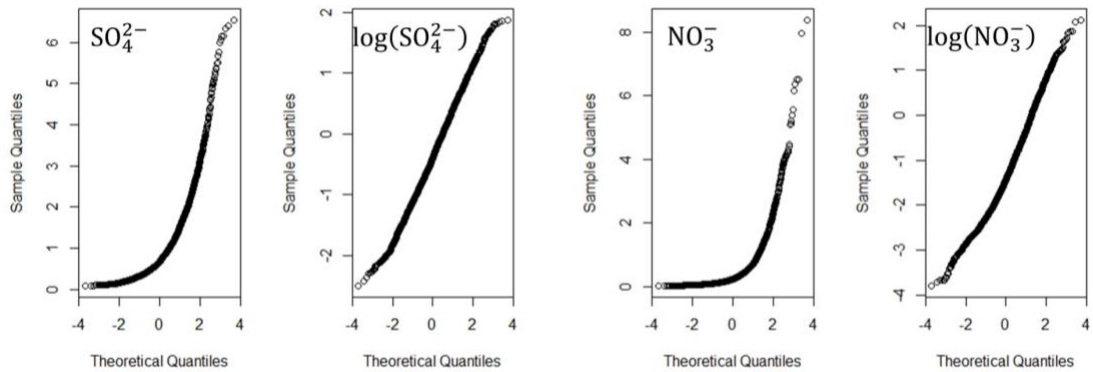


Figure 33. Normal quantile-quantile (Normal QQ) plots before and after log-transformation for sulfate (SO_4^{2-}) and nitrate (NO_3^-).

Table 9. Stepwise regression results for MLR of SOC on log-transformed sulfate ($\log.\text{SO}_4$) and nitrate($\log.\text{NO}_3$), HCHO TVCD (TVCD_HCHO), Fire (Emissions_C) and Radiation (ssrd). Columns from left to right are region names, index for the

selected model, number of predictors selected, selected predictors, correlation coefficient, adjusted correlation coefficient, and Mallow's Cp.

Region	Index	N	Predictors	R ²	Adj.R ²	Mallow's Cp
NW	6	2	log.SO4., TVCD_HCHO	0.158	0.134	0.804
CA	6	2	Emissions_C, log.SO4	0.294	0.275	0.527
SW	26	4	Emissions_C, log.SO4, log.NO3, TVCD_HCHO	0.360	0.338	4.002
MW	1	1	TVCD_HCHO	0.217	0.208	-0.262
NE	5	2	log.df.NO3, TVCD_HCHO	0.148	0.138	1.942
SE	16	3	ssrd, log.SO4, TVCD_HCHO	0.428	0.405	2.214

4.3 Results and Discussions

4.3.1 Regional Clustering and Validation

Compared to the local sources of EC, the variation in OC is primarily influenced by regional factors, owing to its secondary contribution from SOC²⁹¹. Several previous studies have highlighted the regional characteristics of SOC, demonstrating a substantial correlation among various monitoring sites within the same region^{292, 293}. To achieve a more precise estimation of the controlling factors for SOC production in each region, and accurately estimate the regional trends, an enhanced clustering solution for the sites is imperative. This approach should ensure that SOC from different sites within a region are more likely to be governed by the same regional factor and exhibit similar patterns of variation. One effective method for achieving this is correlation clustering²⁸⁹. To group the 160 IMPROVE sites across the CONUS domain, we adopted the average correlation clustering algorithm (ACCA) method²⁹⁰, creating six geographical regions: northwest (NW), California (CA), southwest (SW), Midwest (MW), Northeast (NE) and southeast

(SE), as shown in Figure 32. More details of the clustering analysis can be found in the method section.

Based on the grouping results, we estimated the secondary fractions (SOC/OC) for each region. This estimation was conducted based on historical OC and EC data, on a seasonal basis, covering winter (December-January-February, DJF), spring (March-April-May, MAM), summer (June-July-August, JJA), and fall (September-October-November, SON). For each season, the OC and EC data are extracted utilizing a rolling window spanning 5 years. This window for a given site is subsequently shifted by 1-year intervals, encompassing the period from 2005 to 2020. The choice of a 5-year window considers the trade-off between estimation bias and temporal resolution. Our objective is to determine an optimized secondary fraction which works for mean OC and POC for each site. By assuming that POC and EC share the same combustion sources as in the EC tracer method, we can derive a POC/EC ratio and substitute it into, creating a cost function (Eq. 7) to minimize for obtaining the optimized secondary fraction.

EMSOC-derived secondary fractions (SOC/OC) were compared with the reported data in the literature. To ensure the integrity of our comparison, we extracted corresponding values from our derived dataset, considering the specific region and seasonal coverages of the reported values. PMF using AMS data could also provide information on primary and secondary OC contributions but are not included here. Studies have found that the estimated secondary contributions from AMS data are usually higher than those from the EC tracer method²⁹⁴. One explanation could be related to the fast chemical aging of POC near sources²⁹⁵, where those part of oxygenated OC would be identified as POC in our

methods. In terms of a method-wise comparison (Figure 34(a)), the averaged SOC/OC derived from EMSOC are of similar levels with those estimated by PMF and SOA-tracer methods but tend to be lower when compared with the other two methods, especially with those from CMB. The point-to-point comparison (Figure 35) also shows that SOC/OC derived from CMB lies mostly under the 1:1 line, meaning that they are generally higher than those from EMSOC. The higher SOC estimates from the CMB method can be explained by unconsidered primary OC sources or lack of source profiles, as discussed in previous studies^{296, 297}. The comparison of EMSOC-derived SOC/OC with literature values suggests that our method predicts SOC fractions in a reasonably good range. The mean SOC/OC for each region during our study period is shown in Figure 34(b), ranging from 22% in SE to 40% in SW.

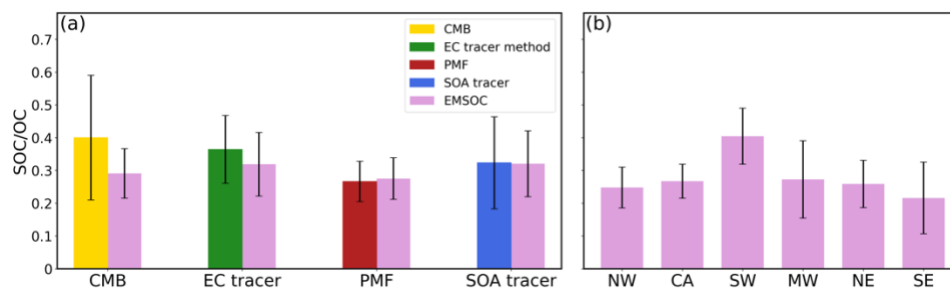


Figure 34. Overview of EMSOC derived secondary ratios (SOC/OC). (a) Validation against other methods; (b) Annual mean EMSOC-derived SOC/OC for each cluster.

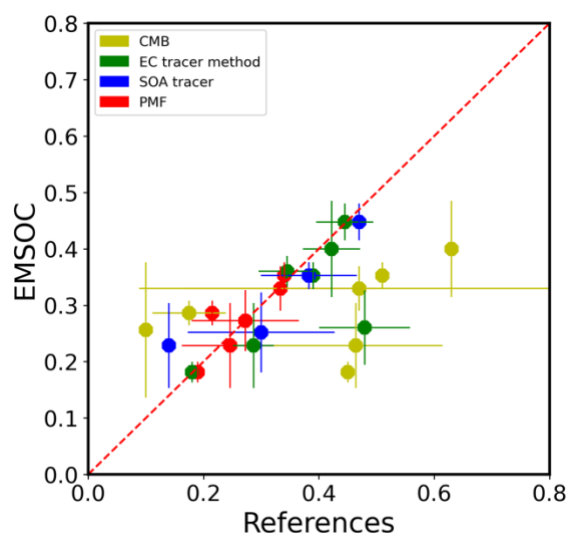


Figure 35. One on one comparison of SOC/OC derived from our study versus previous values.

4.3.2 Factor Analysis of Summertime SOC

We separated OC into empirical SOC and POC through the calculated secondary fractions and investigated their seasonal characteristics. A consistent seasonal pattern of SOC (Figure 36 (a)), with a peak in JJA, confirmed as in previous studies²⁹⁸⁻³⁰⁰, when the photochemical activity is the strongest, is observed for all regions. The summertime peak is pronounced in SE, which has been reported to be primarily affected by the oxidation

processes of emitted BVOCs due to its densely forested condition^{11, 301}. POC does not display distinct seasonal variation across the six regions (Figure 36(b)), which aligns with the indistinct seasonal variation of EC. The seasonal variation of OC primarily stems from that of SOC (Figure 36(c)). Regionally, JJA SOC is higher in the eastern US (NE, SE, and MW) than the western US (0.45-0.65 versus 0.25-0.35 $\mu\text{g C}/\text{m}^3$), with SE exhibiting the highest SOC levels. Additionally, SE POC is also consistently higher than other regions as found in previous studies³⁰⁰. This result may stem from the generally higher OC concentrations over this region. While inter-regional variations SOC reaches its maximum in JJA, other seasons show more homogenous distributions. In contrast, interregional variation in POC remains at a consistent level across all seasons (Figure 36(d)). This result highlights the seasonal dynamics of SOC, indicating heightened chemical activity in summer.

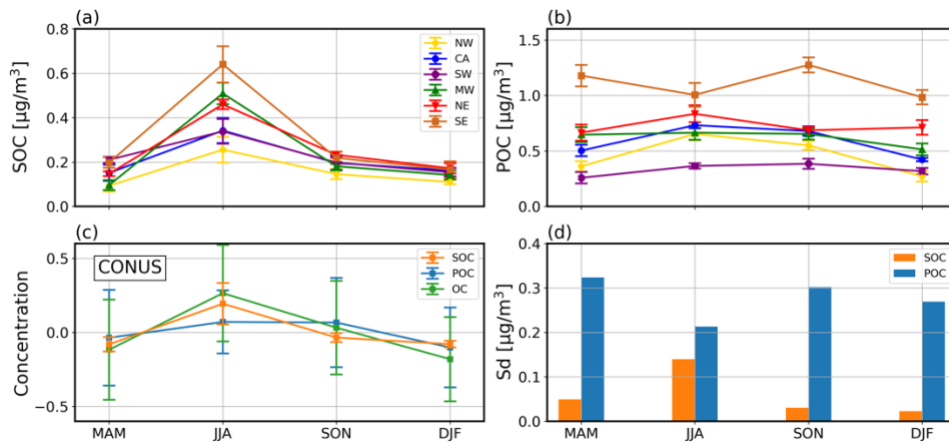


Figure 36. (a) Seasonal variations of SOC for each of the six regions; (b) is similar to (a) but for POC. (c) Normalized seasonal mean and standard deviations of SOC,

POC, and OC for all CONUS sites; (d) inter-regional deviations for SOC and POC in each season.

The substantial inter-regional variations in summer underscore the significance of photochemical oxidation in SOC production, although the factors influencing it can be highly uncertain³⁰². During JJA, biogenic emissions reach their peak and exert a significant influence on SOC formation³⁰³. Simultaneously, anthropogenic factors can directly and indirectly impact this process of biogenic SOC formation^{11, 12, 304}. Contributions from other factors, such as fires, can also play a role^{305, 306}. Given the elevated concentration of SOC in JJA, understanding of the driving factors behind JJA SOC becomes particularly critical for the development of regional regulations. To delve into the effects of biogenic emissions, anthropogenic emissions, fire activity, and radiation on JJA SOC production, we conducted an SMLR analysis on ancillary datasets, with detailed information available in 4.2.4.

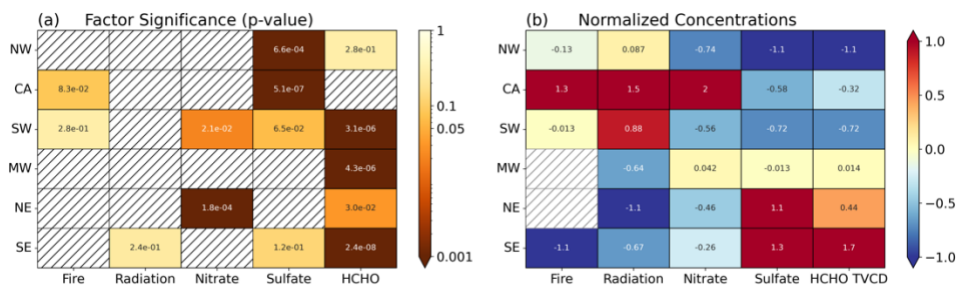


Figure 37. (a) Resulted p-values from MLR built on significant factors, where shaded cells means that the corresponding factor is insignificant. (b) Normalized regional mean concentrations of all factors.

Figure 37 shows the selected variables and their corresponding fitted p-values in the regression results. Notably, we observed that HCHO TVCDs significantly impact most of the regions, with the exception of CA. Considering that most IMPROVE sites located

in rural/remote regions such as national parks ³⁰⁷ with sufficient BVOC emissions, this result suggest that the SOC we derived here is highly likely to be biogenically driven.

Following this strong indication of biogenic SOC formation, sulfate is found to be significant for all three western US regions and SE. Several studies have reported the strong correlation between sulfate with biogenic SOC production³⁰⁸. The uptake of IEPOX, a major oxidation product from ISOP by OH, represents the primary pathway for SOC formation under low NO_x conditions^{309,310}. Previous research has demonstrated that sulfate can enhance the reactive uptake of IEPOX through nucleophilic attack, potentially via the salting-in effect³⁰⁴. Our findings indicate a sulfate dependency of SOC, particularly in low-sulfate regions (Figure 37 (b)), such as the western US. This dependence of SOC on sulfate in low-sulfate regions may signal challenges in reducing SOC in the future. Despite the high sulfate levels in NE, our study does not reveal a significant correlation between sulfate and SOC. This weak correlation between sulfate and SOC might suggest the diverging pathway of sulfate and SOC production in this region, as reported by previous studies³¹¹. In contrast to the significant roles of sulfate, our results indicate a relatively less significant role for nitrate in JJA SOC, which is also more evenly distributed than sulfate in JJA (Figure 37 (b)).

Local fire emissions are found to have significant impacts on JJA SOC in the western US, particularly in CA and SW^{312,313}. With an anticipated increase in PM_{2.5} levels in the US due to escalating wildfires in North America under a warming climate³¹⁴⁻³¹⁶, our findings underscore the importance to account for the fire impact on SOC production.

4.3.3 Increasing SOC Despite Decreasing Anthropogenic Emissions

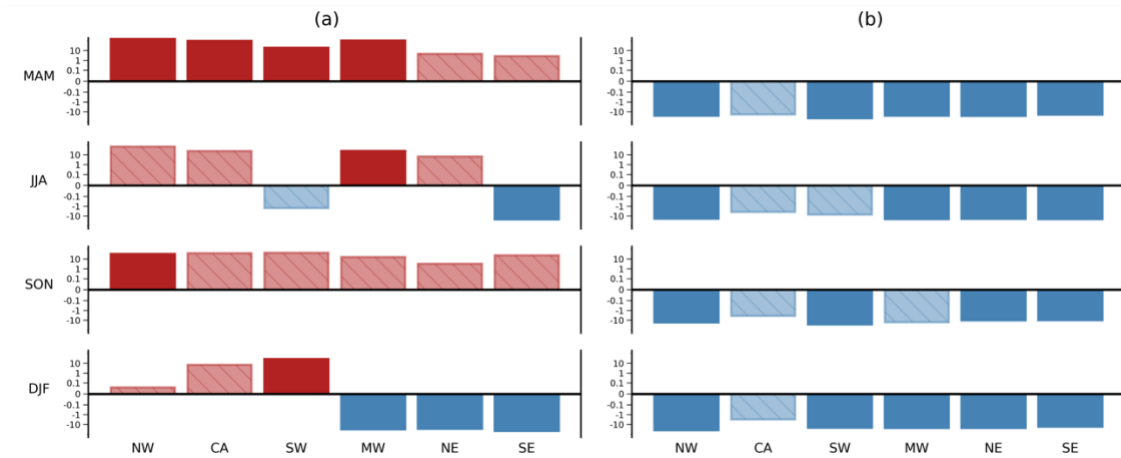


Figure 38. Trend of SOC and POC [percent/decade]. Solid filled cells indicate that the trend is significant, while transparent cells indicate that no significant trend is detected.

Historical trends for all seasons were analyzed for the six regions. Overall, a decreasing trend was observed for POC in all seasons, whereas SOC exhibited contrasting patterns (Figure 38). The decreasing trend in POC aligns with the trends observed for EC, other inorganic $PM_{2.5}$ components, nitrogen dioxides (NO_2), and sulfur dioxides (SO_2) (Figure 39), showing the reduction in anthropogenic emissions in response to EPA

regulations ³¹⁷. Although POC generally follows this declining pattern, the trend for SOC differs in most cases.

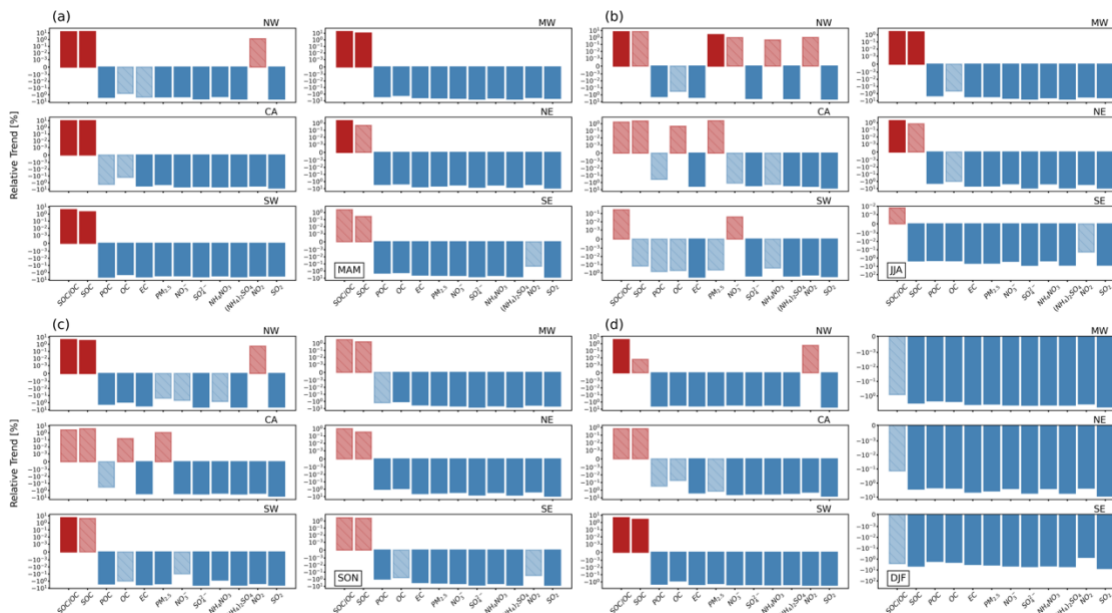


Figure 39. Trends of all species. Solid filled cells indicate that the trend is significant, while transparent cells indicate that no significant trend is detected.

In JJA, which was analyzed previously as the season with the highest SOC concentrations, the historical trends demonstrate the least significance among all the seasons. While some of the trends may be insignificant, an overall increase in SOC was observed across all regions, except for SW and SE. In the case of SW, the insignificant trend can be attributed to less monotonic evolutions, probably caused by the combining effects from many factors, such as the decreasing anthropogenic emissions but increasing fires (Figure 36 (a)). Notably, a significant decreasing trend was observed in the SE region. Considering the biogenic origin of SOC in SE, the decreasing trends of HCHO (Figure 40)

and SO₂, along with a reduction in radiation (Figure 40), could significantly contribute to the decline in SOC.

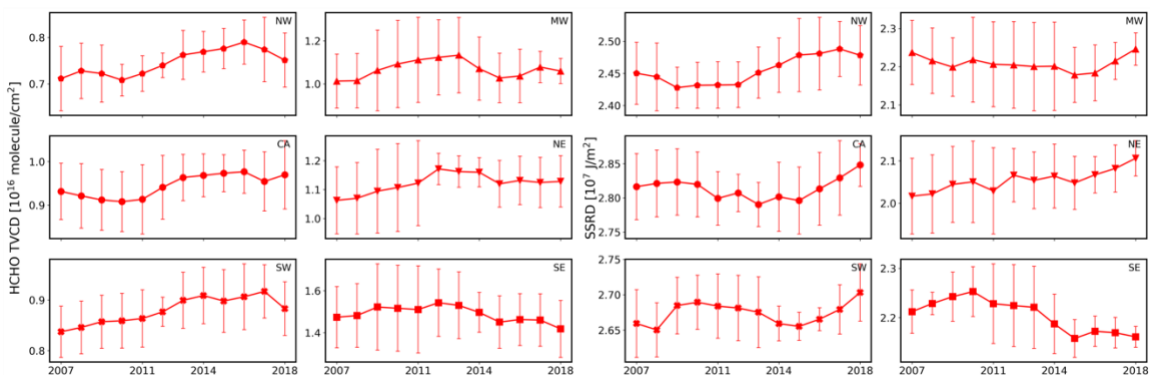


Figure 40. Historical trends for HCHO TVCDs (left) and Surface Solar Radiation Downwards (SSRD) (right).

For the other two regions in the eastern US, NE and MW, the contrasting depiction of the historical trends of SOC and POC is observed. In the western US, significant interannual variations result in less pronounced trends, both positive and negative, not only for SOC but also for POC, OC, and other inorganics. This variations could be attributed to the occurrence of large-scale burning events in recent years^{313, 318}. Studies in central CA have reported impacts of intensified large JJA forest fires on both SOC and POC^{255, 297, 319}. The increasing trend in fire emissions in CA and SW since 2015 (Figure 41) likely contributed to the elevated SOC in these regions during the same period. Fire emissions also impact the northern part of US (NW, MW and NE). While local fire emissions are negligible, an increasing trend in fire emissions from southern Canada (Figure 42) may also contribute to the escalating SOC concentrations in these regions through long-range transport, as suggested in previous studies^{320, 321}. In addition to fire emissions, the NW

region demonstrates a significant increasing trend in PM_{2.5}, as well as an increase in NO₂ and particulate nitrate. Previous research has also identified an increasing background level of NO₂ in the NW US, which may be linked to either trans-Pacific transport or agricultural emissions, necessitating further investigation.³²²

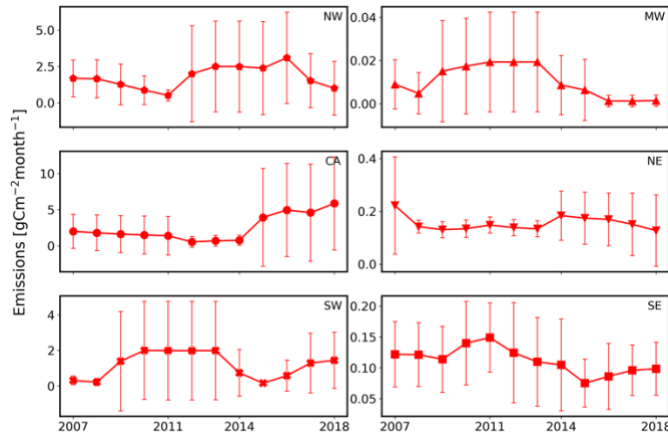


Figure 41. Historical trends for and fire carbon emissions from GFED.

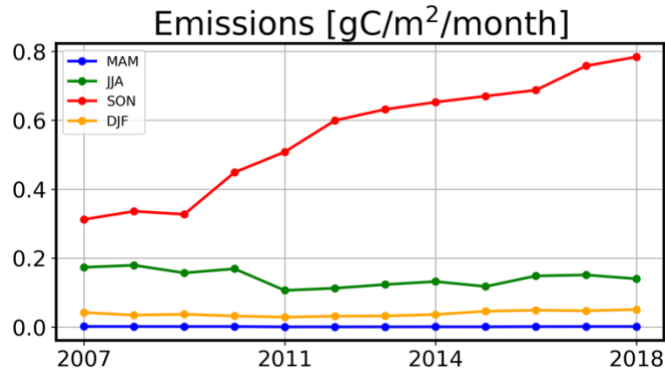


Figure 42. Historical trends for Canadian fire emissions.

For the non-summer seasons, variations across regions are generally limited. Despite continually decreasing anthropogenic emissions, a decreasing trend in SOC is observed only for the eastern US during winter. Studies have indicated a significant influence from burning on SOC production in the eastern US related to both residential heating and local burnings in winter,³²³⁻³²⁵ which may contribute to this decreasing SOC trend. Increasing SOC, whether significant or not, are generally observed in other cases. It is noteworthy that while SOC concentrations exhibit greater variability, the annual mean SOC/OC display increasing trends across all regions (Figure 43), signifying the growing significance of secondary components in OC. Recent health-environmental studies emphasize the significant contribution of SOC to air pollution mortality^{326, 327}. This increasing SOC underscores the importance of exploring its health impacts, emphasizing the need to consider not only primary emissions but also secondary production in PM_{2.5} regulations.

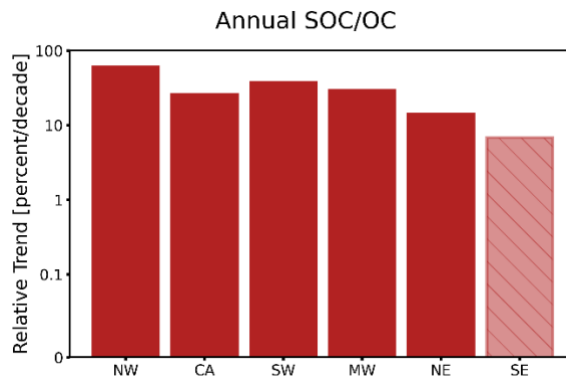


Figure 43. Relative trend of annual SOC/OC. Solid cells indicate that the trend is significant, while transparent cells indicate that the trend is insignificant.

4.4 Conclusions

Current studies on SOC productions are time- and region- limited. Through the ACCA clustering method, we identify six regions across the CONUS domain according to the correlations of measured OC concentrations. We leverage IMPROVE OC and EC data from 2005-2020 to understand the seasonal and historical trends and regional effects. The regional mean SOC/OC vary from 22% to 40%. The comparison of our derived SOC/OC with co-located values reported from previous studies show reasonable agreement, despite a higher bias in the CMB method, likely due to unconsidered POC sources. Unlike POC, which shows insignificant seasonal pattern, SOC exhibits a consistent seasonal pattern, with peak in summer, across all regions, indicating the enhanced photochemical activity during summer. In summer, the interregional variation is also the largest, indicating enhanced photochemical influences. Notably, we found a significant correlation with HCHO of summer SOC for all regions except for CA, where local fires play significant role. Sulfate, as has been discussed in previous studies, play significant role in summertime SOC productions. Our results highlight the regional dependencies of this correlation with sulfate. SOC sensitivity to sulfate is more pronounced over western US, which is characterized by low sulfate concentrations. In contrast, regions with abundant sulfate, such as NE or SE, weak or even non-existent correlations with sulfate are observed. While POC decrease along with decreasing anthropogenic emissions across the United States, SOC does not follow the trend and even increase in some cases. Statistically significant decreasing SOC trend is found only in the three eastern US regions (MW, NE, and SE) in winter and SE in summer. While for other seasons, statistically significant increasing trends, or insignificant positive trends are found in SOC. Accordingly, increasing annual

mean SOC contribution to OC (SOC/OC) is found for all regions except for SE, where no significant trend is detected. The relative trend ranges from 14% to 60% per decade. Meanwhile, recently increasing fire activities over the western United States in summer to fall underscores the difficulty in future reduction of OC through reduction of anthropogenic emissions in the corresponding fire-affected regions. Increasing secondary contribution to OC highlights the need to investigate SOC production for future air quality regulation.

CHAPTER 5. CONCLUSIONS AND FUTURE WORK

This thesis gain insights into the atmospheric chemistry processes regarding O₃ and PM_{2.5} pollutions through observational and modeling analysis. Utilizing comprehensive datasets of both ground-based and satellite-based measurements of trace gases and particles, we gain insights into HONO photoactive production mechanisms and their implications for O₃ production, the uncertainties of satellite retrievals of NO₂ and HCHO, as well as the historical and seasonal trends of SOC across CONUS.

5.1 Observation-based Diagnostic of Photoactive Heterogeneous HONO Sources and their Divergent Implications for Ozone Production

Our modeling analysis of the OPECE gaseous and particulate measurements at a rural coastal site in Shandong, China reaffirmed the presence of daytime heterogeneous production of HONO on aerosols, in line with findings from previous studies. The modeling equivalency of different HONO production mechanisms underscored the intrinsic interplay between NO₂, pNO₃, and HNO₃ in the chemical system. This emphasized that inland in situ observations may not provide sufficient constraints to investigate the heterogeneous HONO production mechanisms. Furthermore, the conversion of HONO from pNO₃ was observed to potentially lead to marked elevations of O₃ in the downwind regions from emission sources. This process may have global implications, potentially impacting even marine environments. Conversely, the photoactive conversion of HONO from NO₂ on aerosols can shift the transition regime, when O₃ production becomes insensitive to NO_x, to higher NO_x conditions, consequently

flattening the increase in PO_3 with decreasing NO_x , when compared to other mechanisms or scenarios without heterogeneous HONO production. Additionally, our analysis on BB indicated that high HONO concentrations during BB can be attributed to the increased level of HONO precursors, such as NO_x or pNO_3 , rather than primary emissions of HONO.

Future work could involve Lagrangian experiments conducted away from emission sources, tracking the evolutions of HONO/ NO_2 , HONO/ pNO_3 , and NO_x/pNO_3 ratios over 1-2 days of chemical aging. Such experiments could provide deeper insights into the underlying HONO production mechanism, as the three mechanisms exhibit markedly distinct predictions of the ratios. Quantifying HONO production on aerosols has profound implications for understanding O_3 pollution and is important to formulating effective O_3 mitigation strategies. Considering the increasing burning activities due to global warming in recent years, an in-depth exploration of the impact of BB on HONO and HONO production pathways is essential not only for understanding the mechanisms of HONO production in BB plumes but also for assessing the impacts of BB on O_3 production. In addition, integrating these HONO heterogeneous production pathways into a 3D model could help quantify and compare their impacts on regions with different emission conditions.

5.2 Remote Sensing Measurements at a Rural Site in China: Implications for Satellite NO_2 and HCHO Measurement Uncertainty and Emissions from Fires

Validations of satellite NO_2 and HCHO products using ground-based MAX-DOAS observations on days without local burnings are conducted after unifying the a priori

profiles for satellite and MAX-DOAS products using REAM simulated vertical profiles. The comparative analysis revealed that the agreement between satellite and MAX-DOAS data is generally better for NO₂ products than for HCHO products, which could be attributed partly to the nature of lower sensitivity of UV band to HCHO in the lower atmosphere due to stronger Rayleigh scattering. Nevertheless, the TROPOMI HCHO product displayed considerable potential for improvement compared to OMI products. For satellite NO₂ products, the two OMI products exhibit a ~30% bias from each other even when using the same a priori profiles, linked to a differed estimation of scattering weight profiles in the lower troposphere. Further analysis indicated that this discrepancy could be partially attributed to the more extensive cloud presence above the boundary layer around the observation site in the OMI-NASA NO₂ products. Additionally, on days with local burnings, our analysis of the effects of BB on boundary layer HONO, NO₂, and HCHO using MAX-DOAS observations revealed substantial enhancements in their concentrations. Notably, the enhancements of NO₂ and HCHO often coincided, whereas the fire-induced enhancements of HONO exhibited higher variability.

Our current analysis focuses mainly on the two OMI products due to lack of TROPOMI standard product (i.e., TROPOMI v2) during our study period. Future efforts could incorporate the TROPOMI standard product into comparisons, leveraging its improved quality and resolution to gain a more nuanced understanding of the observed discrepancies in the two OMI products. Extending the scope of this study to broader regions to determine whether the observed differences in scattering weight profiles possess regional characteristics, quantifying the relative significance of this discrepancy in

different regions would help to gain implications for regional trend studies utilizing satellite products. Furthermore, a better understanding of HONO production mechanisms could help us better understand the variable BB impact on HONO and the consequent impact on O₃ production. Lastly, our study shows that the discrepancy between two OMI NO₂ products stem from their different cloud properties and surface reflectivity data, a comparison of their results after unifying the cloud properties and surface reflectivity separately could help better target the main source contributing to the discrepancies.

5.3 Seasonal and Historical Trends of Secondary Organic Carbon across the Continental United States

We identify six regions across CONUS according to OC concentration correlations across different sites through the ACCA clustering method. Using IMPROVE OC and EC data spanning 15 years (2005-2020), we estimate SOC and POC to understand the seasonal and historical trends, as well as regional effects. The regional mean SOC/OC varies from 22% to 44% and is consistent with co-located values reported by previous studies. Unlike POC, SOC exhibits a consistent seasonal pattern with a summer peak, indicating enhanced photochemical influences in JJA, which results in large inter-regional variations. Employing SMLR analysis, we found that JJA SOC correlated well with HCHO across all regions except for CA, where local fires played a significant role. In addition, our results underscore the regional dependencies of the correlation of SOC with sulfate, that SOC sensitivity to sulfate is more pronounced over western US, where sulfate concentrations are generally lower. While POC decrease along with decreasing anthropogenic emissions across the United States, SOC does not follow the trend and even increase in some cases.

Statistically significant decreasing SOC trend is found only in the three eastern US regions (MW, NE, and SE) in DJF and SE in JJA. While for other seasons, statistically significant increasing trends, or insignificant positive trends are found in SOC. Accordingly, increasing annual mean SOC/OC is found for all regions except for SE, where no significant trend is detected. The relative trend ranges from 14% to 60% per decade. Meanwhile, increasing fire activities over western US and Canada in recent years underscores the difficulty in future reduction of OC through reduction of anthropogenic emissions in the corresponding fire-affected regions, such as western and northern US. Increasing secondary contribution to OC highlights the need to investigate SOC production for future air quality regulations.

In-source formation (ISF) process has recently been found to be a major contributor to ambient particulate sulfate which highlights the importance of an accurate quantification of “primary emissions” in the models^{295, 328}. It should be noted that the secondary fraction derived from OC/EC-related measurements as employed in our study, does not account for SOC formed through the ISF process due to its correlation with EC. This may result in lower secondary fractions when compared to those derived from element-based measurements, such as AMS or ACSM (Figure 44). As long-term measurement campaigns equipped with these instruments, such as ASCENT, are underway, future work should include comparisons and combinations of the results from ASCENT measurements to enhance our comprehensive understanding of SOC across the US.

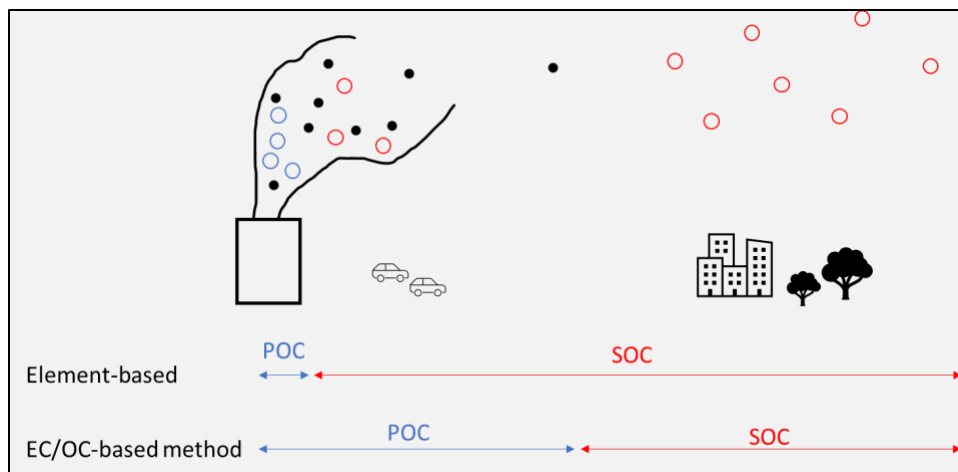


Figure 44. Illustration of the accounted SOC in two methods

Future investigations could involve a more detailed analysis of the regional characteristics of SOC production within each specific region. Integrating additional factors and a larger sample size into the SMLR analysis of SOC could further refine and achieve a more robust identification of significant factors. Considering the increasing wildfire frequencies under a warming climate, back-trajectory simulations which could quantify impacts from transported fire emissions could help to improve the understanding of the fire impact on SOC production, in both local emissions and long-range transport.

REFERENCES

- (1) Lippmann, M. HEALTH EFFECTS OF OZONE A Critical Review. *JAPCA* **1989**, *39* (5), 672-695. DOI: 10.1080/08940630.1989.10466554.
- (2) Cohen, A. J.; Brauer, M.; Burnett, R.; Anderson, H. R.; Frostad, J.; Estep, K.; Balakrishnan, K.; Brunekreef, B.; Dandona, L.; Dandona, R.; et al. Estimates and 25-year trends of the global burden of disease attributable to ambient air pollution: an analysis of data from the Global Burden of Diseases Study 2015. *The Lancet* **2017**, *389* (10082), 1907-1918. DOI: 10.1016/S0140-6736(17)30505-6 (accessed 2023/10/22).
- (3) Manisalidis, I.; Stavropoulou, E.; Stavropoulos, A.; Bezirtzoglou, E. Environmental and Health Impacts of Air Pollution: A Review. *Frontiers in Public Health* **2020**, *8*, Review. DOI: 10.3389/fpubh.2020.00014.
- (4) WHO. *WHO global air quality guidelines*; WHO, 2021. <https://www.who.int/publications/i/item/9789240034228>.
- (5) Wang, T.; Xue, L.; Brimblecombe, P.; Lam, Y. F.; Li, L.; Zhang, L. Ozone pollution in China: A review of concentrations, meteorological influences, chemical precursors, and effects. *Science of The Total Environment* **2017**, *575*, 1582-1596. DOI: <https://doi.org/10.1016/j.scitotenv.2016.10.081>.
- (6) Wang, W.; Parrish, D. D.; Wang, S.; Bao, F.; Ni, R.; Li, X.; Yang, S.; Wang, H.; Cheng, Y.; Su, H. Long-term trend of ozone pollution in China during 2014–2020: distinct seasonal and spatial characteristics and ozone sensitivity. *Atmos. Chem. Phys.* **2022**, *22* (13), 8935-8949. DOI: 10.5194/acp-22-8935-2022.
- (7) Xiao, Q.; Geng, G.; Xue, T.; Liu, S.; Cai, C.; He, K.; Zhang, Q. Tracking PM_{2.5} and O₃ Pollution and the Related Health Burden in China 2013–2020. *Environmental Science & Technology* **2022**, *56* (11), 6922-6932. DOI: 10.1021/acs.est.1c04548.
- (8) Gil-Alana, L. A.; Yaya, O. S.; Awolaja, O. G.; Cristofaro, L. Long Memory and Time Trends in Particulate Matter Pollution (PM_{2.5} and PM₁₀) in the 50 U.S. States. *Journal of Applied Meteorology and Climatology* **2020**, *59* (8), 1351-1367. DOI: 10.1175/JAMC-D-20-0040.1.
- (9) Chung, S. H.; Seinfeld, J. H. Global distribution and climate forcing of carbonaceous aerosols. *Journal of Geophysical Research: Atmospheres* **2002**, *107* (D19), AAC 14-11-AAC 14-33. DOI: <https://doi.org/10.1029/2001JD001397>.
- (10) Zhang, Q.; Jimenez, J. L.; Canagaratna, M. R.; Allan, J. D.; Coe, H.; Ulbrich, I.; Alfarra, M. R.; Takami, A.; Middlebrook, A. M.; Sun, Y. L.; et al. Ubiquity and dominance of oxygenated species in organic aerosols in anthropogenically-influenced Northern

Hemisphere midlatitudes. *Geophysical Research Letters* **2007**, *34* (13), n/a-n/a. DOI: 10.1029/2007gl029979.

(11) Weber, R. J.; Sullivan, A. P.; Peltier, R. E.; Russell, A.; Yan, B.; Zheng, M.; de Gouw, J.; Warneke, C.; Brock, C.; Holloway, J. S.; et al. A study of secondary organic aerosol formation in the anthropogenic - influenced southeastern United States. *Journal of Geophysical Research: Atmospheres* **2007**, *112* (D13). DOI: 10.1029/2007jd008408.

(12) Ng, N. L.; Chhabra, P. S.; Chan, A. W. H.; Surratt, J. D.; Kroll, J. H.; Kwan, A. J.; McCabe, D. C.; Wennberg, P. O.; Sorooshian, A.; Murphy, S. M.; et al. Effect of NO_x level on secondary organic aerosol (SOA) formation from the photooxidation of terpenes. *Atmos. Chem. Phys.* **2007**, *7* (19), 5159-5174. DOI: 10.5194/acp-7-5159-2007.

(13) Shrivastava, M.; Cappa, C. D.; Fan, J.; Goldstein, A. H.; Guenther, A. B.; Jimenez, J. L.; Kuang, C.; Laskin, A.; Martin, S. T.; Ng, N. L.; et al. Recent advances in understanding secondary organic aerosol: Implications for global climate forcing. *Reviews of Geophysics* **2017**, *55* (2), 509-559. DOI: 10.1002/2016rg000540.

(14) Lee, Y.; Huey, L. G.; Wang, Y.; Qu, H.; Zhang, R.; Ji, Y.; Tanner, D. J.; Wang, X.; Tang, J.; Song, W.; et al. Photochemistry of Volatile Organic Compounds in the Yellow River Delta, China: Formation of O₃ and Peroxyacyl Nitrates. *Journal of Geophysical Research: Atmospheres* **2021**, *126* (23), e2021JD035296. DOI: <https://doi.org/10.1029/2021JD035296>.

(15) Li, J.; Wang, Y. Inferring the anthropogenic NO_x emission trend over the United States during 2003–2017 from satellite observations: was there a flattening of the emission trend after the Great Recession? *Atmos. Chem. Phys.* **2019**, *19* (24), 15339-15352. DOI: 10.5194/acp-19-15339-2019.

(16) Liu, Z.; Wang, Y.; Gu, D.; Zhao, C.; HUEY, L. G.; STICKEL, R.; LIAO, J.; Shao, M.; Zhu, T.; Zeng, L.; et al. Evidence of Reactive Aromatics As a Major Source of Peroxy Acetyl Nitrate over China. **2010**.

(17) Liu, Z.; Wang, Y.; Gu, D.; Zhao, C.; Huey, L. G.; Stickel, R.; Liao, J.; Shao, M.; Zhu, T.; Zeng, L.; et al. Summertime photochemistry during CAREBeijing-2007: RO_x budgets and O₃ formation. *Atmospheric Chemistry and Physics* **2012**, *12* (16), 7737-7752. DOI: 10.5194/acp-12-7737-2012.

(18) Qu, H.; Wang, Y.; Zhang, R.; Liu, X.; Huey, L. G.; Sjostedt, S.; Zeng, L.; Lu, K.; Wu, Y.; Shao, M.; et al. Chemical Production of Oxygenated Volatile Organic Compounds Strongly Enhances Boundary-Layer Oxidation Chemistry and Ozone Production. *Environmental Science & Technology* **2021**, *55* (20), 13718-13727. DOI: 10.1021/acs.est.1c04489.

(19) Yan, Q.; Wang, Y.; Cheng, Y.; Li, J. Summertime Clean-Background Ozone Concentrations Derived from Ozone Precursor Relationships are Lower than Previous

Estimates in the Southeast United States. *Environmental Science & Technology* **2021**, *55* (19), 12852-12861. DOI: 10.1021/acs.est.1c03035.

(20) Johnson, M. S.; Souri, A. H.; Philip, S.; Kumar, R.; Naeger, A.; Geddes, J.; Judd, L.; Janz, S.; Chong, H.; Sullivan, J. Satellite remote-sensing capability to assess tropospheric-column ratios of formaldehyde and nitrogen dioxide: case study during the Long Island Sound Tropospheric Ozone Study 2018 (LISTOS 2018) field campaign. *Atmos. Meas. Tech.* **2023**, *16* (9), 2431-2454. DOI: 10.5194/amt-16-2431-2023.

(21) Liu, Z.; Wang, Y.; Costabile, F.; Amoroso, A.; Zhao, C.; Huey, L. G.; Stickel, R.; Liao, J.; Zhu, T. Evidence of aerosols as a media for rapid daytime HONO production over China. *Environ Sci Technol* **2014**, *48* (24), 14386-14391. DOI: 10.1021/es504163z.

(22) Qu, H.; Wang, Y.; Zhang, R.; Li, J. Extending Ozone-Precursor Relationships in China From Peak Concentration to Peak Time. *Journal of Geophysical Research: Atmospheres* **2020**, *125* (22), e2020JD033670. DOI: <https://doi.org/10.1029/2020JD033670>.

(23) Dusanter, S.; Vimal, D.; Stevens, P. S.; Volkamer, R.; Molina, L. T.; Baker, A.; Meinardi, S.; Blake, D.; Sheehy, P.; Merten, A.; et al. Measurements of OH and HO₂ concentrations during the MCMA-2006 field campaign – Part 2: Model comparison and radical budget. *Atmos. Chem. Phys.* **2009**, *9* (18), 6655-6675. DOI: 10.5194/acp-9-6655-2009.

(24) Kleffmann, J. Daytime formation of nitrous acid: A major source of OH radicals in a forest. *Geophysical Research Letters* **2005**, *32* (5). DOI: 10.1029/2005gl022524.

(25) Kim, S.; VandenBoer, T. C.; Young, C. J.; Riedel, T. P.; Thornton, J. A.; Swarthout, B.; Sive, B.; Lerner, B.; Gilman, J. B.; Warneke, C.; et al. The primary and recycling sources of OH during the NACHTT-2011 campaign: HONO as an important OH primary source in the wintertime. *Journal of Geophysical Research: Atmospheres* **2014**, *119* (11), 6886-6896, <https://doi.org/10.1002/2013JD019784>. DOI: <https://doi.org/10.1002/2013JD019784> (accessed 2021/06/22).

(26) Alicke, B.; Platt, U.; Stutz, J. Impact of nitrous acid photolysis on the total hydroxyl radical budget during the Limitation of Oxidant Production/Pianura Padana Produzione di Ozono study in Milan. *Journal of Geophysical Research: Atmospheres* **2002**, *107* (D22), LOP 9-1-LOP 9-17. DOI: <https://doi.org/10.1029/2000JD000075> (accessed 2023/09/24).

(27) Lu, X.; Wang, Y.; Li, J.; Shen, L.; Fung, J. C. H. Evidence of heterogeneous HONO formation from aerosols and the regional photochemical impact of this HONO source. *Environmental Research Letters* **2018**, *13* (11). DOI: 10.1088/1748-9326/aae492.

(28) Xing, L.; Wu, J.; Elser, M.; Tong, S.; Liu, S.; Li, X.; Liu, L.; Cao, J.; Zhou, J.; El-Haddad, I.; et al. Wintertime secondary organic aerosol formation in Beijing–Tianjin–Hebei (BTH): contributions of HONO sources and heterogeneous reactions. *Atmospheric Chemistry and Physics* **2019**, *19* (4), 2343-2359. DOI: 10.5194/acp-19-2343-2019.

- (29) Liu, P.; Xue, C.; Ye, C.; Liu, C.; Zhang, C.; Wang, J.; Zhang, Y.; Liu, J.; Mu, Y. The Lack of HONO Measurement May Affect the Accurate Diagnosis of Ozone Production Sensitivity. *ACS Environmental Au* **2023**, *3* (1), 18-23. DOI: 10.1021/acsenvironau.2c00048.
- (30) Li, Q.; Zhang, L.; Wang, T.; Wang, Z.; Fu, X.; Zhang, Q. "New" Reactive Nitrogen Chemistry Reshapes the Relationship of Ozone to Its Precursors. *Environ Sci Technol* **2018**, *52* (5), 2810-2818. DOI: 10.1021/acs.est.7b05771.
- (31) Pagsberg, P.; Bjergbakke, E.; Ratajczak, E.; Sillesen, A. Kinetics of the gas phase reaction OH + NO(+ M) HONO(+ M) and the determination of the UV absorption cross sections of HONO. *Chemical Physics Letters* **1997**.
- (32) Burling, I. R.; Yokelson, R. J.; Griffith, D. W. T.; Johnson, T. J.; Veres, P.; Roberts, J. M.; Warneke, C.; Urbanski, S. P.; Reardon, J.; Weise, D. R.; et al. Laboratory measurements of trace gas emissions from biomass burning of fuel types from the southeastern and southwestern United States. *Atmospheric Chemistry and Physics* **2010**, *10* (22), 11115-11130. DOI: 10.5194/acp-10-11115-2010.
- (33) Veres, P.; Roberts, J. M.; Burling, I. R.; Warneke, C.; de Gouw, J.; Yokelson, R. J. Measurements of gas-phase inorganic and organic acids from biomass fires by negative-ion proton-transfer chemical-ionization mass spectrometry. *Journal of Geophysical Research: Atmospheres* **2010**, *115* (D23). DOI: <https://doi.org/10.1029/2010JD014033>.
- (34) Neuman, J. A.; Trainer, M.; Brown, S. S.; Min, K. E.; Nowak, J. B.; Parrish, D. D.; Peischl, J.; Pollack, I. B.; Roberts, J. M.; Ryerson, T. B.; et al. HONO emission and production determined from airborne measurements over the Southeast U.S. *Journal of Geophysical Research: Atmospheres* **2016**, *121* (15), 9237-9250. DOI: 10.1002/2016jd025197.
- (35) Theys, N.; Volkamer, R.; Müller, J. F.; Zarzana, K. J.; Kille, N.; Clarisse, L.; De Smedt, I.; Lerot, C.; Finkenzeller, H.; Hendrick, F.; et al. Global nitrous acid emissions and levels of regional oxidants enhanced by wildfires. *Nature Geoscience* **2020**, *13* (10), 681-686. DOI: 10.1038/s41561-020-0637-7.
- (36) Roberts, J. M.; Stockwell, C. E.; Yokelson, R. J.; de Gouw, J.; Liu, Y.; Selimovic, V.; Koss, A. R.; Sekimoto, K.; Coggon, M. M.; Yuan, B.; et al. The nitrogen budget of laboratory-simulated western US wildfires during the FIREX 2016 Fire Lab study. *Atmos. Chem. Phys.* **2020**, *20* (14), 8807-8826. DOI: 10.5194/acp-20-8807-2020.
- (37) Xu, L.; Crouse, J. D.; Vasquez, K. T.; Allen, H.; Wennberg, P. O.; Bourgeois, I.; Brown, S. S.; Campuzano-Jost, P.; Coggon, M. M.; Crawford, J. H.; et al. Ozone chemistry in western U.S. wildfire plumes. *Science Advances* **2021**, *7* (50), eabl3648. DOI: doi:10.1126/sciadv.abl3648.

- (38) Li, X.; Rohrer, F.; Hofzumahaus, A.; Brauers, T.; Häseler, R.; Bohn, B.; Broch, S.; Fuchs, H.; Gomm, S.; Holland, F.; et al. Missing Gas-Phase Source of HONO Inferred from Zeppelin Measurements in the Troposphere. *Science* **2014**, *344* (6181), 292-296. DOI: 10.1126/science.1248999.
- (39) Michoud, V.; Colomb, A.; Borbon, A.; Miet, K.; Beekmann, M.; Camredon, M.; Aumont, B.; Perrier, S.; Zapf, P.; Siour, G.; et al. Study of the unknown HONO daytime source at a European suburban site during the MEGAPOLI summer and winter field campaigns. *Atmos. Chem. Phys.* **2014**, *14* (6), 2805-2822. DOI: 10.5194/acp-14-2805-2014.
- (40) Lammel, G.; Cape, J. N. Nitrous acid and nitrite in the atmosphere. *Chemical Society Reviews* **1996**, *25* (5), 361-369, 10.1039/CS9962500361. DOI: 10.1039/CS9962500361.
- (41) Finlayson-Pitts, B. J.; Wingen, L. M.; Sumner, A. L.; Syomin, D.; Ramazan, K. A. The heterogeneous hydrolysis of NO₂ in laboratory systems and in outdoor and indoor atmospheres: An integrated mechanism. *Physical Chemistry Chemical Physics* **2003**, *5* (2), 223-242, 10.1039/B208564J. DOI: 10.1039/B208564J.
- (42) Kleffmann, J.; Becker, K.; Wiesen, P. Heterogeneous NO₂ conversion processes on acid surfaces: possible atmospheric implications. *Atmospheric Environment* **1998**, *32* (16), 2721-2729.
- (43) Reisinger, A. R. Observations of HNO₂ in the polluted winter atmosphere: possible heterogeneous production on aerosols. *Atmospheric Environment* **2000**, *34* (23), 3865-3874. DOI: [https://doi.org/10.1016/S1352-2310\(00\)00179-5](https://doi.org/10.1016/S1352-2310(00)00179-5).
- (44) Tuite, K.; Thomas, J. L.; Veres, P. R.; Roberts, J. M.; Stevens, P. S.; Griffith, S. M.; Dusanter, S.; Flynn, J. H.; Ahmed, S.; Emmons, L.; et al. Quantifying Nitrous Acid Formation Mechanisms Using Measured Vertical Profiles During the CalNex 2010 Campaign and 1D Column Modeling. *Journal of Geophysical Research: Atmospheres* **2021**, *126* (13), e2021JD034689. DOI: <https://doi.org/10.1029/2021JD034689>.
- (45) Xue, C.; Zhang, C.; Ye, C.; Liu, P.; Catoire, V.; Krysztofiak, G.; Chen, H.; Ren, Y.; Zhao, X.; Wang, J.; et al. HONO Budget and Its Role in Nitrate Formation in the Rural North China Plain. *Environ Sci Technol* **2020**, *54* (18), 11048-11057. DOI: 10.1021/acs.est.0c01832.
- (46) Zheng, J.; Shi, X.; Ma, Y.; Ren, X.; Jabbour, H.; Diao, Y.; Wang, W.; Ge, Y.; Zhang, Y.; Zhu, W. Contribution of nitrous acid to the atmospheric oxidation capacity in an industrial zone in the Yangtze River Delta region of China. *Atmospheric Chemistry and Physics* **2020**, *20* (9), 5457-5475. DOI: 10.5194/acp-20-5457-2020.
- (47) Stutz, J.; Alicke, B.; Neftel, A. Nitrous acid formation in the urban atmosphere: Gradient measurements of NO₂ and HONO over grass in Milan, Italy. *Journal of*

Geophysical Research: Atmospheres **2002**, 107 (D22), LOP 5-1-LOP 5-15. DOI: <https://doi.org/10.1029/2001JD000390>.

(48) Notholt, J.; Hjorth, J.; Raes, F. Formation of HNO₂ on aerosol surfaces during foggy periods in the presence of NO and NO₂. *Atmospheric Environment. Part A. General Topics* **1992**, 26 (2), 211-217. DOI: [https://doi.org/10.1016/0960-1686\(92\)90302-2](https://doi.org/10.1016/0960-1686(92)90302-2).

(49) Ammann, M.; Kalberer, M.; Jost, D. T.; Tobler, L.; Rossler, E.; Piguet, D.; W., G. H.; Baltensperger, U. Heterogeneous production of nitrous acid on soot in polluted air masses. *Nature* **1998**.

(50) George, C.; Strekowski, R. S.; Kleffmann, J.; Stemmler, K.; Ammann, M. Photoenhanced uptake of gaseous NO₂ on solid organic compounds: a photochemical source of HONO? *Faraday Discuss* **2005**, 130, 195-210; discussion 241-164, 519-124. DOI: 10.1039/b417888m.

(51) Ramazan, K. A.; Syomin, D.; Finlayson-Pitts, B. J. The photochemical production of HONO during the heterogeneous hydrolysis of NO₂. *Physical Chemistry Chemical Physics* **2004**, 6 (14), 3836-3843, 10.1039/B402195A. DOI: 10.1039/B402195A.

(52) Gustafsson, R. J.; Orlov, A.; Griffiths, P. T.; Cox, R. A.; Lambert, R. M. Reduction of NO₂ to nitrous acid on illuminated titanium dioxide aerosol surfaces: implications for photocatalysis and atmospheric chemistry. *Chemical Communications* **2006**, (37), 3936-3938, 10.1039/B609005B. DOI: 10.1039/B609005B.

(53) Stemmler, K.; Ammann, M.; Donders, C.; Kleffmann, J.; George, C. Photosensitized reduction of nitrogen dioxide on humic acid as a source of nitrous acid. *Nature* **2006**, 440 (7081), 195-198. DOI: 10.1038/nature04603.

(54) Ndour, M.; D'Anna, B.; George, C.; Ka, O.; Balkanski, Y.; Kleffmann, J.; Stemmler, K.; Ammann, M. Photoenhanced uptake of NO₂ on mineral dust: Laboratory experiments and model simulations. *Geophysical Research Letters* **2008**, 35 (5). DOI: 10.1029/2007GL032006 (accessed 2020/07/17).

(55) Wang, S.; Ackermann, R.; Spicer, C. W.; Fast, J. D.; Schmeling, M.; Stutz, J. Atmospheric observations of enhanced NO₂-HONO conversion on mineral dust particles. *Geophysical Research Letters* **2003**, 30 (11). DOI: <https://doi.org/10.1029/2003GL017014>.

(56) Jiang, Y.; Xue, L.; Gu, R.; Jia, M.; Zhang, Y.; Wen, L.; Zheng, P.; Chen, T.; Li, H.; Shan, Y.; et al. Sources of nitrous acid (HONO) in the upper boundary layer and lower free troposphere of North China Plain: insights from the Mount Tai Observatory. *Atmos. Chem. Phys.* **2020**. DOI: 10.5194/acp-2020-377.

- (57) Colussi, A. J.; Enami, S.; Yabushita, A.; Hoffmann, M. R.; Liu, W. G.; Mishra, H.; Goddard, W. A., 3rd. Tropospheric aerosol as a reactive intermediate. *Faraday Discuss* **2013**, *165*, 407-420. DOI: 10.1039/c3fd00040k.
- (58) Ricker, H. M.; Leonardi, A.; Navea, J. G. Reduction and Photoreduction of NO₂ in Humic Acid Films as a Source of HONO, ClNO, N₂O, NO_x, and Organic Nitrogen. *ACS Earth and Space Chemistry* **2022**, *6* (12), 3066-3077. DOI: 10.1021/acsearthspacechem.2c00282.
- (59) Ye, C.; Zhang, N.; Gao, H.; Zhou, X. Photolysis of Particulate Nitrate as a Source of HONO and NO_x. *Environ Sci Technol* **2017**, *51* (12), 6849-6856. DOI: 10.1021/acs.est.7b00387.
- (60) Zhou, X.; Zhang, N.; TerAvest, M.; Tang, D.; Hou, J.; Bertman, S.; Alaghmand, M.; Shepson, P. B.; Carroll, M. A.; Griffith, S.; et al. Nitric acid photolysis on forest canopy surface as a source for tropospheric nitrous acid. *Nature Geoscience* **2011**, *4* (7), 440-443. DOI: 10.1038/ngeo1164.
- (61) Andersen, S. T.; Carpenter, L. J.; Reed, C.; Lee, J. D.; Chance, R.; Sherwen, T.; Vaughan, A. R.; Stewart, J.; Edwards, P. M.; Bloss, W. J.; et al. Extensive field evidence for the release of HONO from the photolysis of nitrate aerosols. *Science Advances* **2023**, *9* (3), eadd6266. DOI: doi:10.1126/sciadv.add6266.
- (62) Ye, C.; Zhou, X.; Pu, D.; Stutz, J.; Festa, J.; Spolaor, M.; Tsai, C.; Cantrell, C.; Mauldin III, R. L.; Weinheimer, A.; et al. Tropospheric HONO distribution and chemistry in the southeastern US. *Atmos. Chem. Phys.* **2018**, *18* (12), 9107-9120. DOI: 10.5194/acp-18-9107-2018.
- (63) Jiang, Y.; Hoffmann, E. H.; Tilgner, A.; Aiyuk, M. B. E.; Andersen, S. T.; Wen, L.; van Pinxteren, M.; Shen, H.; Xue, L.; Wang, W.; et al. Insights Into NO_x and HONO Chemistry in the Tropical Marine Boundary Layer at Cape Verde During the MarParCloud Campaign. *Journal of Geophysical Research: Atmospheres* **2023**, *128* (16), e2023JD038865. DOI: <https://doi.org/10.1029/2023JD038865>.
- (64) Tsai, C.; Spolaor, M.; Colosimo, S. F.; Pikel'naya, O.; Cheung, R.; Williams, E.; Gilman, J. B.; Lerner, B. M.; Zamora, R. J.; Warneke, C.; et al. Nitrous acid formation in a snow-free wintertime polluted rural area. *Atmos. Chem. Phys.* **2018**, *18* (3), 1977-1996. DOI: 10.5194/acp-18-1977-2018.
- (65) Laufs, S.; Kleffmann, J. Investigations on HONO formation from photolysis of adsorbed HNO₃ on quartz glass surfaces. *Physical Chemistry Chemical Physics* **2016**, *18* (14), 9616-9625, 10.1039/C6CP00436A. DOI: 10.1039/C6CP00436A.
- (66) Chai, J.; Dibb, J. E.; Anderson, B. E.; Bekker, C.; Blum, D. E.; Heim, E.; Jordan, C. E.; Joyce, E. E.; Kaspari, J. H.; Munro, H.; et al. Isotopic constraints on wildfire derived

HONO. *Atmospheric Chemistry and Physics Discussion* **2021**. DOI: 10.5194/acp-2021-225.

(67) Romer, P. S.; Wooldridge, P. J.; Crouse, J. D.; Kim, M. J.; Wennberg, P. O.; Dibb, J. E.; Scheuer, E.; Blake, D. R.; Meinardi, S.; Brosius, A. L.; et al. Constraints on Aerosol Nitrate Photolysis as a Potential Source of HONO and NO_x. *Environ Sci Technol* **2018**, *52* (23), 13738-13746. DOI: 10.1021/acs.est.8b03861.

(68) Pusede, S. E.; VandenBoer, T. C.; Murphy, J. G.; Markovic, M. Z.; Young, C. J.; Veres, P. R.; Roberts, J. M.; Washenfelder, R. A.; Brown, S. S.; Ren, X.; et al. An Atmospheric Constraint on the NO₂ Dependence of Daytime Near-Surface Nitrous Acid (HONO). *Environmental Science & Technology* **2015**, *49* (21), 12774-12781. DOI: 10.1021/acs.est.5b02511.

(69) Yang, Y.; Li, X.; Zu, K.; Lian, C.; Chen, S.; Dong, H.; Feng, M.; Liu, H.; Liu, J.; Lu, K.; et al. Elucidating the effect of HONO on O₃ pollution by a case study in southwest China. *Sci Total Environ* **2021**, *756*, 144127. DOI: 10.1016/j.scitotenv.2020.144127.

(70) Liu, Y.; Lu, K.; Li, X.; Dong, H.; Tan, Z.; Wang, H.; Zou, Q.; Wu, Y.; Zeng, L.; Hu, M.; et al. A Comprehensive Model Test of the HONO Sources Constrained to Field Measurements at Rural North China Plain. *Environ Sci Technol* **2019**, *53* (7), 3517-3525. DOI: 10.1021/acs.est.8b06367.

(71) Ge, Y.; Shi, X.; Ma, Y.; Zhang, W.; Ren, X.; Zheng, J.; Zhang, Y. Seasonality of nitrous acid near an industry zone in the Yangtze River Delta region of China: Formation mechanisms and contribution to the atmospheric oxidation capacity. *Atmospheric Environment* **2021**, *254*. DOI: 10.1016/j.atmosenv.2021.118420.

(72) Shi, X.; Ge, Y.; Zheng, J.; Ma, Y.; Ren, X.; Zhang, Y. Budget of nitrous acid and its impacts on atmospheric oxidative capacity at an urban site in the central Yangtze River Delta region of China. *Atmospheric Environment* **2020**, *238*. DOI: 10.1016/j.atmosenv.2020.117725.

(73) Nie, W.; Ding, A. J.; Xie, Y. N.; Xu, Z.; Mao, H.; Kerminen, V. M.; Zheng, L. F.; Qi, X. M.; Huang, X.; Yang, X. Q.; et al. Influence of biomass burning plumes on HONO chemistry in eastern China. *Atmospheric Chemistry and Physics* **2015**, *15* (3), 1147-1159. DOI: 10.5194/acp-15-1147-2015.

(74) Peng, Q.; Palm, B. B.; Fredrickson, C. D.; Lee, B. H.; Hall, S. R.; Ullmann, K.; Weinheimer, A. J.; Levin, E.; DeMott, P.; Garofalo, L. A.; et al. Direct Constraints on Secondary HONO Production in Aged Wildfire Smoke From Airborne Measurements Over the Western US. *Geophysical Research Letters* **2022**, *49* (15), e2022GL098704. DOI: <https://doi.org/10.1029/2022GL098704>.

(75) Chai, J.; Miller, D. J.; Scheuer, E.; Dibb, J.; Selimovic, V.; Yokelson, R.; Zarzana, K. J.; Brown, S. S.; Koss, A. R.; Warneke, C.; et al. Isotopic characterization of nitrogen

oxides (NO_x), nitrous acid (HONO), and nitrate (pNO₃⁻) from laboratory biomass burning during FIREX. *Atmos. Meas. Tech.* **2019**, *12* (12), 6303-6317. DOI: 10.5194/amt-12-6303-2019.

(76) Scharko, N. K.; Berke, A. E.; Raff, J. D. Release of nitrous acid and nitrogen dioxide from nitrate photolysis in acidic aqueous solutions. *Environ Sci Technol* **2014**, *48* (20), 11991-12001. DOI: 10.1021/es503088x.

(77) Shi, X.; Nenes, A.; Xiao, Z.; Song, S.; Yu, H.; Shi, G.; Zhao, Q.; Chen, K.; Feng, Y.; Russell, A. G. High-Resolution Data Sets Unravel the Effects of Sources and Meteorological Conditions on Nitrate and Its Gas-Particle Partitioning. *Environ Sci Technol* **2019**, *53* (6), 3048-3057. DOI: 10.1021/acs.est.8b06524.

(78) Park, J. Y.; Lee, Y. N. Solubility and decomposition kinetics of nitrous acid in aqueous solution. *The Journal of Physical Chemistry* **1988**, *92* (22), 6294-6302. DOI: 10.1021/j100333a025.

(79) Mora Garcia, S. L.; Pandit, S.; Navea, J. G.; Grassian, V. H. Nitrous Acid (HONO) Formation from the Irradiation of Aqueous Nitrate Solutions in the Presence of Marine Chromophoric Dissolved Organic Matter: Comparison to Other Organic Photosensitizers. *ACS Earth and Space Chemistry* **2021**, *5* (11), 3056-3064. DOI: 10.1021/acsearthspacechem.1c00292.

(80) VandenBoer, T. C.; Markovic, M. Z.; Sanders, J. E.; Ren, X.; Pusede, S. E.; Browne, E. C.; Cohen, R. C.; Zhang, L.; Thomas, J.; Brune, W. H.; et al. Evidence for a nitrous acid (HONO) reservoir at the ground surface in Bakersfield, CA, during CalNex 2010. *Journal of Geophysical Research: Atmospheres* **2014**, *119* (14), 9093-9106. DOI: <https://doi.org/10.1002/2013JD020971>.

(81) Kleffmann, J.; Heland, J.; Kurtenbach, R.; Lörzer, J. C.; Wiesen, P. A new instrument (LOPAP) for the detection of nitrous acid (HONO). *Environ. Sci. Pollut. Res.* **2002**, *9*, 48-54.

(82) Heland, J.; Kleffmann, J.; Kurtenbach, R.; Wiesen, P. A New Instrument To Measure Gaseous Nitrous Acid (HONO) in the Atmosphere. *Environmental Science & Technology* **2001**, *35* (15), 3207-3212. DOI: 10.1021/es000303t.

(83) Kleffmann, J.; Lörzer, J. C.; Wiesen, P.; Kern, C.; Trick, S.; Volkamer, R.; Rodenas, M.; Wirtz, K. Intercomparison of the DOAS and LOPAP techniques for the detection of nitrous acid (HONO). *Atmospheric Environment* **2006**, *40* (20), 3640-3652. DOI: <https://doi.org/10.1016/j.atmosenv.2006.03.027>.

(84) Reed, C.; Brumby, C. A.; Crilley, L. R.; Kramer, L. J.; Bloss, W. J.; Seakins, P. W.; Lee, J. D.; Carpenter, L. J. HONO measurement by differential photolysis. *Atmos. Meas. Tech.* **2016**, *9* (6), 2483-2495. DOI: 10.5194/amt-9-2483-2016.

- (85) Crilley, L. R.; Kramer, L. J.; Ouyang, B.; Duan, J.; Zhang, W.; Tong, S.; Ge, M.; Tang, K.; Qin, M.; Xie, P.; et al. Intercomparison of nitrous acid (HONO) measurement techniques in a megacity (Beijing). *Atmospheric Measurement Techniques* **2019**, *12* (12), 6449-6463. DOI: 10.5194/amt-12-6449-2019.
- (86) Lewis, E. R. An examination of Köhler theory resulting in an accurate expression for the equilibrium radius ratio of a hygroscopic aerosol particle valid up to and including relative humidity 100%. *Journal of Geophysical Research* **2008**, *113* (D3). DOI: 10.1029/2007jd008590.
- (87) Nenes, A.; Pandis, S. N.; Pilinis, C. ISORROPIA: A New Thermodynamic Equilibrium Model for Multiphase Multicomponent Inorganic Aerosols. *Aquatic Geochemistry* **1998**, *4* (1), 123-152. DOI: 10.1023/A:1009604003981.
- (88) Fountoukis, C.; Nenes, A. ISORROPIA II: a computationally efficient thermodynamic equilibrium model for K^+ – Ca^{2+} – Mg^{2+} – NH_4^+ – Na^+ – SO_4^{2-} – NO_3^- – Cl^- – H_2O aerosols. *Atmos. Chem. Phys.* **2007**, *7* (17), 4639-4659. DOI: 10.5194/acp-7-4639-2007.
- (89) Guo, H.; Xu, L.; Bougiatioti, A.; Cerully, K. M.; Capps, S. L.; Hite Jr, J. R.; Carlton, A. G.; Lee, S. H.; Bergin, M. H.; Ng, N. L.; et al. Fine-particle water and pH in the southeastern United States. *Atmos. Chem. Phys.* **2015**, *15* (9), 5211-5228. DOI: 10.5194/acp-15-5211-2015.
- (90) Hennigan, C. J.; Izumi, J.; Sullivan, A. P.; Weber, R. J.; Nenes, A. A critical evaluation of proxy methods used to estimate the acidity of atmospheric particles. *Atmos. Chem. Phys.* **2015**, *15* (5), 2775-2790. DOI: 10.5194/acp-15-2775-2015.
- (91) Weber, R. J.; Guo, H.; Russell, A. G.; Nenes, A. High aerosol acidity despite declining atmospheric sulfate concentrations over the past 15 years. *Nature Geoscience* **2016**, *9* (4), 282-285. DOI: 10.1038/ngeo2665.
- (92) Guo, H.; Sullivan, A. P.; Campuzano-Jost, P.; Schroder, J. C.; Lopez-Hilfiker, F. D.; Dibb, J. E.; Jimenez, J. L.; Thornton, J. A.; Brown, S. S.; Nenes, A.; et al. Fine particle pH and the partitioning of nitric acid during winter in the northeastern United States. *Journal of Geophysical Research: Atmospheres* **2016**, *121* (17), 10,355-310,376, <https://doi.org/10.1002/2016JD025311>. DOI: <https://doi.org/10.1002/2016JD025311> (accessed 2021/08/26).
- (93) Zhang, Y.; Wang, Y.; Chen, G.; Smeltzer, C.; Crawford, J.; Olson, J.; Szykman, J.; Weinheimer, A. J.; Knapp, D. J.; Montzka, D. D.; et al. Large vertical gradient of reactive nitrogen oxides in the boundary layer: Modeling analysis of DISCOVER-AQ 2011 observations. *Journal of Geophysical Research: Atmospheres* **2016**, *121* (4), 1922-1934. DOI: 10.1002/2015jd024203.

- (94) Wang, Y.; Logan, J. A.; Jacob, D. J. Global simulation of tropospheric O₃-NO_x-hydrocarbon chemistry: 2. Model evaluation and global ozone budget. *Journal of Geophysical Research: Atmospheres* **1998**, *103* (D9), 10727-10755. DOI: 10.1029/98jd00157.
- (95) Kramer, L. J.; Crilley, L. R.; Adams, T. J.; Ball, S. M.; Pope, F. D.; Bloss, W. J. Nitrous acid (HONO) emissions under real-world driving conditions from vehicles in a UK road tunnel. *Atmospheric Chemistry and Physics* **2020**, *20* (9), 5231-5248. DOI: 10.5194/acp-20-5231-2020.
- (96) Kleffmann, J.; Becker, K. H.; Wiesen, P. Heterogeneous NO₂ conversion processes on acid surfaces: possible atmospheric implications. *Atmospheric Environment* **1998**, *32* (16), 2721-2729. DOI: [https://doi.org/10.1016/S1352-2310\(98\)00065-X](https://doi.org/10.1016/S1352-2310(98)00065-X).
- (97) Wang, Y.; Wang, J.; Wang, Y.; Zhang, Y.; Woodward-Massey, R.; Zhang, C.; Kuang, Y.; Zhu, J.; Shang, J.; Li, X.; et al. Experimental and kinetic model evaluation of HONO production from surface nitrate photolysis. *Atmospheric Environment* **2023**, *296*, 119568. DOI: <https://doi.org/10.1016/j.atmosenv.2022.119568>.
- (98) Song, M.; Zhao, X.; Liu, P.; Mu, J.; He, G.; Zhang, C.; Tong, S.; Xue, C.; Zhao, X.; Ge, M.; et al. Atmospheric NO_x oxidation as major sources for nitrous acid (HONO). *npj Climate and Atmospheric Science* **2023**, *6* (1), 30. DOI: 10.1038/s41612-023-00357-8.
- (99) Gu, R.; Zheng, P.; Chen, T.; Dong, C.; Wang, Y. n.; Liu, Y.; Liu, Y.; Luo, Y.; Han, G.; Wang, X.; et al. Atmospheric nitrous acid (HONO) at a rural coastal site in North China: Seasonal variations and effects of biomass burning. *Atmospheric Environment* **2020**, *229*. DOI: 10.1016/j.atmosenv.2020.117429.
- (100) Yang, J.; Shen, H.; Guo, M.-Z.; Zhao, M.; Jiang, Y.; Chen, T.; Liu, Y.; Li, H.; Zhu, Y.; Meng, H.; et al. Strong marine-derived nitrous acid (HONO) production observed in the coastal atmosphere of northern China. *Atmospheric Environment* **2021**, *244*. DOI: 10.1016/j.atmosenv.2020.117948.
- (101) Cui, L.; Li, R.; Fu, H.; Li, Q.; Zhang, L.; George, C.; Chen, J. Formation features of nitrous acid in the offshore area of the East China Sea. *Sci Total Environ* **2019**, *682*, 138-150. DOI: 10.1016/j.scitotenv.2019.05.004.
- (102) Lee, J. D.; Whalley, L. K.; Heard, D. E.; Stone, D.; Dunmore, R. E.; Hamilton, J. F.; Young, D. E.; Allan, J. D.; Laufs, S.; Kleffmann, J. Detailed budget analysis of HONO in central London reveals a missing daytime source. *Atmospheric Chemistry and Physics* **2016**, *16* (5), 2747-2764. DOI: 10.5194/acp-16-2747-2016.
- (103) Zha, Q.; Xue, L.; Wang, T.; Xu, Z.; Yeung, C.; Louie, P. K. K.; Luk, C. W. Y. Large conversion rates of NO₂ to HNO₂ observed in air masses from the South China Sea: Evidence of strong production at sea surface? *Geophysical Research Letters* **2014**, *41* (21), 7710-7715. DOI: <https://doi.org/10.1002/2014GL061429>.

- (104) Chen, J.; Li, C.; Ristovski, Z.; Milic, A.; Gu, Y.; Islam, M. S.; Wang, S.; Hao, J.; Zhang, H.; He, C.; et al. A review of biomass burning: Emissions and impacts on air quality, health and climate in China. *Sci Total Environ* **2017**, *579*, 1000-1034. DOI: 10.1016/j.scitotenv.2016.11.025.
- (105) Yuan, B.; Liu, Y.; Shao, M.; Lu, S.; Streets, D. G. Biomass Burning Contributions to Ambient VOCs Species at a Receptor Site in the Pearl River Delta (PRD), China. *Environmental Science & Technology* **2010**, *44* (12), 4577-4582. DOI: 10.1021/es1003389.
- (106) Juncosa Calahorrano, J. F.; Lindaas, J.; O'Dell, K.; Palm, B. B.; Peng, Q.; Flocke, F.; Pollack, I. B.; Garofalo, L. A.; Farmer, D. K.; Pierce, J. R.; et al. Daytime Oxidized Reactive Nitrogen Partitioning in Western U.S. Wildfire Smoke Plumes. *Journal of Geophysical Research: Atmospheres* **2021**, *126* (4). DOI: 10.1029/2020jd033484.
- (107) Hughes, D. D.; Christiansen, M. B.; Milani, A.; Vermeuel, M. P.; Novak, G. A.; Alwe, H. D.; Dickens, A. F.; Pierce, R. B.; Millet, D. B.; Bertram, T. H.; et al. PM_{2.5} chemistry, organosulfates, and secondary organic aerosol during the 2017 Lake Michigan Ozone Study. *Atmospheric Environment* **2021**, *244*. DOI: 10.1016/j.atmosenv.2020.117939.
- (108) Lindaas, J.; Pollack, I. B.; Garofalo, L. A.; Pothier, M. A.; Farmer, D. K.; Kreidenweis, S. M.; Campos, T. L.; Flocke, F.; Weinheimer, A. J.; Montzka, D. D.; et al. Emissions of Reactive Nitrogen From Western U.S. Wildfires During Summer 2018. *Journal of Geophysical Research: Atmospheres* **2021**, *126* (2). DOI: 10.1029/2020jd032657.
- (109) Peng, Q.; Palm, B. B.; Melander, K. E.; Lee, B. H.; Hall, S. R.; Ullmann, K.; Campos, T.; Weinheimer, A. J.; Apel, E. C.; Hornbrook, R. S.; et al. HONO Emissions from Western U.S. Wildfires Provide Dominant Radical Source in Fresh Wildfire Smoke. *Environ Sci Technol* **2020**. DOI: 10.1021/acs.est.0c00126.
- (110) Xu, R.; Li, X.; Dong, H.; Wu, Z.; Chen, S.; Xin, F.; Gao, J.; Guo, S.; Hu, M.; Li, D.; et al. Measurement of gaseous and particulate formaldehyde in the Yangtze River Delta, China. *Atmospheric Environment* **2019**, *224*, 117114. DOI: 10.1016/j.atmosenv.2019.117114.
- (111) Brock, C. A.; Cozic, J.; Bahreini, R.; Froyd, K. D.; Middlebrook, A. M.; McComiskey, A.; Brioude, J.; Cooper, O. R.; Stohl, A.; Aikin, K. C.; et al. Characteristics, sources, and transport of aerosols measured in spring 2008 during the aerosol, radiation, and cloud processes affecting Arctic Climate (ARCPAC) Project. *Atmospheric Chemistry and Physics* **2011**, *11* (6), 2423-2453. DOI: 10.5194/acp-11-2423-2011.
- (112) Pandit, S.; Grassian, V. H. Gas-Phase Nitrous Acid (HONO) Is Controlled by Surface Interactions of Adsorbed Nitrite (NO₂⁻) on Common Indoor Material Surfaces.

Environmental Science & Technology **2022**, *56* (17), 12045-12054. DOI: 10.1021/acs.est.2c02042.

(113) Riordan, E.; Minogue, N.; Healy, D.; O'Driscoll, P.; Sodeau, J. R. Spectroscopic and Optimization Modeling Study of Nitrous Acid in Aqueous Solution. *The Journal of Physical Chemistry A* **2005**, *109* (5), 779-786. DOI: 10.1021/jp040269v.

(114) Anastasio, C.; Chu, L. Photochemistry of Nitrous Acid (HONO) and Nitrous Acidium Ion (H₂ONO⁺) in Aqueous Solution and Ice. *Environmental Science & Technology* **2009**, *43* (4), 1108-1114. DOI: 10.1021/es802579a.

(115) Zhang, W.; Tong, S.; Jia, C.; Wang, L.; Liu, B.; Tang, G.; Ji, D.; Hu, B.; Liu, Z.; Li, W.; et al. Different HONO Sources for Three Layers at the Urban Area of Beijing. *Environ Sci Technol* **2020**, *54* (20), 12870-12880. DOI: 10.1021/acs.est.0c02146.

(116) Jiang, Y.; Xue, L.; Shen, H.; Dong, C.; Xiao, Z.; Wang, W. Dominant Processes of HONO Derived from Multiple Field Observations in Contrasting Environments. *Environmental Science & Technology Letters* **2022**, *9* (4), 258-264. DOI: 10.1021/acs.estlett.2c00004.

(117) Ye, C.; Zhou, X.; Pu, D.; Stutz, J.; Festa, J.; Spolaor, M.; Tsai, C.; Cantrell, C.; Mauldin, R. L., 3rd; Campos, T.; et al. Rapid cycling of reactive nitrogen in the marine boundary layer. *Nature* **2016**, *532* (7600), 489-491. DOI: 10.1038/nature17195.

(118) Ramazan, K. A.; Wingen, L. M.; Miller, Y.; Chaban, G. M.; Gerber, R. B.; Xantheas, S. S.; Finlayson-Pitts, B. J. New Experimental and Theoretical Approach to the Heterogeneous Hydrolysis of NO₂: Key Role of Molecular Nitric Acid and Its Complexes. *The Journal of Physical Chemistry A* **2006**, *110* (21), 6886-6897. DOI: 10.1021/jp056426n.

(119) Zhou, X.; Gao, H.; He, Y.; Huang, G.; Bertman, S. B.; Civerolo, K.; Schwab, J. Nitric acid photolysis on surfaces in low-NO_x environments: Significant atmospheric implications. *Geophysical Research Letters* **2003**, *30* (23). DOI: 10.1029/2003GL018620 (accessed 2020/07/23).

(120) Wong, K. W.; Tsai, C.; Lefer, B.; Grossberg, N.; Stutz, J. Modeling of daytime HONO vertical gradients during SHARP 2009. *Atmospheric Chemistry and Physics* **2013**, *13* (7), 3587-3601. DOI: 10.5194/acp-13-3587-2013.

(121) Gall, E. T.; Griffin, R. J.; Steiner, A. L.; Dibb, J.; Scheuer, E.; Gong, L.; Rutter, A. P.; Cevik, B. K.; Kim, S.; Lefer, B.; et al. Evaluation of nitrous acid sources and sinks in urban outflow. *Atmospheric Environment* **2016**, *127*, 272-282. DOI: 10.1016/j.atmosenv.2015.12.044.

(122) Zhang, L.; Wang, T.; Zhang, Q.; Zheng, J.; Xu, Z.; Lv, M. Potential sources of nitrous acid (HONO) and their impacts on ozone: A WRF-Chem study in a polluted subtropical

region. *Journal of Geophysical Research: Atmospheres* **2016**, *121* (7), 3645-3662. DOI: 10.1002/2015jd024468.

(123) Bao, F.; Li, M.; Zhang, Y.; Chen, C.; Zhao, J. Photochemical Aging of Beijing Urban PM_{2.5}: HONO Production. *Environ Sci Technol* **2018**, *52* (11), 6309-6316. DOI: 10.1021/acs.est.8b00538.

(124) Liu, J.; Liu, Z.; Ma, Z.; Yang, S.; Yao, D.; Zhao, S.; Hu, B.; Tang, G.; Sun, J.; Cheng, M.; et al. Detailed budget analysis of HONO in Beijing, China: Implication on atmosphere oxidation capacity in polluted megacity. *Atmospheric Environment* **2021**, *244*. DOI: 10.1016/j.atmosenv.2020.117957.

(125) Dyson, J. E.; Boustead, G. A.; Fleming, L. T.; Blitz, M.; Stone, D.; Arnold, S. R.; Whalley, L. K.; Heard, D. E. Production of HONO from NO₂ uptake on illuminated TiO₂ aerosol particles and following the illumination of mixed TiO₂ / ammonium nitrate particles. *Atmos. Chem. Phys.* **2021**, *21* (7), 5755-5775. DOI: 10.5194/acp-21-5755-2021.

(126) Reed, C.; Evans, M. J.; Crilley, L. R.; Bloss, W. J.; Sherwen, T.; Read, K. A.; Lee, J. D.; Carpenter, L. J. Evidence for renoxification in the tropical marine boundary layer. *Atmos. Chem. Phys.* **2017**, *17* (6), 4081-4092. DOI: 10.5194/acp-17-4081-2017.

(127) Kasibhatla, P.; Sherwen, T.; Evans, M. J.; Carpenter, L. J.; Reed, C.; Alexander, B.; Chen, Q.; Sulprizio, M. P.; Lee, J. D.; Read, K. A.; et al. Global impact of nitrate photolysis in sea-salt aerosol on NO_x, OH, and O₃ in the marine boundary layer. *Atmospheric Chemistry and Physics* **2018**, *18* (15), 11185-11203. DOI: 10.5194/acp-18-11185-2018.

(128) Ha, P. T. M.; Kanaya, Y.; Taketani, F.; Andrés Hernández, M. D.; Schreiner, B.; Pfeilsticker, K.; Sudo, K. Implementation of HONO into the chemistry–climate model CHASER (V4.0): roles in tropospheric chemistry. *Geosci. Model Dev.* **2023**, *16* (3), 927-960. DOI: 10.5194/gmd-16-927-2023.

(129) Crilley, L. R.; Kramer, L. J.; Pope, F. D.; Reed, C.; Lee, J. D.; Carpenter, L. J.; Hollis, L. D. J.; Ball, S. M.; Bloss, W. J. Is the ocean surface a source of nitrous acid (HONO) in the marine boundary layer? *Atmos. Chem. Phys.* **2021**, *21* (24), 18213-18225. DOI: 10.5194/acp-21-18213-2021.

(130) Yin, H.; Lu, X.; Sun, Y.; Li, K.; Gao, M.; Zheng, B.; Liu, C. Unprecedented decline in summertime surface ozone over eastern China in 2020 comparably attributable to anthropogenic emission reductions and meteorology. *Environmental Research Letters* **2021**, *16* (12), 124069. DOI: 10.1088/1748-9326/ac3e22.

(131) Xu, J.; Huang, X.; Wang, N.; Li, Y.; Ding, A. Understanding ozone pollution in the Yangtze River Delta of eastern China from the perspective of diurnal cycles. *Science of The Total Environment* **2021**, *752*, 141928. DOI: <https://doi.org/10.1016/j.scitotenv.2020.141928>.

- (132) Li, K.; Jacob, D. J.; Shen, L.; Lu, X.; De Smedt, I.; Liao, H. Increases in surface ozone pollution in China from 2013 to 2019: anthropogenic and meteorological influences. *Atmos. Chem. Phys.* **2020**, *20* (19), 11423-11433. DOI: 10.5194/acp-20-11423-2020.
- (133) Levy, J. I.; Carrothers, T. J.; Tuomisto, J. T.; Hammitt, J. K.; Evans, J. S. Assessing the public health benefits of reduced ozone concentrations. *Environmental health perspectives* **2001**, *109* (12), 1215-1226.
- (134) Nuvolone, D.; Petri, D.; Voller, F. The effects of ozone on human health. *Environmental Science and Pollution Research* **2018**, *25* (9), 8074-8088.
- (135) Finlayson, B. J.; Pitts, J. N. Photochemistry of the Polluted Troposphere. *Science* **1976**, *192* (4235), 111-119. DOI: doi:10.1126/science.192.4235.111.
- (136) Wang, Y.; Jacob, D. J.; Logan, J. A. Global simulation of tropospheric O₃-NO_x-hydrocarbon chemistry: 1. Model formulation. **1998**.
- (137) Logan, J. A. Nitrogen oxides in the troposphere: Global and regional budgets. *Journal of Geophysical Research: Oceans* **1983**, *88* (C15), 10785-10807, <https://doi.org/10.1029/JC088iC15p10785>. DOI: <https://doi.org/10.1029/JC088iC15p10785> (accessed 2023/01/19).
- (138) Felix, J. D.; Elliott, E. M. Isotopic composition of passively collected nitrogen dioxide emissions: Vehicle, soil and livestock source signatures. *Atmospheric Environment* **2014**, *92*, 359-366.
- (139) Dovrou, E.; Bates, K. H.; Moch, J. M.; Mickley, L. J.; Jacob, D. J.; Keutsch, F. N. Catalytic role of formaldehyde in particulate matter formation. *Proceedings of the National Academy of Sciences* **2022**, *119* (6), e2113265119. DOI: doi:10.1073/pnas.2113265119.
- (140) Shim, C.; Wang, Y.; Choi, Y.; Palmer, P. I.; Abbot, D. S.; Chance, K. Constraining global isoprene emissions with Global Ozone Monitoring Experiment (GOME) formaldehyde column measurements. *Journal of Geophysical Research: Atmospheres* **2005**, *110* (D24).
- (141) Li, D.; Wang, S.; Xue, R.; Zhu, J.; Zhang, S.; Sun, Z.; Zhou, B. OMI-observed HCHO in Shanghai, China, during 2010 - 2019 and ozone sensitivity inferred by an improved HCHO/NO₂ ratio. *Atmos. Chem. Phys.* **2021**, *21* (20), 15447-15460. DOI: 10.5194/acp-21-15447-2021.
- (142) Balamurugan, V.; Chen, J.; Qu, Z.; Bi, X.; Gensheimer, J.; Shekhar, A.; Bhattacharjee, S.; Keutsch, F. N. Tropospheric NO₂ and O₃ Response to COVID-19 Lockdown Restrictions at the National and Urban Scales in Germany. *Journal of Geophysical Research: Atmospheres* **2021**, *126* (19), e2021JD035440. DOI: <https://doi.org/10.1029/2021JD035440>.

- (143) Wang, H. J. R.; Damadeo, R.; Flittner, D.; Kramarova, N.; Taha, G.; Davis, S.; Thompson, A. M.; Strahan, S.; Wang, Y.; Froidevaux, L.; et al. Validation of SAGE III/ISS Solar Occultation Ozone Products With Correlative Satellite and Ground-Based Measurements. *Journal of Geophysical Research: Atmospheres* **2020**, *125* (11), e2020JD032430. DOI: <https://doi.org/10.1029/2020JD032430>.
- (144) Zhang, Y.; Wang, Y.; Crawford, J.; Cheng, Y.; Li, J. Improve observation-based ground-level ozone spatial distribution by compositing satellite and surface observations: A simulation experiment. *Atmospheric Environment* **2018**, *180*, 226-233. DOI: <https://doi.org/10.1016/j.atmosenv.2018.02.044>.
- (145) Lamsal, L. N.; Martin, R. V.; van Donkelaar, A.; Celarier, E. A.; Bucsela, E. J.; Boersma, K. F.; Dirksen, R.; Luo, C.; Wang, Y. Indirect validation of tropospheric nitrogen dioxide retrieved from the OMI satellite instrument: Insight into the seasonal variation of nitrogen oxides at northern midlatitudes. *Journal of Geophysical Research: Atmospheres* **2010**, *115* (D5). DOI: <https://doi.org/10.1029/2009JD013351>.
- (146) Zeng, T.; Wang, Y.; Yoshida, Y.; Tian, D.; Russell, A. G.; Barnard, W. R. Impacts of prescribed fires on air quality over the Southeastern United States in spring based on modeling and ground/satellite measurements. *Environ Sci Technol* **2008**, *42* (22), 8401-8406. DOI: [10.1021/es800363d](https://doi.org/10.1021/es800363d) From NLM.
- (147) Levelt, P. F.; Hilsenrath, E.; Leppelmeier, G. W.; Oord, G. H. J. v. d.; Bhartia, P. K.; Tamminen, J.; Haan, J. F. d.; Veefkind, J. P. Science objectives of the ozone monitoring instrument. *IEEE Transactions on Geoscience and Remote Sensing* **2006**, *44* (5), 1199-1208. DOI: [10.1109/TGRS.2006.872336](https://doi.org/10.1109/TGRS.2006.872336).
- (148) Veefkind, J. P.; Aben, I.; McMullan, K.; Förster, H.; de Vries, J.; Otter, G.; Claas, J.; Eskes, H. J.; de Haan, J. F.; Kleipool, Q.; et al. TROPOMI on the ESA Sentinel-5 Precursor: A GMES mission for global observations of the atmospheric composition for climate, air quality and ozone layer applications. *Remote Sensing of Environment* **2012**, *120*, 70-83. DOI: <https://doi.org/10.1016/j.rse.2011.09.027>.
- (149) Smedt, I. D.; Geffen, J. v.; Richter, A.; Beirle, S.; Yu, H.; Vlietinck, J.; Roozendael, M. V.; A, R. v. d.; Lorente, A.; Scanlon, T.; et al. *Product User Guide for HCHO*; BIRA-IASB, KNMI, MPI-C, IUP-B, WUR, NPL, 2017. https://www.temis.nl/qa4ecv/hcho/QA4ECV_HCHO_PSD_v1.0.pdf.
- (150) Krotkov, N. A.; Lamsal, L. N.; Marchenko, S. V.; Swartz, W. H. *OMNO2 README Document*

Data	Product	Version	Year
		4.0;	2019.

https://aura.gesdisc.eosdis.nasa.gov/data/Aura_OMI_Level2/OMNO2.003/doc/README.OMNO2.pdf.
- (151) Pu, D.; Zhu, L.; De Smedt, I.; Li, X.; Sun, W.; Wang, D.; Liu, S.; Li, J.; Shu, L.; Chen, Y.; et al. Response of Anthropogenic Volatile Organic Compound Emissions to Urbanization in Asia Probed With TROPOMI and VIIRS Satellite Observations.

Geophysical Research Letters **2022**, *49* (18), e2022GL099470, <https://doi.org/10.1029/2022GL099470>. DOI: <https://doi.org/10.1029/2022GL099470> (accessed 2022/09/22).

(152) Zhang, R.; Zhang, Y.; Lin, H.; Feng, X.; Fu, T.-M.; Wang, Y. NO_x Emission Reduction and Recovery during COVID-19 in East China. *Atmosphere* **2020**, *11* (4), 433.

(153) Krotkov, N. A.; McLinden, C. A.; Li, C.; Lamsal, L. N.; Celarier, E. A.; Marchenko, S. V.; Swartz, W. H.; Bucsela, E. J.; Joiner, J.; Duncan, B. N.; et al. Aura OMI observations of regional SO₂ and NO₂ pollution changes from 2005 to 2015. *Atmos. Chem. Phys.* **2016**, *16* (7), 4605-4629. DOI: 10.5194/acp-16-4605-2016.

(154) DiMaria, C. A.; Jones, D. B. A.; Worden, H.; Bloom, A. A.; Bowman, K.; Stavrou, T.; Miyazaki, K.; Worden, J.; Guenther, A.; Sarkar, C.; et al. Optimizing the Isoprene Emission Model MEGAN With Satellite and Ground-Based Observational Constraints. *Journal of Geophysical Research: Atmospheres* **2023**, *128* (4), e2022JD037822. DOI: <https://doi.org/10.1029/2022JD037822>.

(155) González Abad, G.; Liu, X.; Chance, K.; Wang, H.; Kurosu, T. P.; Suleiman, R. Updated Smithsonian Astrophysical Observatory Ozone Monitoring Instrument (SAO OMI) formaldehyde retrieval. *Atmos. Meas. Tech.* **2015**, *8* (1), 19-32. DOI: 10.5194/amt-8-19-2015.

(156) González Abad, G.; Vasilkov, A.; Seftor, C.; Liu, X.; Chance, K. Smithsonian Astrophysical Observatory Ozone Mapping and Profiler Suite (SAO OMPS) formaldehyde retrieval. *Atmos. Meas. Tech.* **2016**, *9* (7), 2797-2812. DOI: 10.5194/amt-9-2797-2016.

(157) Souri, A. H.; Johnson, M. S.; Wolfe, G. M.; Crawford, J. H.; Fried, A.; Wisthaler, A.; Brune, W. H.; Blake, D. R.; Weinheimer, A. J.; Verhoelst, T.; et al. Characterization of Errors in Satellite-based HCHO / NO₂ Tropospheric Column Ratios with Respect to Chemistry, Column to PBL Translation, Spatial Representation, and Retrieval Uncertainties. *Atmos. Chem. Phys. Discuss.* **2022**, *2022*, 1-43. DOI: 10.5194/acp-2022-410.

(158) Boersma, K. F.; Eskes, H. J.; Brinksma, E. J. Error analysis for tropospheric NO₂ retrieval from space. *Journal of Geophysical Research: Atmospheres* **2004**, *109* (D4). DOI: <https://doi.org/10.1029/2003JD003962>.

(159) Lin, J. T.; Martin, R. V.; Boersma, K. F.; Sneep, M.; Stammes, P.; Spurr, R.; Wang, P.; Van Roozendaal, M.; Clémer, K.; Irie, H. Retrieving tropospheric nitrogen dioxide from the Ozone Monitoring Instrument: effects of aerosols, surface reflectance anisotropy, and vertical profile of nitrogen dioxide. *Atmos. Chem. Phys.* **2014**, *14* (3), 1441-1461. DOI: 10.5194/acp-14-1441-2014.

- (160) Wang, P.; Holloway, T.; Bindl, M.; Harkey, M.; De Smedt, I. Ambient Formaldehyde over the United States from Ground-Based (AQS) and Satellite (OMI) Observations. *Remote Sensing* **2022**, *14* (9). DOI: 10.3390/rs14092191.
- (161) Hönninger, G.; von Friedeburg, C.; Platt, U. Multi axis differential optical absorption spectroscopy (MAX-DOAS). *Atmos. Chem. Phys.* **2004**, *4* (1), 231-254. DOI: 10.5194/acp-4-231-2004.
- (162) Frieß, U.; Klein Baltink, H.; Beirle, S.; Clémer, K.; Hendrick, F.; Henzing, B.; Irie, H.; de Leeuw, G.; Li, A.; Moerman, M. M.; et al. Intercomparison of aerosol extinction profiles retrieved from MAX-DOAS measurements. *Atmospheric Measurement Techniques* **2016**, *9* (7), 3205-3222. DOI: 10.5194/amt-9-3205-2016.
- (163) Irie, H.; Takashima, H.; Kanaya, Y.; Boersma, K. F.; Gast, L.; Wittrock, F.; Brunner, D.; Zhou, Y.; Van Roozendaal, M. Eight-component retrievals from ground-based MAX-DOAS observations. *Atmos. Meas. Tech.* **2011**, *4* (6), 1027-1044. DOI: 10.5194/amt-4-1027-2011.
- (164) Ma, J. Z.; Beirle, S.; Jin, J. L.; Shaiganfar, R.; Yan, P.; Wagner, T. Tropospheric NO₂ vertical column densities over Beijing: results of the first three years of ground-based MAX-DOAS measurements (2008–2011) and satellite validation. *Atmos. Chem. Phys.* **2013**, *13* (3), 1547-1567. DOI: 10.5194/acp-13-1547-2013.
- (165) Wang, Y.; Apituley, A.; Bais, A.; Beirle, S.; Benavent, N.; Borovski, A.; Bruchkouski, I.; Chan, K. L.; Donner, S.; Drosoglou, T.; et al. Inter-comparison of MAX-DOAS measurements of tropospheric HONO slant column densities and vertical profiles during the CINDI-2 campaign. *Atmos. Meas. Tech.* **2020**, *13* (9), 5087-5116. DOI: 10.5194/amt-13-5087-2020.
- (166) De Smedt, I.; Pinardi, G.; Vigouroux, C.; Compernelle, S.; Bais, A.; Benavent, N.; Boersma, F.; Chan, K. L.; Donner, S.; Eichmann, K. U.; et al. Comparative assessment of TROPOMI and OMI formaldehyde observations and validation against MAX-DOAS network column measurements. *Atmos. Chem. Phys.* **2021**, *21* (16), 12561-12593. DOI: 10.5194/acp-21-12561-2021.
- (167) Verhoelst, T.; Compernelle, S.; Pinardi, G.; Lambert, J. C.; Eskes, H. J.; Eichmann, K. U.; Fjæraa, A. M.; Granville, J.; Niemeijer, S.; Cede, A.; et al. Ground-based validation of the Copernicus Sentinel-5P TROPOMI NO₂ measurements with the NDACC ZSL-DOAS, MAX-DOAS and Pandonia global networks. *Atmos. Meas. Tech.* **2021**, *14* (1), 481-510. DOI: 10.5194/amt-14-481-2021.
- (168) Zhang, C.; Liu, C.; Chan, K. L.; Hu, Q.; Liu, H.; Li, B.; Xing, C.; Tan, W.; Zhou, H.; Si, F.; et al. First observation of tropospheric nitrogen dioxide from the Environmental Trace Gases Monitoring Instrument onboard the GaoFen-5 satellite. *Light: Science & Applications* **2020**, *9* (1), 66. DOI: 10.1038/s41377-020-0306-z.

- (169) Xia, C.; Liu, C.; Cai, Z.; Duan, X.; Hu, Q.; Zhao, F.; Liu, H.; Ji, X.; Zhang, C.; Liu, Y. Improved Anthropogenic SO₂ Retrieval from High-Spatial-Resolution Satellite and its Application during the COVID-19 Pandemic. *Environmental Science & Technology* **2021**, *55* (17), 11538-11548. DOI: 10.1021/acs.est.1c01970.
- (170) Ialongo, I.; Herman, J.; Krotkov, N.; Lamsal, L.; Boersma, K. F.; Hovila, J.; Tamminen, J. Comparison of OMI NO₂ observations and their seasonal and weekly cycles with ground-based measurements in Helsinki. *Atmos. Meas. Tech.* **2016**, *9* (10), 5203-5212. DOI: 10.5194/amt-9-5203-2016.
- (171) Jin, J.; Ma, J.; Lin, W.; Zhao, H.; Shaiganfar, R.; Beirle, S.; Wagner, T. MAX-DOAS measurements and satellite validation of tropospheric NO₂ and SO₂ vertical column densities at a rural site of North China. *Atmospheric Environment* **2016**, *133*, 12-25. DOI: <https://doi.org/10.1016/j.atmosenv.2016.03.031>.
- (172) Irie, H.; Hoque, H. M. S.; Damiani, A.; Okamoto, H.; Fatmi, A. M.; Khatri, P.; Takamura, T.; Jarupongsakul, T. Simultaneous observations by sky radiometer and MAX-DOAS for characterization of biomass burning plumes in central Thailand in January–April 2016. *Atmos. Meas. Tech.* **2019**, *12* (1), 599-606. DOI: 10.5194/amt-12-599-2019.
- (173) Lin, H.; Xing, C.; Hong, Q.; Liu, C.; Ji, X.; Liu, T.; Lin, J.; Lu, C.; Tan, W.; Li, Q.; et al. Diagnosis of Ozone Formation Sensitivities in Different Height Layers via MAX-DOAS Observations in Guangzhou. *Journal of Geophysical Research: Atmospheres* **2022**, *127* (15), e2022JD036803, <https://doi.org/10.1029/2022JD036803>. DOI: <https://doi.org/10.1029/2022JD036803> (accessed 2023/04/19).
- (174) Hendrick, F.; Müller, J. F.; Clémer, K.; Wang, P.; De Mazière, M.; Fayt, C.; Gielen, C.; Hermans, C.; Ma, J. Z.; Pinardi, G.; et al. Four years of ground-based MAX-DOAS observations of HONO and NO₂ in the Beijing area. *Atmospheric Chemistry and Physics* **2014**, *14* (2), 765-781. DOI: 10.5194/acp-14-765-2014.
- (175) Liu, C.; Gao, M.; Hu, Q.; Brasseur, G. P.; Carmichael, G. R. Stereoscopic Monitoring: A Promising Strategy to Advance Diagnostic and Prediction of Air Pollution. *Bulletin of the American Meteorological Society* **2021**, *102* (4), E730-E737. DOI: <https://doi.org/10.1175/BAMS-D-20-0217.1>.
- (176) Javed, Z.; Wang, Y.; Xie, M.; Tanvir, A.; Rehman, A.; Ji, X.; Xing, C.; Shakoor, A.; Liu, C. Investigating the Impacts of the COVID-19 Lockdown on Trace Gases Using Ground-Based MAX-DOAS Observations in Nanjing, China. *Remote Sensing* **2020**, *12* (23), 3939.
- (177) Javed, Z.; Tanvir, A.; Bilal, M.; Su, W.; Xia, C.; Rehman, A.; Zhang, Y.; Sandhu, O.; Xing, C.; Ji, X.; et al. Recommendations for HCHO and SO₂ Retrieval Settings from MAX-DOAS Observations under Different Meteorological Conditions. *Remote Sensing* **2021**, *13* (12), 2244.

- (178) Wang, Y.; Pukīte, J.; Wagner, T.; Donner, S.; Beirle, S.; Hilboll, A.; Vrekoussis, M.; Richter, A.; Apituley, A.; Pipers, A.; et al. Vertical Profiles of Tropospheric Ozone From MAX-DOAS Measurements During the CINDI-2 Campaign: Part 1—Development of a New Retrieval Algorithm. *Journal of Geophysical Research: Atmospheres* **2018**, *123* (18), 10,637-610,670. DOI: <https://doi.org/10.1029/2018JD028647> (accessed 2023/10/05).
- (179) Xing, C.; Liu, C.; Wang, S.; Chan, K. L.; Gao, Y.; Huang, X.; Su, W.; Zhang, C.; Dong, Y.; Fan, G.; et al. Observations of the vertical distributions of summertime atmospheric pollutants and the corresponding ozone production in Shanghai, China. *Atmos. Chem. Phys.* **2017**, *17* (23), 14275-14289. DOI: 10.5194/acp-17-14275-2017.
- (180) Zheng, X.; Javed, Z.; Liu, C.; Tanvir, A.; Sandhu, O.; Liu, H.; Ji, X.; Xing, C.; Lin, H.; Du, D. MAX-DOAS and In-situ measurements of aerosols and trace gases over Dongying, China: Insight into Ozone formation sensitivity based on Secondary HCHO. *Journal of Environmental Sciences* **2022**. DOI: <https://doi.org/10.1016/j.jes.2022.09.014>.
- (181) Danckaert, T.; Fayt, C.; Van Roozendael, M.; De Smedt, I.; Letocart, V.; Merlaud, A.; Pinardi, G. QDOAS Software user manual. **2012**.
- (182) Rodgers, C. D. *Inverse Methods for Atmospheric Sounding*; 2000. DOI: 10.1142/3171.
- (183) Song, Y.; Xing, C.; Liu, C.; Lin, J.; Wu, H.; Liu, T.; Lin, H.; Zhang, C.; Tan, W.; Ji, X.; et al. Evaluation of transport processes over North China Plain and Yangtze River Delta using MAX-DOAS observations. *Atmos. Chem. Phys.* **2023**, *23* (3), 1803-1824. DOI: 10.5194/acp-23-1803-2023.
- (184) Krotkov, N. A.; Lamsal, L. N.; Marchenko, S. V.; Bucsela, E. J.; Swartz, W. H.; Joiner, J.; team, t. O. c. OMI/Aura Nitrogen Dioxide (NO₂) Total and Tropospheric Column 1-orbit L2 Swath 13x24 km V003. Goddard Earth Sciences Data and Information Services Center (GES DISC): Greenbelt, MD, USA, 2019.
- (185) Boersma, K. F.; Eskes, H. J.; Dirksen, R. J.; van der A, R. J.; Veefkind, J. P.; Stammes, P.; Huijnen, V.; Kleipool, Q. L.; Sneep, M.; Claas, J.; et al. An improved tropospheric NO₂ column retrieval algorithm for the Ozone Monitoring Instrument. *Atmos. Meas. Tech.* **2011**, *4* (9), 1905-1928. DOI: 10.5194/amt-4-1905-2011.
- (186) van Geffen, J.; Eskes, H.; Boersma, K. F.; Veefkind, J. P. *TROPOMI ATBD of the total and tropospheric NO₂ data products*; S5P-KNMI-L2-0005-RP; KNMI, De Bilt, The Netherlands, 2021. <http://www.tropomi.eu/data-products/nitrogen-dioxide/>.
- (187) Platt, U.; Stutz, J. *Differential Optical Absorption Spectroscopy, Physics of Earth and Space Environments*; Springer, 2008. DOI: <https://doi.org/10.1007/978-3-540-75776-4>.

- (188) Eskes, H. J.; Boersma, K. F. Averaging kernels for DOAS total-column satellite retrievals. *Atmos. Chem. Phys.* **2003**, *3* (5), 1285-1291. DOI: 10.5194/acp-3-1285-2003.
- (189) Bucsela, E. J.; Krotkov, N. A.; Celarier, E. A.; Lamsal, L. N.; Swartz, W. H.; Bhartia, P. K.; Boersma, K. F.; Veefkind, J. P.; Gleason, J. F.; Pickering, K. E. A new stratospheric and tropospheric NO₂ retrieval algorithm for nadir-viewing satellite instruments: applications to OMI. *Atmos. Meas. Tech.* **2013**, *6* (10), 2607-2626. DOI: 10.5194/amt-6-2607-2013.
- (190) Krotkov, N. A.; Lamsal, L. N.; Celarier, E. A.; Swartz, W. H.; Marchenko, S. V.; Bucsela, E. J.; Chan, K. L.; Wenig, M.; Zara, M. The version 3 OMI NO₂ standard product. *Atmos. Meas. Tech.* **2017**, *10* (9), 3133-3149. DOI: 10.5194/amt-10-3133-2017.
- (191) Griffin, D.; Zhao, X.; McLinden, C. A.; Boersma, F.; Bourassa, A.; Dammers, E.; Degenstein, D.; Eskes, H.; Fehr, L.; Fioletov, V.; et al. High-Resolution Mapping of Nitrogen Dioxide With TROPOMI: First Results and Validation Over the Canadian Oil Sands. *Geophysical Research Letters* **2019**, *46* (2), 1049-1060. DOI: <https://doi.org/10.1029/2018GL081095>.
- (192) Lamsal, L. N.; Krotkov, N. A.; Celarier, E. A.; Swartz, W. H.; Pickering, K. E.; Bucsela, E. J.; Gleason, J. F.; Martin, R. V.; Philip, S.; Irie, H.; et al. Evaluation of OMI operational standard NO₂ column retrievals using in situ and surface-based NO₂ observations. *Atmos. Chem. Phys.* **2014**, *14* (21), 11587-11609. DOI: 10.5194/acp-14-11587-2014.
- (193) Lorente, A.; Folkert Boersma, K.; Yu, H.; Dörner, S.; Hilboll, A.; Richter, A.; Liu, M.; Lamsal, L. N.; Barkley, M.; De Smedt, I.; et al. Structural uncertainty in air mass factor calculation for NO₂ and HCHO satellite retrievals. *Atmos. Meas. Tech.* **2017**, *10* (3), 759-782. DOI: 10.5194/amt-10-759-2017.
- (194) Li, J.; Wang, Y.; Zhang, R.; Smeltzer, C.; Weinheimer, A.; Herman, J.; Boersma, K. F.; Celarier, E. A.; Long, R. W.; Szykman, J. J.; et al. Comprehensive evaluations of diurnal NO₂ measurements during DISCOVER-AQ 2011: effects of resolution-dependent representation of NO_x emissions. *Atmos. Chem. Phys.* **2021**, *21* (14), 11133-11160. DOI: 10.5194/acp-21-11133-2021.
- (195) De Smedt, I.; Yu, H.; Richter, A.; Beirle, S.; Eskes, H.; Boersma, K. F.; Van Roozendaal, M.; Van Geffen, J.; Wagner, T.; Lorente, A.; et al. QA4ECV HCHO tropospheric column data from OMI. 1.1 ed.; Aeronomy, R. B. I. f. S., Ed.; Uccle, Belgium, 2017.
- (196) De Smedt, I.; Stavrou, T.; Hendrick, F.; Danckaert, T.; Vlemmix, T.; Pinardi, G.; Theys, N.; Lerot, C.; Gielen, C.; Vigouroux, C.; et al. Diurnal, seasonal and long-term variations of global formaldehyde columns inferred from combined OMI and GOME-2 observations. *Atmos. Chem. Phys.* **2015**, *15* (21), 12519-12545. DOI: 10.5194/acp-15-12519-2015.

- (197) Chance, K. OMI/Aura Formaldehyde (HCHO) Total Column 1-orbit L2 Swath 13x24 km. V003 ed.; DISC), G. E. S. D. a. I. S. C. G., Ed.; Greenbelt, MD, USA, 2007.
- (198) De Smedt, I.; Theys, N.; Yu, H.; Danckaert, T.; Lerot, C.; Compennolle, S.; Van Roozendael, M.; Richter, A.; Hilboll, A.; Peters, E.; et al. Algorithm theoretical baseline for formaldehyde retrievals from S5P TROPOMI and from the QA4ECV project. *Atmos. Meas. Tech.* **2018**, *11* (4), 2395-2426. DOI: 10.5194/amt-11-2395-2018.
- (199) Boersma, K. F.; Vinken, G. C. M.; Eskes, H. J. Representativeness errors in comparing chemistry transport and chemistry climate models with satellite UV-Vis tropospheric column retrievals. *Geosci. Model Dev.* **2016**, *9* (2), 875-898. DOI: 10.5194/gmd-9-875-2016.
- (200) Sekiya, T.; Miyazaki, K.; Eskes, H.; Sudo, K.; Takigawa, M.; Kanaya, Y. A comparison of the impact of TROPOMI and OMI tropospheric NO₂ on global chemical data assimilation. *Atmos. Meas. Tech.* **2022**, *15* (6), 1703-1728. DOI: 10.5194/amt-15-1703-2022.
- (201) Wang, Y.; Beirle, S.; Lampel, J.; Koukouli, M.; De Smedt, I.; Theys, N.; Li, A.; Wu, D.; Xie, P.; Liu, C.; et al. Validation of OMI, GOME-2A and GOME-2B tropospheric NO₂, SO₂ and HCHO products using MAX-DOAS observations from 2011 to 2014 in Wuxi, China: investigation of the effects of priori profiles and aerosols on the satellite products. *Atmos. Chem. Phys.* **2017**, *17* (8), 5007-5033. DOI: 10.5194/acp-17-5007-2017.
- (202) Zhang, R.; Wang, Y.; Smeltzer, C.; Qu, H.; Koshak, W.; Boersma, K. F. Comparing OMI-based and EPA AQS in situ NO₂ trends: towards understanding surface NO_x emission changes. *Atmos. Meas. Tech.* **2018**, *11* (7), 3955-3967. DOI: 10.5194/amt-11-3955-2018.
- (203) Zhao, C.; Wang, Y. Assimilated inversion of NO_x emissions over east Asia using OMI NO₂ column measurements. *Geophysical Research Letters* **2009**, *36* (6), <https://doi.org/10.1029/2008GL037123>. DOI: <https://doi.org/10.1029/2008GL037123> (accessed 2022/09/21).
- (204) Levelt, P. F.; Joiner, J.; Tamminen, J.; Veefkind, J. P.; Bhartia, P. K.; Stein Zweers, D. C.; Duncan, B. N.; Streets, D. G.; Eskes, H.; van der A, R.; et al. The Ozone Monitoring Instrument: overview of 14 years in space. *Atmos. Chem. Phys.* **2018**, *18* (8), 5699-5745. DOI: 10.5194/acp-18-5699-2018.
- (205) Boersma, K. F.; Geffen, J. v.; Eskes, H.; A, R. v. d.; Smedt, I. D.; Roozendael, M. V.; Yu, H.; Richter, A.; Peters, E.; Beirle, S.; et al. *Product Specification Document for the QA4ECV NO₂ ECV precursor product*; 1: KNMI, 2:BIRA-IASB, 3: IUP Bremen, 4: MPIC, 5: WUR, 6: NPL, 2017.
- (206) Compennolle, S.; Verhoelst, T.; Pinardi, G.; Granville, J.; Hubert, D.; Keppens, A.; Niemeijer, S.; Rino, B.; Bais, A.; Beirle, S.; et al. Validation of Aura-OMI QA4ECV NO₂

climate data records with ground-based DOAS networks: the role of measurement and comparison uncertainties. *Atmos. Chem. Phys.* **2020**, *20* (13), 8017-8045. DOI: 10.5194/acp-20-8017-2020.

(207) Gu, D.; Wang, Y.; Smeltzer, C.; Boersma, K. F. Anthropogenic emissions of NO_x over China: Reconciling the difference of inverse modeling results using GOME-2 and OMI measurements. *Journal of Geophysical Research: Atmospheres* **2014**, *119* (12), 7732-7740. DOI: <https://doi.org/10.1002/2014JD021644>.

(208) Su, W.; Liu, C.; Chan, K. L.; Hu, Q.; Liu, H.; Ji, X.; Zhu, Y.; Liu, T.; Zhang, C.; Chen, Y.; et al. An improved TROPOMI tropospheric HCHO retrieval over China. *Atmos. Meas. Tech.* **2020**, *13* (11), 6271-6292. DOI: 10.5194/amt-13-6271-2020.

(209) Douglass, A. R.; Stolarski, R. S.; Strahan, S. E.; Connell, P. S. Radicals and reservoirs in the GMI chemistry and transport model: Comparison to measurements. *Journal of Geophysical Research: Atmospheres* **2004**, *109* (D16). DOI: <https://doi.org/10.1029/2004JD004632>.

(210) Lamsal, L. N.; Krotkov, N. A.; Vasilkov, A.; Marchenko, S.; Qin, W.; Yang, E. S.; Fasnacht, Z.; Joiner, J.; Choi, S.; Haffner, D.; et al. Ozone Monitoring Instrument (OMI) Aura nitrogen dioxide standard product version 4.0 with improved surface and cloud treatments. *Atmos. Meas. Tech.* **2021**, *14* (1), 455-479. DOI: 10.5194/amt-14-455-2021.

(211) Williams, J. E.; Boersma, K. F.; Le Sager, P.; Verstraeten, W. W. The high-resolution version of TM5-MP for optimized satellite retrievals: description and validation. *Geosci. Model Dev.* **2017**, *10* (2), 721-750. DOI: 10.5194/gmd-10-721-2017.

(212) Guenther, A. B.; Jiang, X.; Heald, C. L.; Sakulyanontvittaya, T.; Duhl, T.; Emmons, L. K.; Wang, X. The Model of Emissions of Gases and Aerosols from Nature version 2.1 (MEGAN2.1): an extended and updated framework for modeling biogenic emissions. *Geosci. Model Dev.* **2012**, *5* (6), 1471-1492. DOI: 10.5194/gmd-5-1471-2012.

(213) Bucseles, E. J.; Perring, A. E.; Cohen, R. C.; Boersma, K. F.; Celarier, E. A.; Gleason, J. F.; Wenig, M. O.; Bertram, T. H.; Wooldridge, P. J.; Dirksen, R.; et al. Comparison of tropospheric NO₂ from in situ aircraft measurements with near-real-time and standard product data from OMI. *Journal of Geophysical Research: Atmospheres* **2008**, *113* (D16). DOI: <https://doi.org/10.1029/2007JD008838>.

(214) Riess, T. C. V. W.; Boersma, K. F.; van Vliet, J.; Peters, W.; Sneep, M.; Eskes, H.; van Geffen, J. Improved monitoring of shipping NO₂ with TROPOMI: decreasing NO_x emissions in European seas during the COVID-19 pandemic. *Atmos. Meas. Tech.* **2022**, *15* (5), 1415-1438. DOI: 10.5194/amt-15-1415-2022.

(215) Wang, P.; Stammes, P.; van der A, R.; Pinardi, G.; van Roozendaal, M. FRESCO+: an improved O₂ A-band cloud retrieval algorithm for tropospheric trace gas retrievals. *Atmos. Chem. Phys.* **2008**, *8* (21), 6565-6576. DOI: 10.5194/acp-8-6565-2008.

- (216) van Geffen, J.; Eskes, H.; Compernolle, S.; Pinardi, G.; Verhoelst, T.; Lambert, J. C.; Sneep, M.; ter Linden, M.; Ludewig, A.; Boersma, K. F.; et al. Sentinel-5P TROPOMI NO₂ retrieval: impact of version v2.2 improvements and comparisons with OMI and ground-based data. *Atmos. Meas. Tech.* **2022**, *15* (7), 2037-2060. DOI: 10.5194/amt-15-2037-2022.
- (217) Belmonte Rivas, M.; Veefkind, P.; Eskes, H.; Levelt, P. OMI tropospheric NO₂ profiles from cloud slicing: constraints on surface emissions, convective transport and lightning NO_x. *Atmos. Chem. Phys.* **2015**, *15* (23), 13519-13553. DOI: 10.5194/acp-15-13519-2015.
- (218) Davies, D. K.; Ilavajhala, S.; Wong, M. M.; Justice, C. O. Fire Information for Resource Management System: Archiving and Distributing MODIS Active Fire Data. *IEEE Transactions on Geoscience and Remote Sensing* **2009**, *47* (1), 72-79. DOI: 10.1109/TGRS.2008.2002076.
- (219) Hubert, D.; Heue, K. P.; Lambert, J. C.; Verhoelst, T.; Allaart, M.; Compernolle, S.; Cullis, P. D.; Dehn, A.; Félix, C.; Johnson, B. J.; et al. TROPOMI tropospheric ozone column data: geophysical assessment and comparison to ozonesondes, GOME-2B and OMI. *Atmos. Meas. Tech.* **2021**, *14* (12), 7405-7433. DOI: 10.5194/amt-14-7405-2021.
- (220) Stoffelen, A. Toward the true near-surface wind speed: Error modeling and calibration using triple collocation. *Journal of Geophysical Research: Oceans* **1998**, *103* (C4), 7755-7766. DOI: <https://doi.org/10.1029/97JC03180>.
- (221) Zwieback, S.; Scipal, K.; Dorigo, W.; Wagner, W. Structural and statistical properties of the collocation technique for error characterization. *Nonlin. Processes Geophys.* **2012**, *19* (1), 69-80. DOI: 10.5194/npg-19-69-2012.
- (222) McColl, K. A.; Vogelzang, J.; Konings, A. G.; Entekhabi, D.; Piles, M.; Stoffelen, A. Extended triple collocation: Estimating errors and correlation coefficients with respect to an unknown target. *Geophysical Research Letters* **2014**, *41* (17), 6229-6236. DOI: <https://doi.org/10.1002/2014GL061322>.
- (223) Dong, J.; Crow, W. T. An Improved Triple Collocation Analysis Algorithm for Decomposing Autocorrelated and White Soil Moisture Retrieval Errors. *Journal of Geophysical Research: Atmospheres* **2017**, *122* (24), 13,081-013,094. DOI: <https://doi.org/10.1002/2017JD027387>.
- (224) Beirle, S.; Platt, U.; Wenig, M.; Wagner, T. Weekly cycle of NO₂ by GOME measurements: a signature of anthropogenic sources. *Atmos. Chem. Phys.* **2003**, *3* (6), 2225-2232. DOI: 10.5194/acp-3-2225-2003.
- (225) Stavrakou, T.; Müller, J. F.; Bauwens, M.; Boersma, K. F.; van Geffen, J. Satellite evidence for changes in the NO₂ weekly cycle over large cities. *Scientific Reports* **2020**, *10* (1), 10066. DOI: 10.1038/s41598-020-66891-0.

(226) Shaiganfar, R.; Beirle, S.; Petetin, H.; Zhang, Q.; Beekmann, M.; Wagner, T. New concepts for the comparison of tropospheric NO₂ column densities derived from car-MAX-DOAS observations, OMI satellite observations and the regional model CHIMERE during two MEGAPOLI campaigns in Paris 2009/10. *Atmos. Meas. Tech.* **2015**, *8* (7), 2827-2852. DOI: 10.5194/amt-8-2827-2015.

(227) Choi, Y.; Kim, H.; Tong, D.; Lee, P. Summertime weekly cycles of observed and modeled NO_x and O₃ concentrations as a function of satellite-derived ozone production sensitivity and land use types over the Continental United States. *Atmos. Chem. Phys.* **2012**, *12* (14), 6291-6307. DOI: 10.5194/acp-12-6291-2012.

(228) Wang, Y.; Lampel, J.; Xie, P.; Beirle, S.; Li, A.; Wu, D.; Wagner, T. Ground-based MAX-DOAS observations of tropospheric aerosols, NO₂, SO₂ and HCHO in Wuxi, China, from 2011 to 2014. *Atmos. Chem. Phys.* **2017**, *17* (3), 2189-2215. DOI: 10.5194/acp-17-2189-2017.

(229) Wang, Y.; Dörner, S.; Donner, S.; Böhnke, S.; De Smedt, I.; Dickerson, R. R.; Dong, Z.; He, H.; Li, Z.; Li, Z.; et al. Vertical profiles of NO₂, SO₂, HONO, HCHO, CHOCHO and aerosols derived from MAX-DOAS measurements at a rural site in the central western North China Plain and their relation to emission sources and effects of regional transport. *Atmos. Chem. Phys.* **2019**, *19* (8), 5417-5449. DOI: 10.5194/acp-19-5417-2019.

(230) Zara, M.; Boersma, K. F.; De Smedt, I.; Richter, A.; Peters, E.; van Geffen, J. H. G. M.; Beirle, S.; Wagner, T.; Van Roozendaal, M.; Marchenko, S.; et al. Improved slant column density retrieval of nitrogen dioxide and formaldehyde for OMI and GOME-2A from QA4ECV: intercomparison, uncertainty characterisation, and trends. *Atmos. Meas. Tech.* **2018**, *11* (7), 4033-4058. DOI: 10.5194/amt-11-4033-2018.

(231) Laughner, J. L.; Zare, A.; Cohen, R. C. Effects of daily meteorology on the interpretation of space-based remote sensing of NO₂. *Atmos. Chem. Phys.* **2016**, *16* (23), 15247-15264. DOI: 10.5194/acp-16-15247-2016.

(232) Palmer, P. I.; Jacob, D. J.; Chance, K.; Martin, R. V.; Spurr, R. J. D.; Kurosu, T. P.; Bey, I.; Yantosca, R.; Fiore, A.; Li, Q. Air mass factor formulation for spectroscopic measurements from satellites: Application to formaldehyde retrievals from the Global Ozone Monitoring Experiment. *Journal of Geophysical Research: Atmospheres* **2001**, *106* (D13), 14539-14550. DOI: <https://doi.org/10.1029/2000JD900772>.

(233) Boersma, K. F.; Eskes, H. J.; Richter, A.; De Smedt, I.; Lorente, A.; Beirle, S.; van Geffen, J. H. G. M.; Zara, M.; Peters, E.; Van Roozendaal, M.; et al. Improving algorithms and uncertainty estimates for satellite NO₂ retrievals: results from the quality assurance for the essential climate variables (QA4ECV) project. *Atmos. Meas. Tech.* **2018**, *11* (12), 6651-6678. DOI: 10.5194/amt-11-6651-2018.

(234) Lorente, A.; Boersma, K. F.; Stammes, P.; Tilstra, L. G.; Richter, A.; Yu, H.; Kharbouche, S.; Muller, J. P. The importance of surface reflectance anisotropy for cloud

and NO₂ retrievals from GOME-2 and OMI. *Atmos. Meas. Tech.* **2018**, *11* (7), 4509-4529. DOI: 10.5194/amt-11-4509-2018.

(235) Fasnacht, Z.; Vasilkov, A.; Haffner, D.; Qin, W.; Joiner, J.; Krotkov, N.; Sayer, A. M.; Spurr, R. A geometry-dependent surface Lambertian-equivalent reflectivity product for UV–Vis retrievals – Part 2: Evaluation over open ocean. *Atmos. Meas. Tech.* **2019**, *12* (12), 6749-6769. DOI: 10.5194/amt-12-6749-2019.

(236) Qin, W.; Fasnacht, Z.; Haffner, D.; Vasilkov, A.; Joiner, J.; Krotkov, N.; Fisher, B.; Spurr, R. A geometry-dependent surface Lambertian-equivalent reflectivity product for UV–Vis retrievals – Part 1: Evaluation over land surfaces using measurements from OMI at 466 nm. *Atmos. Meas. Tech.* **2019**, *12* (7), 3997-4017. DOI: 10.5194/amt-12-3997-2019.

(237) Vasilkov, A.; Yang, E. S.; Marchenko, S.; Qin, W.; Lamsal, L.; Joiner, J.; Krotkov, N.; Haffner, D.; Bhartia, P. K.; Spurr, R. A cloud algorithm based on the O₂-O₂ 477 nm absorption band featuring an advanced spectral fitting method and the use of surface geometry-dependent Lambertian-equivalent reflectivity. *Atmos. Meas. Tech.* **2018**, *11* (7), 4093-4107. DOI: 10.5194/amt-11-4093-2018.

(238) Vasilkov, A.; Qin, W.; Krotkov, N.; Lamsal, L.; Spurr, R.; Haffner, D.; Joiner, J.; Yang, E. S.; Marchenko, S. Accounting for the effects of surface BRDF on satellite cloud and trace-gas retrievals: a new approach based on geometry-dependent Lambertian equivalent reflectivity applied to OMI algorithms. *Atmos. Meas. Tech.* **2017**, *10* (1), 333-349. DOI: 10.5194/amt-10-333-2017.

(239) Leitão, J.; Richter, A.; Vrekoussis, M.; Kokhanovsky, A.; Zhang, Q. J.; Beekmann, M.; Burrows, J. P. On the improvement of NO₂ satellite retrievals – aerosol impact on the airmass factors. *Atmos. Meas. Tech.* **2010**, *3* (2), 475-493. DOI: 10.5194/amt-3-475-2010.

(240) Alvarado, L. M. A.; Richter, A.; Vrekoussis, M.; Hilboll, A.; Kalisz Hedegaard, A. B.; Schneising, O.; Burrows, J. P. Unexpected long-range transport of glyoxal and formaldehyde observed from the Copernicus Sentinel-5 Precursor satellite during the 2018 Canadian wildfires. *Atmos. Chem. Phys.* **2020**, *20* (4), 2057-2072. DOI: 10.5194/acp-20-2057-2020.

(241) Xu, W. Y.; Zhao, C. S.; Ran, L.; Deng, Z. Z.; Liu, P. F.; Ma, N.; Lin, W. L.; Xu, X. B.; Yan, P.; He, X.; et al. Characteristics of pollutants and their correlation to meteorological conditions at a suburban site in the North China Plain. *Atmos. Chem. Phys.* **2011**, *11* (9), 4353-4369. DOI: 10.5194/acp-11-4353-2011.

(242) Fu, X.; Wang, S.; Chang, X.; Cai, S.; Xing, J.; Hao, J. Modeling analysis of secondary inorganic aerosols over China: pollution characteristics, and meteorological and dust impacts. *Scientific Reports* **2016**, *6* (1), 1-7.

- (243) Liu, X.; Zhang, Y.; Huey, L. G.; Yokelson, R. J.; Wang, Y.; Jimenez, J. L.; Campuzano-Jost, P.; Beyersdorf, A. J.; Blake, D. R.; Choi, Y.; et al. Agricultural fires in the southeastern U.S. during SEAC4RS: Emissions of trace gases and particles and evolution of ozone, reactive nitrogen, and organic aerosol. *Journal of Geophysical Research: Atmospheres* **2016**, *121* (12), 7383-7414. DOI: <https://doi.org/10.1002/2016JD025040>.
- (244) Chakrabarty, R. K.; Moosmüller, H.; Chen, L. W. A.; Lewis, K.; Arnott, W. P.; Mazzoleni, C.; Dubey, M. K.; Wold, C. E.; Hao, W. M.; Kreidenweis, S. M. Brown carbon in tar balls from smoldering biomass combustion. *Atmos. Chem. Phys.* **2010**, *10* (13), 6363-6370. DOI: 10.5194/acp-10-6363-2010.
- (245) Urbanski, S. P. Combustion efficiency and emission factors for wildfire-season fires in mixed conifer forests of the northern Rocky Mountains, US. *Atmos. Chem. Phys.* **2013**, *13* (14), 7241-7262. DOI: 10.5194/acp-13-7241-2013.
- (246) Zhang, A.; Wang, Y.; Zhang, Y.; Weber, R. J.; Song, Y.; Ke, Z.; Zou, Y. Modeling the global radiative effect of brown carbon: a potentially larger heating source in the tropical free troposphere than black carbon. *Atmos. Chem. Phys.* **2020**, *20* (4), 1901-1920. DOI: 10.5194/acp-20-1901-2020.
- (247) Zhang, Y.; Forrister, H.; Liu, J.; Dibb, J.; Anderson, B.; Schwarz, J. P.; Perring, A. E.; Jimenez, J. L.; Campuzano-Jost, P.; Wang, Y.; et al. Top-of-atmosphere radiative forcing affected by brown carbon in the upper troposphere. *Nature Geoscience* **2017**, *10* (7), 486-489. DOI: 10.1038/ngeo2960.
- (248) Bond, T. C.; Bergstrom, R. W. Light Absorption by Carbonaceous Particles: An Investigative Review. *Aerosol Science and Technology* **2006**, *40* (1), 27-67. DOI: 10.1080/02786820500421521.
- (249) Kanakidou, M.; Seinfeld, J. H.; Pandis, S. N.; Barnes, I.; Dentener, F. J.; Facchini, M. C.; Van Dingenen, R.; Ervens, B.; Nenes, A.; Nielsen, C. J.; et al. Organic aerosol and global climate modelling: a review. *Atmos. Chem. Phys.* **2005**, *5* (4), 1053-1123. DOI: 10.5194/acp-5-1053-2005.
- (250) Kroll, J. H.; Ng, N. L.; Murphy, S. M.; Flagan, R. C.; Seinfeld, J. H. Secondary Organic Aerosol Formation from Isoprene Photooxidation. *Environmental Science & Technology* **2006**, *40* (6), 1869-1877. DOI: 10.1021/es0524301.
- (251) Volkamer, R.; Jimenez, J. L.; San Martini, F.; Dzepina, K.; Zhang, Q.; Salcedo, D.; Molina, L. T.; Worsnop, D. R.; Molina, M. J. Secondary organic aerosol formation from anthropogenic air pollution: Rapid and higher than expected. *Geophysical Research Letters* **2006**, *33* (17). DOI: <https://doi.org/10.1029/2006GL026899>.
- (252) de Gouw, J. A.; Middlebrook, A. M.; Warneke, C.; Goldan, P. D.; Kuster, W. C.; Roberts, J. M.; Fehsenfeld, F. C.; Worsnop, D. R.; Canagaratna, M. R.; Pszenny, A. A. P.;

et al. Budget of organic carbon in a polluted atmosphere: Results from the New England Air Quality Study in 2002. *Journal of Geophysical Research: Atmospheres* **2005**, *110* (D16). DOI: <https://doi.org/10.1029/2004JD005623>.

(253) Stefenelli, G.; Jiang, J.; Bertrand, A.; Bruns, E. A.; Pieber, S. M.; Baltensperger, U.; Marchand, N.; Aksoyoglu, S.; Prévôt, A. S. H.; Slowik, J. G.; et al. Secondary organic aerosol formation from smoldering and flaming combustion of biomass: a box model parametrization based on volatility basis set. *Atmos. Chem. Phys.* **2019**, *19* (17), 11461-11484. DOI: 10.5194/acp-19-11461-2019.

(254) Kodros, J. K.; Papanastasiou, D. K.; Paglione, M.; Masiol, M.; Squizzato, S.; Florou, K.; Skyllakou, K.; Kaltsonoudis, C.; Nenes, A.; Pandis, S. N. Rapid dark aging of biomass burning as an overlooked source of oxidized organic aerosol. *Proceedings of the National Academy of Sciences* **2020**, *117* (52), 33028-33033. DOI: [doi:10.1073/pnas.2010365117](https://doi.org/10.1073/pnas.2010365117).

(255) Tohidi, R.; Altuwayjiri, A.; Pirhadi, M.; Sioutas, C. Quantifying ambient concentrations of primary and secondary organic aerosol in central Los Angeles using an integrated approach coupling source apportionment with regression analysis. *Atmospheric Environment* **2022**, *268*, 118807. DOI: <https://doi.org/10.1016/j.atmosenv.2021.118807>.

(256) Zheng, M.; Cass, G. R.; Schauer, J. J.; Edgerton, E. S. Source Apportionment of PM_{2.5} in the Southeastern United States Using Solvent-Extractable Organic Compounds as Tracers. *Environmental Science & Technology* **2002**, *36* (11), 2361-2371. DOI: 10.1021/es011275x.

(257) Ding, X.; Wang, X.-M.; Gao, B.; Fu, X.-X.; He, Q.-F.; Zhao, X.-Y.; Yu, J.-Z.; Zheng, M. Tracer-based estimation of secondary organic carbon in the Pearl River Delta, south China. *Journal of Geophysical Research: Atmospheres* **2012**, *117* (D5). DOI: <https://doi.org/10.1029/2011JD016596>.

(258) Lee, A.; Goldstein, A. H.; Kroll, J. H.; Ng, N. L.; Varutbangkul, V.; Flagan, R. C.; Seinfeld, J. H. Gas-phase products and secondary aerosol yields from the photooxidation of 16 different terpenes. *Journal of Geophysical Research: Atmospheres* **2006**, *111* (D17). DOI: <https://doi.org/10.1029/2006JD007050> (accessed 2023/10/30).

(259) Kleindienst, T. E.; Jaoui, M.; Lewandowski, M.; Offenberg, J. H.; Lewis, C. W.; Bhave, P. V.; Edney, E. O. Estimates of the contributions of biogenic and anthropogenic hydrocarbons to secondary organic aerosol at a southeastern US location. *Atmospheric Environment* **2007**, *41* (37), 8288-8300. DOI: <https://doi.org/10.1016/j.atmosenv.2007.06.045>.

(260) Turpin, B. J.; Huntzicker, J. J. Identification of secondary organic aerosol episodes and quantitation of primary and secondary organic aerosol concentrations during SCAQS. *Atmospheric Environment* **1995**, *29* (23), 3527-3544. DOI: [https://doi.org/10.1016/1352-2310\(94\)00276-Q](https://doi.org/10.1016/1352-2310(94)00276-Q).

- (261) Zhang, R.; Wang, G.; Guo, S.; Zamora, M. L.; Ying, Q.; Lin, Y.; Wang, W.; Hu, M.; Wang, Y. Formation of Urban Fine Particulate Matter. *Chemical Reviews* **2015**, *115* (10), 3803-3855. DOI: 10.1021/acs.chemrev.5b00067.
- (262) Schauer, J. J.; Rogge, W. F.; Hildemann, L. M.; Mazurek, M. A.; Cass, G. R.; Simoneit, B. R. T. Source apportionment of airborne particulate matter using organic compounds as tracers. *Atmospheric Environment* **1996**, *30* (22), 3837-3855. DOI: [https://doi.org/10.1016/1352-2310\(96\)00085-4](https://doi.org/10.1016/1352-2310(96)00085-4).
- (263) Shrivastava, M. K.; Subramanian, R.; Rogge, W. F.; Robinson, A. L. Sources of organic aerosol: Positive matrix factorization of molecular marker data and comparison of results from different source apportionment models. *Atmospheric Environment* **2007**, *41* (40), 9353-9369. DOI: 10.1016/j.atmosenv.2007.09.016.
- (264) Balachandran, S.; Chang, H. H.; Pachon, J. E.; Holmes, H. A.; Mulholland, J. A.; Russell, A. G. Bayesian-Based Ensemble Source Apportionment of PM_{2.5}. *Environmental Science & Technology* **2013**, *47* (23), 13511-13518. DOI: 10.1021/es4020647.
- (265) Kimmel, J. R.; Farmer, D. K.; Cubison, M. J.; Sueper, D.; Tanner, C.; Nemitz, E.; Worsnop, D. R.; Gonin, M.; Jimenez, J. L. Real-time aerosol mass spectrometry with millisecond resolution. *International Journal of Mass Spectrometry* **2011**, *303* (1), 15-26. DOI: <https://doi.org/10.1016/j.ijms.2010.12.004>.
- (266) Ng, N. L.; Herndon, S. C.; Trimborn, A.; Canagaratna, M. R.; Croteau, P. L.; Onasch, T. B.; Sueper, D.; Worsnop, D. R.; Zhang, Q.; Sun, Y. L.; et al. An Aerosol Chemical Speciation Monitor (ACSM) for Routine Monitoring of the Composition and Mass Concentrations of Ambient Aerosol. *Aerosol Science and Technology* **2011**, *45* (7), 780-794. DOI: 10.1080/02786826.2011.560211.
- (267) Canagaratna, M. R.; Jayne, J. T.; Jimenez, J. L.; Allan, J. D.; Alfarra, M. R.; Zhang, Q.; Onasch, T. B.; Drewnick, F.; Coe, H.; Middlebrook, A.; et al. Chemical and microphysical characterization of ambient aerosols with the aerodyne aerosol mass spectrometer. *Mass Spectrom Rev* **2007**, *26* (2), 185-222. DOI: 10.1002/mas.20115 From NLM.
- (268) Williams, L. R.; Gonzalez, L. A.; Peck, J.; Trimborn, D.; McInnis, J.; Farrar, M. R.; Moore, K. D.; Jayne, J. T.; Robinson, W. A.; Lewis, D. K.; et al. Characterization of an aerodynamic lens for transmitting particles greater than 1 micrometer in diameter into the Aerodyne aerosol mass spectrometer. *Atmos. Meas. Tech.* **2013**, *6* (11), 3271-3280. DOI: 10.5194/amt-6-3271-2013.
- (269) Peck, J.; Gonzalez, L. A.; Williams, L. R.; Xu, W.; Croteau, P. L.; Timko, M. T.; Jayne, J. T.; Worsnop, D. R.; Miake-Lye, R. C.; Smith, K. A. Development of an aerosol mass spectrometer lens system for PM_{2.5}. *Aerosol Science and Technology* **2016**, *50* (8), 781-789. DOI: 10.1080/02786826.2016.1190444.

(270) Xu, W.; Croteau, P.; Williams, L.; Canagaratna, M.; Onasch, T.; Cross, E.; Zhang, X.; Robinson, W.; Worsnop, D.; Jayne, J. Laboratory characterization of an aerosol chemical speciation monitor with PM_{2.5} measurement capability. *Aerosol Science and Technology* **2017**, *51* (1), 69-83. DOI: 10.1080/02786826.2016.1241859.

(271) Joo, T.; Chen, Y.; Xu, W.; Croteau, P.; Canagaratna, M. R.; Gao, D.; Guo, H.; Saavedra, G.; Kim, S. S.; Sun, Y.; et al. Evaluation of a New Aerosol Chemical Speciation Monitor (ACSM) System at an Urban Site in Atlanta, GA: The Use of Capture Vaporizer and PM_{2.5} Inlet. *ACS Earth and Space Chemistry* **2021**, *5* (10), 2565-2576. DOI: 10.1021/acsearthspacechem.1c00173.

(272) Elser, M.; Huang, R. J.; Wolf, R.; Slowik, J. G.; Wang, Q.; Canonaco, F.; Li, G.; Bozzetti, C.; Daellenbach, K. R.; Huang, Y.; et al. New insights into PM_{2.5} chemical composition and sources in two major cities in China during extreme haze events using aerosol mass spectrometry. *Atmos. Chem. Phys.* **2016**, *16* (5), 3207-3225. DOI: 10.5194/acp-16-3207-2016.

(273) Li, Z.; Xu, W.; Zhou, W.; Lei, L.; Sun, J.; You, B.; Wang, Z.; Sun, Y. Insights into the compositional differences of PM₁ and PM_{2.5} from aerosol mass spectrometer measurements in Beijing, China. *Atmospheric Environment* **2023**, *301*, 119709. DOI: <https://doi.org/10.1016/j.atmosenv.2023.119709>.

(274) Zheng, Y.; Cheng, X.; Liao, K.; Li, Y.; Li, Y. J.; Huang, R. J.; Hu, W.; Liu, Y.; Zhu, T.; Chen, S.; et al. Characterization of anthropogenic organic aerosols by TOF-ACSM with the new capture vaporizer. *Atmos. Meas. Tech.* **2020**, *13* (5), 2457-2472. DOI: 10.5194/amt-13-2457-2020.

(275) Zhang, Y.; Tang, L.; Croteau, P. L.; Favez, O.; Sun, Y.; Canagaratna, M. R.; Wang, Z.; Couvidat, F.; Albinet, A.; Zhang, H.; et al. Field characterization of the PM_{2.5} Aerosol Chemical Speciation Monitor: insights into the composition, sources, and processes of fine particles in eastern China. *Atmos. Chem. Phys.* **2017**, *17* (23), 14501-14517. DOI: 10.5194/acp-17-14501-2017.

(276) Hu, W.; Day, D. A.; Campuzano-Jost, P.; Nault, B. A.; Park, T.; Lee, T.; Croteau, P.; Canagaratna, M. R.; Jayne, J. T.; Worsnop, D. R.; et al. Evaluation of the New Capture Vaporizer for Aerosol Mass Spectrometers (AMS): Elemental Composition and Source Apportionment of Organic Aerosols (OA). *ACS Earth and Space Chemistry* **2018**, *2* (4), 410-421. DOI: 10.1021/acsearthspacechem.8b00002.

(277) Xu, W.; Chen, C.; Qiu, Y.; Xie, C.; Chen, Y.; Ma, N.; Xu, W.; Fu, P.; Wang, Z.; Pan, X.; et al. Size-resolved characterization of organic aerosol in the North China Plain: new insights from high resolution spectral analysis. *Environmental Science: Atmospheres* **2021**, *1* (6), 346-358, 10.1039/D1EA00025J. DOI: 10.1039/D1EA00025J.

(278) Katz, E. F.; Guo, H.; Campuzano-Jost, P.; Day, D. A.; Brown, W. L.; Boedicker, E.; Pothier, M.; Lunderberg, D. M.; Patel, S.; Patel, K.; et al. Quantification of cooking organic

aerosol in the indoor environment using aerodyne aerosol mass spectrometers. *Aerosol Science and Technology* **2021**, 55 (10), 1099-1114. DOI: 10.1080/02786826.2021.1931013.

(279) Xu, W.; Lambe, A.; Silva, P.; Hu, W.; Onasch, T.; Williams, L.; Croteau, P.; Zhang, X.; Renbaum-Wolff, L.; Fortner, E.; et al. Laboratory evaluation of species-dependent relative ionization efficiencies in the Aerodyne Aerosol Mass Spectrometer. *Aerosol Science and Technology* **2018**, 52 (6), 626-641. DOI: 10.1080/02786826.2018.1439570.

(280) Fröhlich, R.; Cubison, M. J.; Slowik, J. G.; Bukowiecki, N.; Canonaco, F.; Croteau, P. L.; Gysel, M.; Henne, S.; Herrmann, E.; Jayne, J. T.; et al. Fourteen months of on-line measurements of the non-refractory submicron aerosol at the Jungfraujoch (3580 m a.s.l.) – chemical composition, origins and organic aerosol sources. *Atmos. Chem. Phys.* **2015**, 15 (19), 11373-11398. DOI: 10.5194/acp-15-11373-2015.

(281) Meng, X.; Hand, J. L.; Schichtel, B. A.; Liu, Y. Space-time trends of PM_{2.5} constituents in the conterminous United States estimated by a machine learning approach, 2005–2015. *Environment International* **2018**, 121, 1137-1147. DOI: <https://doi.org/10.1016/j.envint.2018.10.029>.

(282) Lanzafame, G. M.; Srivastava, D.; Favez, O.; Bandowe, B. A. M.; Shahpoury, P.; Lammel, G.; Bonnaire, N.; Alleman, L. Y.; Couvidat, F.; Bessagnet, B.; et al. One-year measurements of secondary organic aerosol (SOA) markers in the Paris region (France): Concentrations, gas/particle partitioning and SOA source apportionment. *Sci Total Environ* **2021**, 757, 143921. DOI: 10.1016/j.scitotenv.2020.143921.

(283) Yu, S.; Dennis, R. L.; Bhave, P. V.; Eder, B. K. Primary and secondary organic aerosols over the United States: estimates on the basis of observed organic carbon (OC) and elemental carbon (EC), and air quality modeled primary OC/EC ratios. *Atmospheric Environment* **2004**, 38 (31), 5257-5268. DOI: <https://doi.org/10.1016/j.atmosenv.2004.02.064>.

(284) Schlag, P.; Kiendler-Scharr, A.; Blom, M. J.; Canonaco, F.; Henzing, J. S.; Moerman, M.; Prévôt, A. S. H.; Holzinger, R. Aerosol source apportionment from 1-year measurements at the CESAR tower in Cabauw, the Netherlands. *Atmos. Chem. Phys.* **2016**, 16 (14), 8831-8847. DOI: 10.5194/acp-16-8831-2016.

(285) Chow, J. C.; Watson, J. G.; Chen, L. W.; Chang, M. C.; Robinson, N. F.; Trimble, D.; Kohl, S. The IMPROVE_A temperature protocol for thermal/optical carbon analysis: maintaining consistency with a long-term database. *J Air Waste Manag Assoc* **2007**, 57 (9), 1014-1023. DOI: 10.3155/1047-3289.57.9.1014.

(286) van der Werf, G. R.; Randerson, J. T.; Giglio, L.; van Leeuwen, T. T.; Chen, Y.; Rogers, B. M.; Mu, M.; van Marle, M. J. E.; Morton, D. C.; Collatz, G. J.; et al. Global fire emissions estimates during 1997–2016. *Earth Syst. Sci. Data* **2017**, 9 (2), 697-720. DOI: 10.5194/essd-9-697-2017.

- (287) Hersbach, H.; Bell, B.; Berrisford, P.; Biavati, G.; Horányi, A.; Muñoz Sabater, J.; Nicolas, J.; Peubey, C.; Radu, R.; Rozum, I.; et al. ERA5 monthly averaged data on single levels from 1959 to present. (CDS), C. C. C. S. C. S. C. D. S., Ed.; 2019.
- (288) Tukey, J. W. *Exploratory data analysis*; Reading, MA, 1977.
- (289) Bansal, N.; Blum, A.; Chawla, S. Correlation Clustering. *Machine Learning* **2004**, *56* (1), 89-113. DOI: 10.1023/B:MACH.0000033116.57574.95.
- (290) Bhattacharya, A.; De, R. K. Average correlation clustering algorithm (ACCA) for grouping of co-regulated genes with similar pattern of variation in their expression values. *J Biomed Inform* **2010**, *43* (4), 560-568. DOI: 10.1016/j.jbi.2010.02.001.
- (291) Lee, S.; Wang, Y.; Russell, A. G. Assessment of Secondary Organic Carbon in the Southeastern United States: A Review. *Journal of the Air & Waste Management Association* **2010**, *60* (11), 1282-1292. DOI: 10.3155/1047-3289.60.11.1282.
- (292) Ding, X.; Zheng, M.; Edgerton, E. S.; Jansen, J. J.; Wang, X. Contemporary or Fossil Origin: Split of Estimated Secondary Organic Carbon in the Southeastern United States. *Environmental Science & Technology* **2008**, *42* (24), 9122-9128. DOI: 10.1021/es802115t.
- (293) Tanner, R. L.; Parkhurst, W. J.; Valente, M. L.; David Phillips, W. Regional composition of PM_{2.5} aerosols measured at urban, rural and “background” sites in the Tennessee valley. *Atmospheric Environment* **2004**, *38* (20), 3143-3153. DOI: <https://doi.org/10.1016/j.atmosenv.2004.03.023>.
- (294) Day, M. C.; Zhang, M.; Pandis, S. N. Evaluation of the ability of the EC tracer method to estimate secondary organic carbon. *Atmospheric Environment* **2015**, *112*, 317-325. DOI: <https://doi.org/10.1016/j.atmosenv.2015.04.044>.
- (295) Zhang, Q.; Wang, Y.; Liu, M.; Zheng, M.; Yuan, L.; Liu, J.; Tao, S.; Wang, X. Wintertime Formation of Large Sulfate Particles in China and Implications for Human Health. *Environmental Science & Technology* **2023**. DOI: 10.1021/acs.est.3c05645.
- (296) Lee, S.; Liu, W.; Wang, Y.; Russell, A. G.; Edgerton, E. S. Source apportionment of PM_{2.5}: Comparing PMF and CMB results for four ambient monitoring sites in the southeastern United States. *Atmospheric Environment* **2008**, *42* (18), 4126-4137. DOI: <https://doi.org/10.1016/j.atmosenv.2008.01.025>.
- (297) Bae, M.-S.; Skiles, M. J.; Lai, A. M.; Olson, M. R.; de Foy, B.; Schauer, J. J. Assessment of forest fire impacts on carbonaceous aerosols using complementary molecular marker receptor models at two urban locations in California's San Joaquin Valley. *Environmental Pollution* **2019**, *246*, 274-283. DOI: <https://doi.org/10.1016/j.envpol.2018.12.013>.

- (298) Rogge, W. F.; Mazurek, M. A.; Hildemann, L. M.; Cass, G. R.; Simoneit, B. R. T. Quantification of urban organic aerosols at a molecular level: Identification, abundance and seasonal variation. *Atmospheric Environment. Part A. General Topics* **1993**, *27* (8), 1309-1330. DOI: [https://doi.org/10.1016/0960-1686\(93\)90257-Y](https://doi.org/10.1016/0960-1686(93)90257-Y).
- (299) Zhang, Y.; Favez, O.; Petit, J. E.; Canonaco, F.; Truong, F.; Bonnaire, N.; Crenn, V.; Amodeo, T.; Prévôt, A. S. H.; Sciare, J.; et al. Six-year source apportionment of submicron organic aerosols from near-continuous highly time-resolved measurements at SIRTÀ (Paris area, France). *Atmos. Chem. Phys.* **2019**, *19* (23), 14755-14776. DOI: 10.5194/acp-19-14755-2019.
- (300) Yu, S.; Bhave, P. V.; Dennis, R. L.; Mathur, R. Seasonal and regional variations of primary and secondary organic aerosols over the continental United States: semi-empirical estimates and model evaluation. *Environ Sci Technol* **2007**, *41* (13), 4690-4697. DOI: 10.1021/es061535g From NLM.
- (301) Verma, V.; Fang, T.; Guo, H.; King, L.; Bates, J. T.; Peltier, R. E.; Edgerton, E.; Russell, A. G.; Weber, R. J. Reactive oxygen species associated with water-soluble PM_{2.5} in the southeastern United States: spatiotemporal trends and source apportionment. *Atmos. Chem. Phys.* **2014**, *14* (23), 12915-12930. DOI: 10.5194/acp-14-12915-2014.
- (302) Kim, P. S.; Jacob, D. J.; Fisher, J. A.; Travis, K.; Yu, K.; Zhu, L.; Yantosca, R. M.; Sulprizio, M. P.; Jimenez, J. L.; Campuzano-Jost, P.; et al. Sources, seasonality, and trends of southeast US aerosol: an integrated analysis of surface, aircraft, and satellite observations with the GEOS-Chem chemical transport model. *Atmos. Chem. Phys.* **2015**, *15* (18), 10411-10433. DOI: 10.5194/acp-15-10411-2015.
- (303) Canonaco, F.; Slowik, J. G.; Baltensperger, U.; Prévôt, A. S. H. Seasonal differences in oxygenated organic aerosol composition: implications for emissions sources and factor analysis. *Atmos. Chem. Phys.* **2015**, *15* (12), 6993-7002. DOI: 10.5194/acp-15-6993-2015.
- (304) Xu, L.; Guo, H.; Boyd, C. M.; Klein, M.; Bougiatioti, A.; Cerully, K. M.; Hite, J. R.; Isaacman-VanWertz, G.; Kreisberg, N. M.; Knote, C.; et al. Effects of anthropogenic emissions on aerosol formation from isoprene and monoterpenes in the southeastern United States. *Proceedings of the National Academy of Sciences* **2015**, *112* (1), 37-42. DOI: doi:10.1073/pnas.1417609112.
- (305) Zeng, T.; Wang, Y. Nationwide summer peaks of OC/EC ratios in the contiguous United States. *Atmospheric Environment* **2011**, *45* (3), 578-586. DOI: <https://doi.org/10.1016/j.atmosenv.2010.10.038>.
- (306) Gunsch, M. J.; May, N. W.; Wen, M.; Bottenus, C. L. H.; Gardner, D. J.; VanReken, T. M.; Bertman, S. B.; Hopke, P. K.; Ault, A. P.; Pratt, K. A. Ubiquitous influence of wildfire emissions and secondary organic aerosol on summertime atmospheric aerosol in the forested Great Lakes region. *Atmos. Chem. Phys.* **2018**, *18* (5), 3701-3715. DOI: 10.5194/acp-18-3701-2018.

- (307) Hand, J. L.; Copeland, S. A.; Day, D.; Dilner, A. M.; Indresand, H.; Malm, W. C.; McDade, C. E.; Moore, C. T.; Pitchford, M.; Schichtel, B. A.; et al. *Spatial and Seasonal Patterns and Temporal Variability of Haze and its Constituents in the United States: Report V*; 2011.
- (308) Zhou, S.; Collier, S.; Xu, J.; Mei, F.; Wang, J.; Lee, Y.-N.; Sedlacek III, A. J.; Springston, S. R.; Sun, Y.; Zhang, Q. Influences of upwind emission sources and atmospheric processing on aerosol chemistry and properties at a rural location in the Northeastern U.S. *Journal of Geophysical Research: Atmospheres* **2016**, *121* (10), 6049-6065. DOI: <https://doi.org/10.1002/2015JD024568>.
- (309) Hallquist, M.; Wenger, J. C.; Baltensperger, U.; Rudich, Y.; Simpson, D.; Claeys, M.; Dommen, J.; Donahue, N. M.; George, C.; Goldstein, A. H.; et al. The formation, properties and impact of secondary organic aerosol: current and emerging issues. *Atmos. Chem. Phys.* **2009**, *9* (14), 5155-5236. DOI: 10.5194/acp-9-5155-2009.
- (310) Surratt, J. D.; Chan, A. W. H.; Eddingsaas, N. C.; Chan, M.; Loza, C. L.; Kwan, A. J.; Hersey, S. P.; Flagan, R. C.; Wennberg, P. O.; Seinfeld, J. H. Reactive intermediates revealed in secondary organic aerosol formation from isoprene. *Proceedings of the National Academy of Sciences* **2010**, *107* (15), 6640-6645. DOI: [doi:10.1073/pnas.0911114107](https://doi.org/10.1073/pnas.0911114107).
- (311) Zhang, J.; Wang, J.; Sun, Y.; Zhou, S.; Shrivastava, M.; Catena, A.; Ng, N. L.; Zhang, Q.; Schwab, J. The Response of Summertime Organic Aerosol Composition to Emission Controls in the Northeastern United States. *Journal of Geophysical Research: Atmospheres* **2022**, *127* (20), e2022JD037056. DOI: <https://doi.org/10.1029/2022JD037056>.
- (312) Liang, Y.; Weber, R. J.; Misztal, P. K.; Jen, C. N.; Goldstein, A. H. Aging of Volatile Organic Compounds in October 2017 Northern California Wildfire Plumes. *Environmental Science & Technology* **2022**. DOI: 10.1021/acs.est.1c05684.
- (313) Farley, R.; Bernays, N.; Jaffe, D. A.; Ketcherside, D.; Hu, L.; Zhou, S.; Collier, S.; Zhang, Q. Persistent Influence of Wildfire Emissions in the Western United States and Characteristics of Aged Biomass Burning Organic Aerosols under Clean Air Conditions. *Environmental Science & Technology* **2022**. DOI: 10.1021/acs.est.1c07301.
- (314) Sarangi, C.; Qian, Y.; Leung, L. R.; Zhang, Y.; Zou, Y.; Wang, Y. Projected increases in wildfires may challenge regulatory curtailment of PM_{2.5} over the eastern US by 2050. *Atmos. Chem. Phys.* **2023**, *23* (2), 1769-1783. DOI: 10.5194/acp-23-1769-2023.
- (315) Xie, Y.; Lin, M.; Decharme, B.; Delire, C.; Horowitz, L. W.; Lawrence, D. M.; Li, F.; Séférian, R. Tripling of western US particulate pollution from wildfires in a warming climate. *Proceedings of the National Academy of Sciences* **2022**, *119* (14), e2111372119. DOI: [doi:10.1073/pnas.2111372119](https://doi.org/10.1073/pnas.2111372119).

(316) Zou, Y.; Rasch, P. J.; Wang, H.; Xie, Z.; Zhang, R. Increasing large wildfires over the western United States linked to diminishing sea ice in the Arctic. *Nature Communications* **2021**, *12* (1), 6048. DOI: 10.1038/s41467-021-26232-9.

(317) National Ambient Air Quality Standards for Particulate Matter. Office of the Federal Register, U.S. Government Publishing Office: Washington, DC, 2013; Vol. 78, pp 3086-3287.

(318) Enders, J. J.; Rhead, T. W.; Phan, J. A.; Zoerb, M. C. Impacts of 2018 California Wildfires on Organic Aerosol Composition and Air Quality under Low Smoke Conditions. *ACS Earth and Space Chemistry* **2021**, *5* (2), 163-169. DOI: 10.1021/acsearthspacechem.0c00202.

(319) Laing, R. J.; Jaffe, D. A. Wildfires are causing extreme PM concentrations in the western United

States. In *The Magazine for Environmental Managers*, 2019.

(320) Mardi, A. H.; Dadashazar, H.; Painemal, D.; Shingler, T.; Seaman, S. T.; Fenn, M. A.; Hostetler, C. A.; Sorooshian, A. Biomass Burning Over the United States East Coast and Western North Atlantic Ocean: Implications for Clouds and Air Quality. *Journal of Geophysical Research: Atmospheres* **2021**, *126* (20), e2021JD034916. DOI: <https://doi.org/10.1029/2021JD034916>.

(321) Zhang, B.; Owen, R. C.; Perlinger, J. A.; Helmig, D.; Val Martín, M.; Kramer, L.; Mazzoleni, L. R.; Mazzoleni, C. Ten-year chemical signatures associated with long-range transport observed in the free troposphere over the central North Atlantic. *Elementa: Science of the Anthropocene* **2017**, *5*, 8. DOI: 10.1525/elementa.194 (accessed 10/19/2023).

(322) Russell, A. R.; Valin, L. C.; Cohen, R. C. Trends in OMI NO₂ observations over the United States: effects of emission control technology and the economic recession. *Atmos. Chem. Phys.* **2012**, *12* (24), 12197-12209. DOI: 10.5194/acp-12-12197-2012.

(323) Sullivan, A. P.; Guo, H.; Schroder, J. C.; Campuzano-Jost, P.; Jimenez, J. L.; Campos, T.; Shah, V.; Jaeglé, L.; Lee, B. H.; Lopez-Hilfiker, F. D.; et al. Biomass Burning Markers and Residential Burning in the WINTER Aircraft Campaign. *Journal of Geophysical Research: Atmospheres* **2019**, *124* (3), 1846-1861. DOI: <https://doi.org/10.1029/2017JD028153>.

(324) Schroder, J. C.; Campuzano-Jost, P.; Day, D. A.; Shah, V.; Larson, K.; Sommers, J. M.; Sullivan, A. P.; Campos, T.; Reeves, J. M.; Hills, A.; et al. Sources and Secondary Production of Organic Aerosols in the Northeastern United States during WINTER. *Journal of Geophysical Research: Atmospheres* **2018**, *123* (14), 7771-7796. DOI: <https://doi.org/10.1029/2018JD028475>.

- (325) Kaulfus, A. S.; Nair, U.; Jaffe, D.; Christopher, S. A.; Goodrick, S. Biomass Burning Smoke Climatology of the United States: Implications for Particulate Matter Air Quality. *Environmental Science & Technology* **2017**, *51* (20), 11731-11741. DOI: 10.1021/acs.est.7b03292.
- (326) Nault, B. A.; Jo, D. S.; McDonald, B. C.; Campuzano-Jost, P.; Day, D. A.; Hu, W.; Schroder, J. C.; Allan, J.; Blake, D. R.; Canagaratna, M. R.; et al. Secondary organic aerosols from anthropogenic volatile organic compounds contribute substantially to air pollution mortality. *Atmos. Chem. Phys.* **2021**, *21* (14), 11201-11224. DOI: 10.5194/acp-21-11201-2021.
- (327) Pye, H. O. T.; Ward-Caviness, C. K.; Murphy, B. N.; Appel, K. W.; Seltzer, K. M. Secondary organic aerosol association with cardiorespiratory disease mortality in the United States. *Nature Communications* **2021**, *12* (1), 7215. DOI: 10.1038/s41467-021-27484-1.
- (328) Moon, A.; Jongebloed, U.; Dingilian, K. K.; Schauer, A. J.; Chan, Y.-C.; Cesler-Maloney, M.; Simpson, W. R.; Weber, R. J.; Tsiang, L.; Yazbeck, F.; et al. Primary Sulfate Is the Dominant Source of Particulate Sulfate during Winter in Fairbanks, Alaska. *ACS ES&T Air* **2023**. DOI: 10.1021/acsestair.3c00023.